EVALUATION OF ACID JETTING IN MATRIX ACIDIZING TREATMENTS

IN CARBONATE RESERVOIRS

A Thesis

by

TAYLOR ROSS FRICK

Submitted to the Office of Graduate and Professional Studies of
Texas A&M University
in partial fulfillment of the requirements for the degree of

MASTER OF SCIENCE

Chair of Committee,	Ding Zhu
Committee Members,	A. Daniel Hill
	Michael Pope
Head of Department,	Jeff Spath

December 2018

Major Subject: Petroleum Engineering

ABSTRACT

Various open-hole completion and stimulation designs used in horizontal wells in carbonate reservoirs cause hydrochloric acid (HCl) to be jetted onto the wellbore surface at high velocity. To properly design a limited entry liner completion and acid stimulation job, wormhole growth due to the acid jet at an orifice and skin reduction due to jetting wormhole growth must be modeled. The literature supplies adequate models of matrix acidizing wormhole growth but not wormhole growth due to an acid jet.

To assist the modeling effort, previous experimental studies were conducted where HCl was jetted through limestone cores using a novel apparatus and procedure. These studies have shown that bulb-shaped cavities form at the base of cores and that dominant wormholes propagate from the base of the cavity structures. One limitation of the previous experimental studies was that interstitial velocity was allowed to increase throughout experiments and not maintained constant.

For this study, the apparatus and procedure used in the previous studies were modified to conduct approximately constant interstitial velocity experiments. 15% HCl was jetted 80 ft/s with constant interstitial velocity through 4-inch diameter by 8-inch length Indiana limestone cores at room temperature. Additionally, a fitting was designed to disperse acid evenly across the core's face in an effort to simulate a matrix acidizing with the jetting apparatus. These "non-jetting" experiments were conducted using the same conditions as the jetting experiments in an effort to have a calibrated comparison between acid jetting and matrix acidizing.

These two sets of experiments were fit to a semi-empirical matrix acidizing wormhole model to gain insights into the wormhole growth behavior of the acid jetting process and its comparison to matrix acidizing. CT images of dissolution structures within cores are shown with reference to interstitial velocity to demonstrate the apparent dissolution regimes of acid jetting at various interstitial velocities and compared to matrix acidizing. Based on the laboratory, core-scale experimental acid jetting result, a theoretical, wellbore-scale wormhole/dissolution geometry is proposed and the geometry's overall impact on apparent well skin and productivity is postulated.

DEDICATION

This thesis is dedicated to those who sacrifice time away from family and friends to get the job done in the oilfield providing for themselves, their families, and the energy the world needs to create and sustain a high quality of life for all people. More emphatically, this thesis is dedicated to those who have lost their lives on the job in this honorable mission.

ACKNOWLEDGEMENTS

CONTRIBUTORS AND FUNDING SOURCES

NOMENCLATURE

μ	Fluid Viscosity
A	Cross-Sectional Area
D_{core}	Core Diameter
DICOM	Digital Imaging and Communications in Medicine
k	Permeability
L	Length
L_{core}	Core Length
MD	Measured Depth
m_{dry}	Dry (Unsaturated) Mass
m_i	Current Mass Value
m_{i-10}	Mass Value 10 Samples Previously
m_{wet}	Water-saturated Mass
PV_{bt}	Pore Volumes to Break Through
Q	Volumetric Flowrate
Q_{flux}	Volumetric Flowrate of Fluid Flux through Core
t_s	Time Between Samples (inverse of sampling frequency)
TVD	Total Vertical Depth
V_{bulk}	Bulk Volume
v_i	Interstitial Velocity
v_{wh}	Wormhole Velocity (or Growth Rate)

V_{pore}	Pore Volume
ΔP	Differential Pressure
ρ_{water}	Liquid Water Density
Φ	Porosity
HCl	Hydrochloric Acid

TABLE OF CONTENTS

LIST OF FIGURES

LIST OF TABLES

1. INTRODUCTION AND LITERATURE REVIEW

1.1 Background on Matrix Acidizing in Carbonate Reservoirs

Oil and gas wells drilled in carbonate reservoirs are often stimulated with hydrochloric acid (HCl). Due to high reaction rates between carbonate rock and HCl, non-uniform, tunnel-like dissolution patterns, called wormholes (Figure 1), can form when HCl is pumped into a carbonate reservoir (Economides et al. 2013). Fluid flow through wormholes displays negligible pressure drop compared to that of Darcy flow, therefore, when wormholes propagate from a well into the formation they reduce the well's skin effect, essentially "enlarging" the wellbore (Economides et al. 2013).
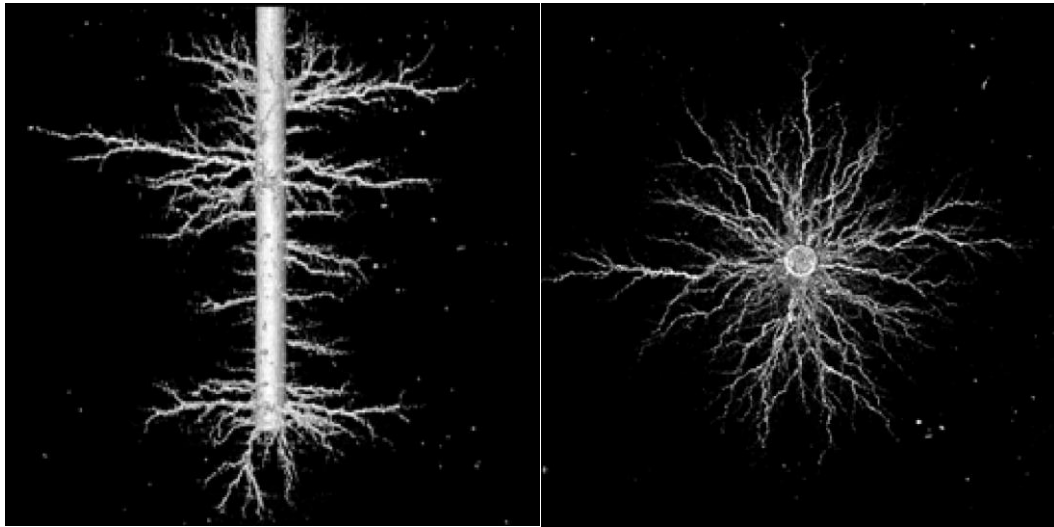
Figure 1 - Wormhole Dissolution Structure from Large Carbonate Block Acidizing Experiment (Reprinted from McDuff et al. (2010))

As acid fluxes into carbonate rock, the largest, most conductive pores accept the most acid, get larger due to dissolution, and ultimately become wormholes. Once a wormhole forms, some acid will reach the wormhole tip via convective transport

extending the wormhole, and some acid will be consumed by molecular diffusion and convective transport, or fluid loss, through the walls of the wormhole. As a wormhole grows in length, the portion of acid lost through molecular diffusion and convective fluid loss increases and ultimately becomes a limiting factor of wormhole growth (Economides et al. 2013).

Based on the information above, one can deduce that the structure of wormholes, or formation of wormholes at all, depends on several independent parameters. For constant governing parameters such as rock type, acid system, and temperature, a progression of wormhole regimes occur at what can be termed low, optimum, and high convection rates, or fluxes. Interstitial velocity is a term which several global matrix acidizing models utilize to characterize flux rates (Buijse and Glasenbergen 2005, Furui et al. 2010). Interstitial velocity can be defined as:

$$v_i = \frac{Q}{A\varphi} \tag{1}$$

where v_i is interstitial velocity, Q is volumetric flowrate, A is cross-sectional flow area, and φ is porosity (Buijse and Glasenbergen 2005).

Many laboratory experiments have proven the concept of low, optimum, and high interstitial velocity wormhole regimes (Fredd and Fogler 1999, Buijse and Glasenbergen 2005, Jin 2013). In matrix acidizing core flood experiments, the wormhole behavior progression is as follows: at extremely low interstitial velocities, compact dissolution occurs on the face of cores; increasing interstitial velocities result in thick wormholes termed "conical"; increasing interstitial velocity farther results in narrower wormhole

termed "dominant"; and increasing interstitial velocity more results in more branched wormholes that consume more acid (Fredd and Fogler 1999, Economides et al. 2013, Buijse and Glasenbergen 2005). Compact dissolution and conical wormholes represent the low interstitial velocity regime, dominant wormholes represent the optimum regime, and the highly branched wormholes represent the high interstitial velocity regime (Figure 2).
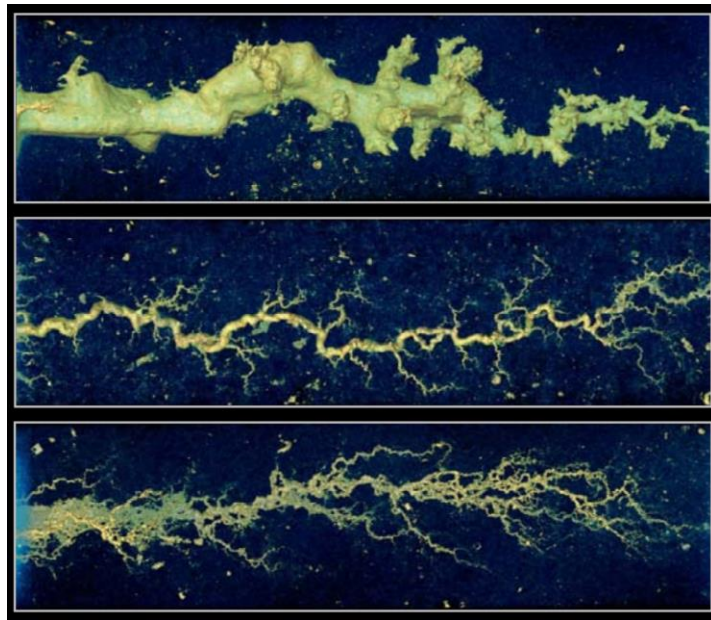
Figure 2 – CT Scan Visualizations of Conical (top), Dominant (middle), and Highly Branched (bottom) Wormhole Regimes (Reprinted from McDuff et al. (2010))

When a set of matrix acidizing core flood experiments with constant parameters (rock type, acid system, and temperature) are performed at varying flux rates, similar to Figure 2, a plot can be generated with the experimental data that proves useful in matrix acidizing wormhole growth modeling. In each matrix acidizing core flood, there is a volume of acid which is required for the acid to break through the core. When this volume

is divided by the core pore volume, a normalized volume is created, termed the pore volume to breakthrough, or PV_{bt}. By plotting the pore volume to breakthrough of experiments versus the interstitial velocity on a log-log plot, an optimal interstitial velocity becomes apparent (Figure 3). This plot helped establish an industry practice of pumping above the optimal rate, due to the minimal loss of efficiency above the optimal point versus the severe loss of efficiency below the optimal point. An example of PV_{bt} vs. v_i plots, or wormhole efficiency curves, is shown in Figure 3.
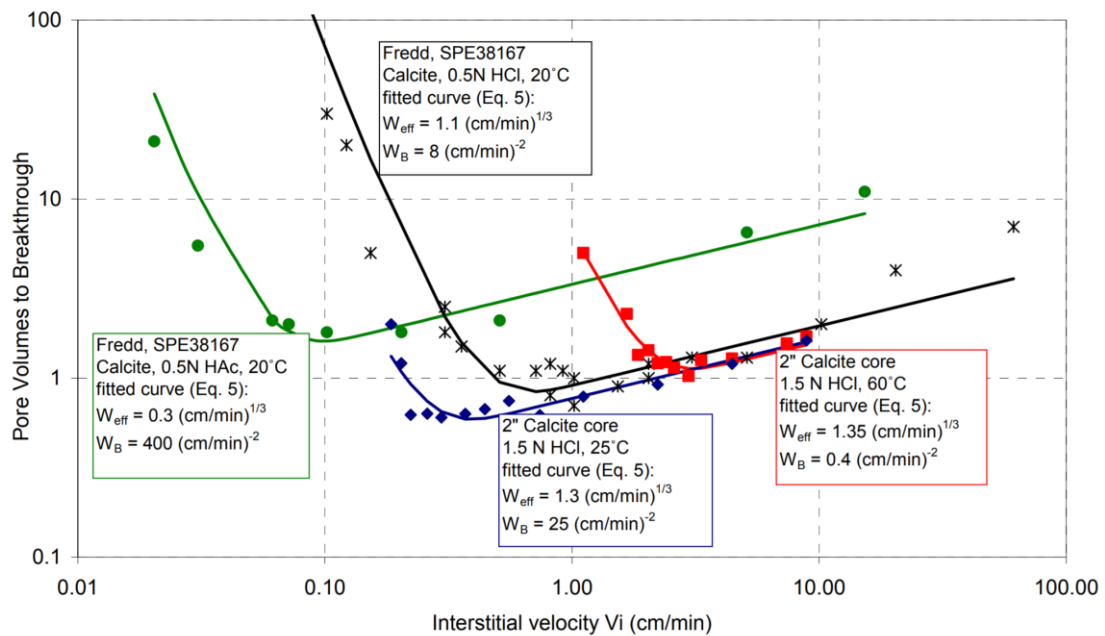
Figure 3 - Wormhole Efficiency Curves for Matrix Acidizing Experiments of Calcite Cores at Various Experimental Conditions (Reprinted from Buijse and Glasenbergen (2005))

1.2 Completion of Extended Reach Wells in Carbonate Reservoirs

In order to decrease costs, improve recovery, and minimize environmental impact, some oil and gas reservoirs are developed using extended reach wells with measured depth

(MD) to total vertical depth (TVD) ratios greater than 2 and lateral lengths greater than 10,000 ft (Issa, Abbott, and Akbari 2014). Due to the complexity and risks associated with running casing, cementing, and perforating in extended reach wells, an open-hole completion may be preferable (Mason, Hey, and Kramer 1997). To enhance productivity, wells completed in carbonate reservoirs will typically require acid stimulation (Economides et al. 2013). A conventional matrix acidizing treatment in a cemented and perforated liner may typically only cover a 750 ft interval, furthering the cause for an open-hole completion in a long lateral more than 10,000 ft (Hansen and Nederveen 2002).

An extended reach well in a carbonate reservoir requires a completion design framework which places high priority on the ability to successfully perform an initial acid stimulation as well as subsequent interventions. Barefoot completions are the simplest and lowest-cost open-hole completion; however, in a long lateral, a bullhead acid stimulation in a barefoot completion is unrealistic as only the heel region would be stimulated. With this in mind, coiled tubing may be employed for stimulation in a barefoot completion, but field experience has demonstrated that getting to TD with coiled tubing in a barefoot completion in a long lateral is highly unlikely. A high-density pre-perforated liner can increase reach capabilities of coiled tubing by reducing friction, but due to rate limitations of coiled tubing, stimulations using this technique are more focused on removing mud and filter cake damage as opposed to aggressive stimulation (Jackson et al. 2012).

Various open-hole completion designs allow more efficient bullhead acid stimulation in long laterals, including limited entry liners, ball drop fracture liners, and combination limited entry-ball drop liners. Both of the ball drop completions are multi-

stage techniques that allow for aggressive stimulation but are more expensive and require more logistical planning. The limited entry liner completion allows for a less expensive but less aggressive single-stage bullhead acid treatment (Jackson et al. 2012). When a matrix acidizing stimulation is desired, the limited entry liner (single-stage) or limited entry-ball drop liner (multi-stage) completion may be implemented.

1.3 Background on Limited Entry Liner Completions

A limited entry liner completion, shown in Figure 4, features pre-drilled holes that can be engineered (diameter, location, and density) and packers that can be engineered (location and density) to evenly distribute acid along the lateral at certain flow rates (Sau et al. 2014). The pre-drilled holes, or orifices, in open-hole limited entry completions create significant pressure drops between the inside of the liner and outside of the liner in the annulus region. This phenomenon pushes acid to the toe of the well via a choke effect. In addition to the pressure drop, the orifices create high-velocity jets of acid which strike the borehole wall (Mayer, Sau, and Shuchart 2014).
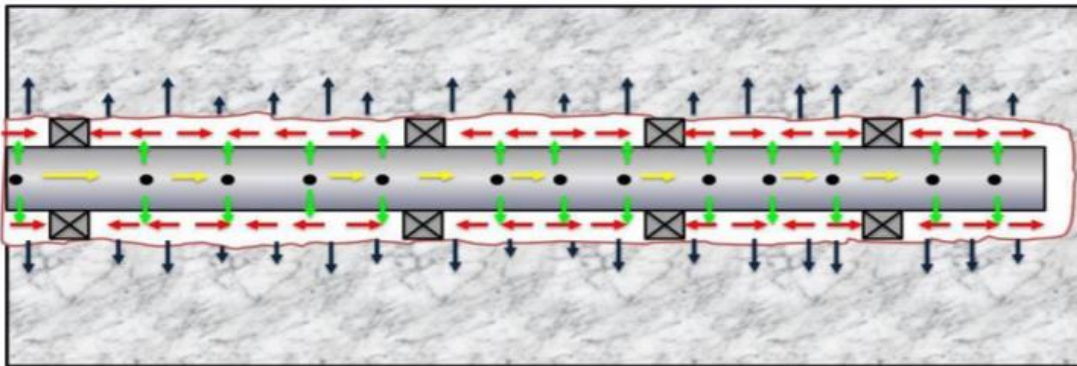
Figure 4 - Flow Pattern in a Limited Entry Liner (Reprinted from Sau et al. (2014))

To design a limited entry liner completion, multiple processes must be properly modeled. These processes include axial fluid flow inside the liner, radial flow from inside the liner into the annulus (orifice flow), axial fluid flow in the annulus, radial flow from the annulus into the reservoir, matrix acidizing wormhole growth, and the skin reduction due to wormhole growth (Sau et al. 2014). By gridding the wellbore and reservoir into discrete sections, the equations that model each of the above processes combined with a numerical algorithm can be used simulate an acid stimulation treatment with a limited entry liner. Simulations can be conducted iteratively to optimize the completion and stimulation treatment design based on reservoir properties and stimulation outcome goals. This simulation strategy was used to successfully design limited entry liner completions in the field (Hosani et al. 2016).

One major uncertainty in the modeling and design effort mentioned above, is the acid-reservoir interaction, or dissolution structure, that occurs near the orifices in a limited entry liner completion. As mentioned earlier, these orifices cause a high-velocity, high-pressure jet to impinge on the borehole wall (Mayer, Sau, and Shuchart 2014). Previous theoretical and experimental research was conducted to examine this process and improve modeling (Beckham, Shuchart, and Buechler 2015, Ndonhong 2014, Holland 2014, Belostrino 2016). Ultimately, the goal is to accurately model dissolution structures in the region near these acid jets so completion and stimulation design can be optimized.

1.4 Experimental Study of Acid Jetting

Three previous experimental studies were conducted to examine the effect of an acid jet on carbonate rock dissolution (Belostrino 2016, Ndonhong 2014, Holland 2014).

7

The seminal acid jetting experiments were performed on 4-inch diameter by 16-inch length Indiana limestone cores (Holland 2014). The study set the baseline acid jetting experimental apparatus and procedure for the studies that followed. The profound result discovered from the experiments was that acid jetting produces a bulb shaped cavity on the inlet side where the acid jet strikes the core (Figure 5). Wormholes extended from the base of the cavities; wormholes broke through the cores at higher interstitial velocities and only partially penetrated the cores at lower interstitial velocities. An additional result from the study was the demonstration that cavities grow with increasing jetting velocity and increasing jetting time. Holland (2014) compared his experiments with previous matrix acidizing experiments performed by Jin (2013) with 4-inch diameter Indiana limestone core at similar conditions. Stoichiometry and the mass of core dissolved were used to calculate pore volumes of acid used to breakthrough. The PV_{bt} vs. v_i plot showed that the acid jetting experiments consumed significantly more acid than conventional matrix acidizing experiments to achieve breakthrough. However, the acid jetting results were not comparable to matrix acidizing results because the acid jetting experiments were conducted with constant pressure differential across the core, where flux was allowed to increase throughout experiments as wormholes grew, and matrix acidizing were conducted with constant pump rates, resulting in constant flux (Holland 2014).
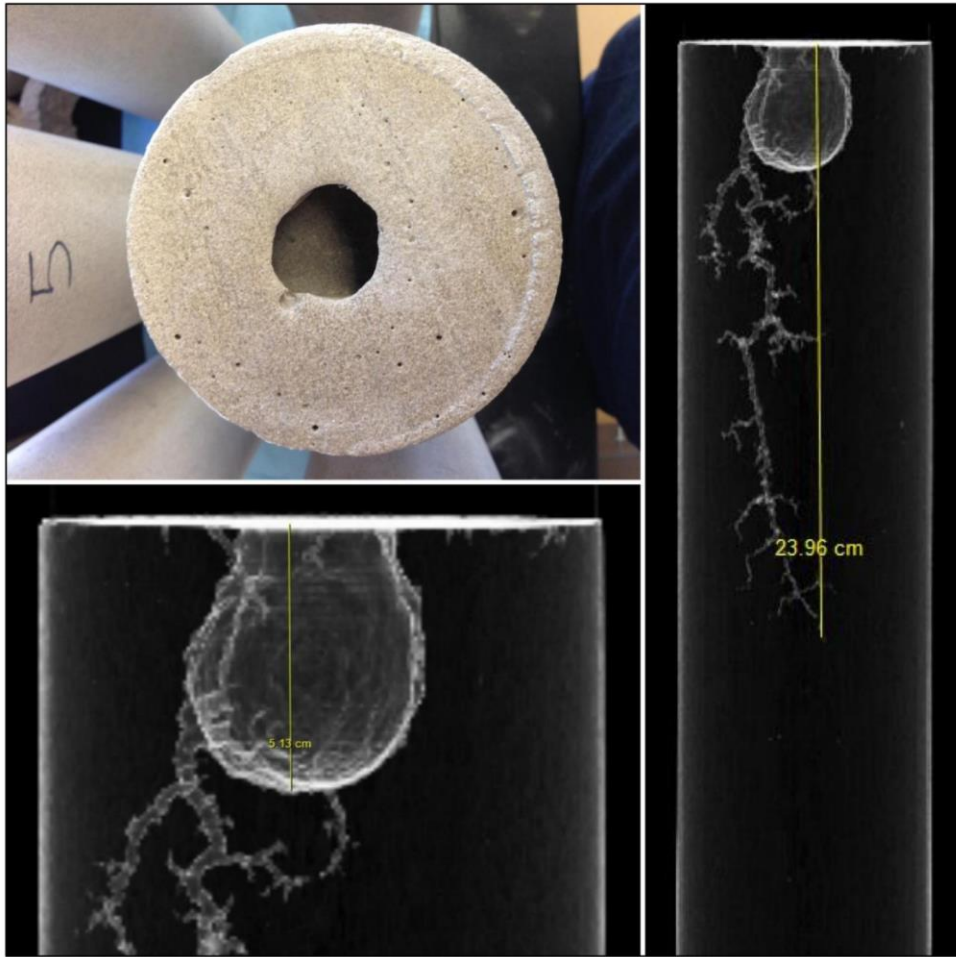
Figure 5 - Bulb-Shaped Cavity and Wormhole Caused by an Acid Jet Impinging on the Core Face: An Example from the Seminal Acid Jetting Experiments (Reprinted from Holland (2014))

The second experimental acid jetting study utilizing the same experimental apparatus and procedure as Holland (2014). The study focused on identifying the parameters that affect mass transfer of acid onto the face of the core and through the core (Ndonhong 2014). Injection rate (jetting velocity), fluid flux (interstitial velocity), permeability, pore distribution, temperature, acid concentration, and injection time were identified as governing parameters. Interstitial velocity was determined to be the primary

factor affecting wormhole propagation. Higher temperature resulted in larger cavity sizes and more branched wormholes; higher permeability had little effect at higher interstitial velocities but produced larger cavities at lower interstitial velocities below the optimum. An uncertainty remaining after Ndonhong (2014) study was whether the cavities and wormholes grow simultaneously.

A multi-stage acid jetting study was conducted using the same experimental apparatus as Holland (2014) but modified the procedure to break the core floods into multiple stages, where in between the stages the core was scanned with a CT scanner to track the development of the cavity and wormholes (Belostrino 2016). The study clearly demonstrated that the cavity and wormholes identified by Holland (2014) and Ndonhong (2014) growth simultaneously (Figure 6). The study demonstrated that wormhole length and cavity volume grew linearly through time; however, the study only featured initial interstitial velocities of ~0.5 cm/min for each stage (Belostrino 2016). An important point is that the average interstitial velocity per stage grew higher each stage.
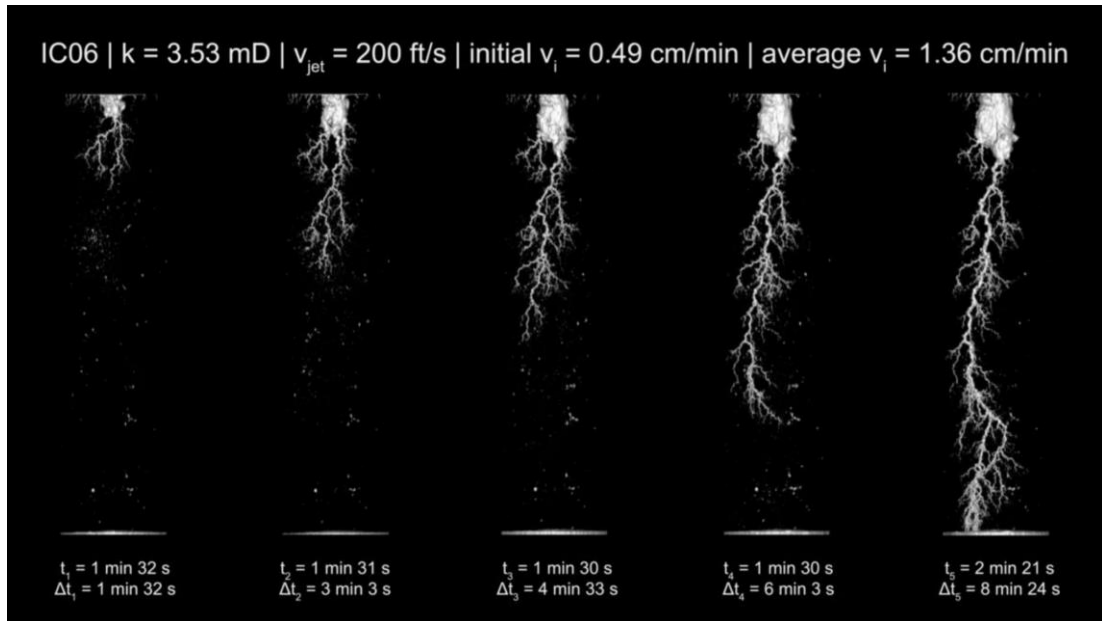
Figure 6 - Simultaneous Growth of Cavities and Wormholes through Time during Multi-stage Acid Jetting Experiment (Reprinted from Belostrino (2016))

1.5 Research Objectives

All of the previous acid jetting experimental studies provided valuable insight into the acid jetting process; however, the experimental apparatus in the previous studies did not provide a mechanism which allowed acid jetting core floods at constant interstitial velocity. Each individual experiment in traditional matrix acidizing experiments is run at constant interstitial velocity, or flux. For each rock-acid-temperature system, a set of these experiments run at various interstitial velocities establishes the wormhole efficiency curve for that system. This so-called wormhole efficiency curve provides the necessary baseline that enables engineers to model matrix acidizing at wellbore scale.

This study amends the experimental apparatus and procedure of Holland (2014) to conduct constant interstitial velocity acid jetting core floods, uses the amended apparatus

and procedure to conduct a constant interstitial velocity experiment set for a rock-acid-temperature system, and outlines three graphical methods to evaluate the acid jetting experiment set in this study in the context of a matrix acidizing experimental set with the same rock-acid-temperature system. The study demonstrates how acid jetting is acid inefficient, confirming the conclusion of Holland (2014), but can increase wormhole growth rate, which is simply defined as the wormhole length, L_{wh}, divided by the jetting time, t_{jet}. The study provides technical reasoning in support of early-time, near-wellbore faster wormhole growth rate near an acid jet, as well as later-time, far-field faster wormhole growth rate near an acid jet in radial geometry. The study additionally provides a theoretical framework and workflow to determine the net effect of acid jetting on wellbore productivity that can be used to inform and optimize the wellbore-scale acid stimulation problem in an open-hole limited entry liner completion.

2. METHODOLOGY

The methodology used in this study will be explained in a chronological context, where (1) the rock core preparation and property measurement, (2) the constant interstitial velocity acid jetting experimental apparatus and procedure, and (3) post-experiment core CT image processing are described and explained.

The rock samples used in this study were 4-inch diameter by 8-inch length, 2-10 mD Indiana limestone from Kocurek Industries. Indiana limestone is a Mississippian-age skeletal grainstone known for its relative homogeneity with respect to other carbonate rocks. Indiana limestone's minerology is almost entirely calcium carbonate ($CaCO_3$ ~ 97.3%) with other trace minerals ($MgCO_3$ ~ 0.4%, Al_2O_3 ~ 0.5%, SiO_2 ~ 1.7%) (Hill 2018). Each core was labeled with an identification code before use.

2.1 Rock Sample Preparation and Property Measurement

2.1.1 Core Water Saturation

After labeling core samples, the dry weight, or weight before water saturation, was obtained. Core samples were then saturated with water before performing permeability measurements and acid jetting experiments. The cores were placed in a PVC pipe tube, shown in Figure 7, then the tube was filled with water. The tube was sealed with a cap that is attached to a Leynold Trivac Model D2a vacuum pump. The vacuum pressure created in the tube by the pump facilitates the evacuation of air from the porosity of the core and saturation with water. Each core was saturated for eight hours (or longer) with a 70 kPa vacuum pressure.

Figure 7 – Vacuum Pump (70 kPa Vacuum Pressure) Evacuates Air from Core Inside White Core Tube Allowing Core to Reach Full Water Saturation

2.1.2 Core Permeability Measurement

After water saturation, each core's permeability was measured using equipment originally described by Grabski (2012) for matrix acidizing core floods; however, when water was pumped instead of hydrochloric acid, the system functions as an efficient means to measure permeability. The equipment used included a 4-inch Hastelloy hassler-type core holder, two accumulators, a syringe pump, a hydraulic hand pump, a back-pressure regulator, and a pressure transducer all connected via tubing and fittings. The pressure

data from the transducer was sent to a LabVIEW program on a computer near the apparatus. A diagram of the apparatus used for permeability testing is shown in Figure 8.
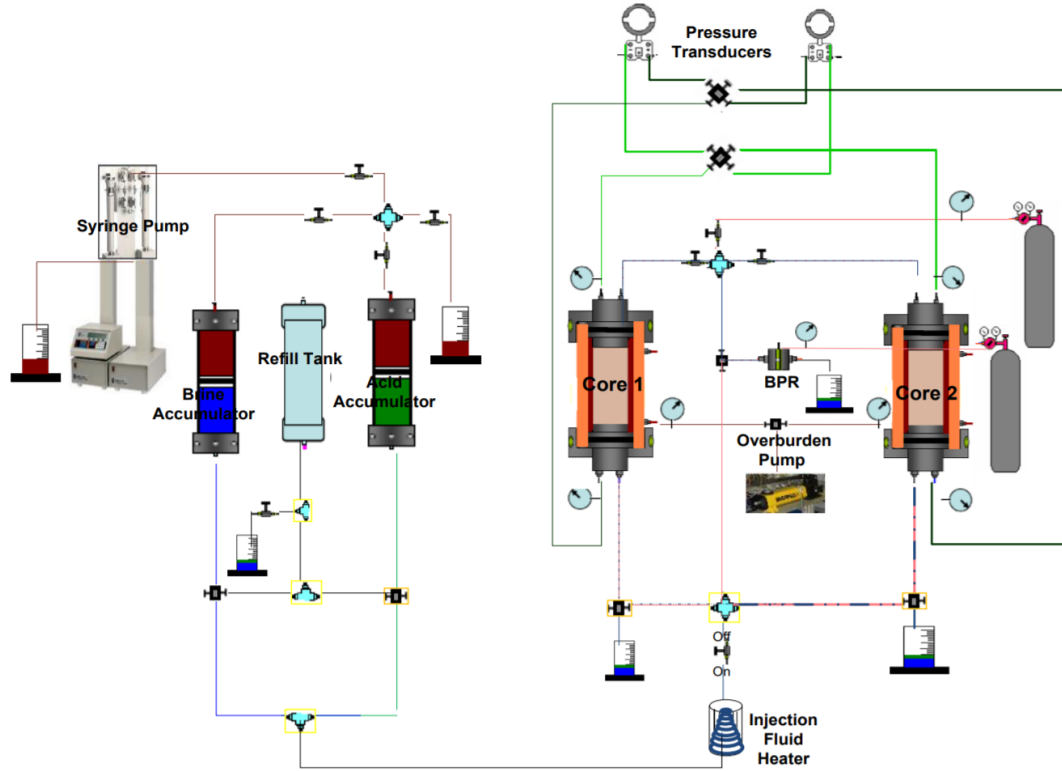
Figure 8 – Core Permeability Measurement Apparatus (Permeability Determined by Measuring Steady-State Pressure Differential Across Core with 10 mL/min Flowrate) (Reprinted from Grabski (2012))

Water was pumped into the core at constant rate utilizing the syringe pump. Once a steady-state condition was attained (i.e. stable differential pressure across core for constant flow rate), permeability was calculated utilizing the linear Darcy flow equation:

$$k = \frac{96.13 QL\mu}{\Delta PA} \qquad (2)$$

where k is permeability in mD, Q is flow rate in mL/min, L is core length in cm, μ is fluid viscosity in cp, ΔP is pressure differential across the core in psi, and A is core cross-sectional are in in^2. A picture of the permeability measurement apparatus is shown in Figure 9. For more information on the permeability apparatus, see Grabski (2012); for more information on the permeability testing procedure, see Holland (2014).

Figure 9 – Permeability Measurement Apparatus

2.1.3 Core Porosity Calculation

Immediately following core permeability measurement, the core's "wet" weight, or weight after water saturation, was obtained. The difference of the core sample dry weight and wet weight along with the core's dimensions provide the necessary information to calculate the effective porosity. Porosity is defined as the pore volume per bulk volume of rock. In the context of this study, the pore volume was calculated by dividing the difference in mass before and after saturation by the saturating fluid's density, in this case, water. The bulk volume was calculated simply using the equation for the volume of a cylinder. This straightforward calculation is presented in Equation 3:

$$\varphi = \frac{V_{pore}}{V_{bulk}} = \frac{\dfrac{m_{wet} - m_{dry}}{\rho_{water}}}{\dfrac{\pi}{4} D_{core}^2 L_{core}} \tag{3}$$

where φ is porosity, V_{pore} is pore volume, V_{bulk} is bulk volume, m_{wet} is the core's saturated mass, m_{dry} is the core's dry mass, ρ_{water} is the density of water, D_{core} is core diameter, and L_{core} is core length. Consistent units are necessary to utilize Equation 3 because porosity is a dimensionless parameter.

2.1.4 Pressure Differential Calculation

Interstitial velocity is an important governing parameter in matrix acidizing experiments and acid jetting experiments (Ndonhong 2014). Equation 1 was rearranged to calculate the needed flowrate to establish in the desired interstitial velocity, and Equation 2 was rearranged to calculate the needed pressure differential to establish the flow rate

calculated via Equation 1. These equations provide an estimate pressure differential for the desired interstitial velocity in each acid jetting experiment.

$$Q = v_i \varphi A \qquad (4)$$

$$\Delta P = \frac{QL\mu}{96.13kA} \qquad (5)$$

2.3 Constant Interstitial Velocity Acid Jetting

2.3.1 Experimental Apparatus

After cores were properly prepared and characterized, the cores underwent constant interstitial velocity acid jetting core floods. The experimental apparatus used to conduct these experiments is fundamentally the same apparatus used by Holland (2014), Ndonhong (2014), and Belostrino (2016). However, a Ohaus Ranger 7000 weight scale and a Badger control valve-Hanbay actuator combo were added to the apparatus, and a new LabVIEW program is used which allows the critical experimental parameter of interstitial velocity to be held approximately constant throughout experiments. For more detailed information about the apparatus equipment specifications other than the newly added equipment used in this study, please refer to Holland (2014).

The principal components of the experimental apparatus were a pulse pump, a core holder, two back pressure regulators, two nitrogen tanks that supply pressure to the back-pressure regulators, a differential pressure transducer, a water tank, a chemical tank, an actuator-control valve combo, a high-precision weight scale, data acquisition hardware, and a LabVIEW program which recorded incoming weight data from the scale and

controled the actuator-control valve during experiments. A diagram of the general experimental setup is shown in Figure 10.
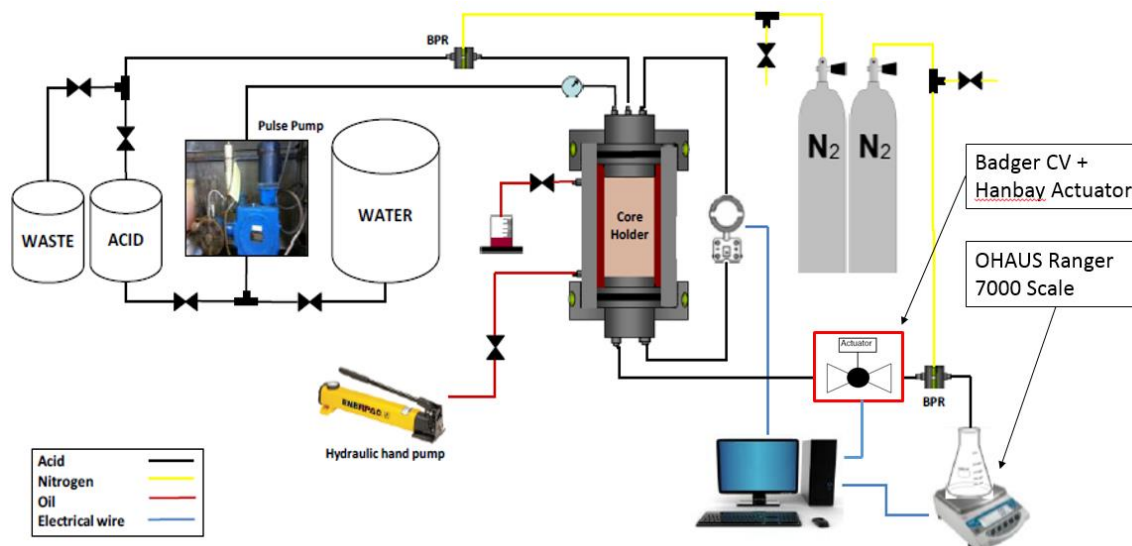
Figure 10 – General Setup of Constant Interstitial Velocity Acid Jetting Experiments Differentiated from Holland (2012) by the Control Valve-Actuator Combo and the High Precision Scale

The Chem/Meter 802 pulse pump, featured in Figure 11, established the appropriate flow rates for desired jetting velocities in experiments; the pump is rated for 16.3 gallons per hour maximum flowrate and 1,900 psi maximum operating pressures. The pump inlet received fluids from the water tank (during pre-flush and post-flush) and from the acid/chemical tank (during acid jetting). The tanks feeding fluids to the pump were controlled via ball valves which were opened or closed "on the fly" to switch from water to acid and vice versa. The pump outlet, or discharge, line was connected to the inlet cap of the core holder.

Figure 11 – Chem/Meter 802 Pulse Pump which Pumps HCl at the Desired Flowrate to Achieve the Desired Jetting Velocity During Experiments

The cross-section of the core holder inlet cap (Figure 12) shows the inlet line which received fluids from the pump, the nozzle attachment which significantly reduces the diameter of the inlet line to 0.0225-inch to create a high velocity jet, the outlet line which accepted fluids that do not enter the core, and the pressure transducer line. The outlet line was connected to the upstream back pressure regulator which was connected to the return line to the waste container. The back-pressure regulator setting determined the upstream pressure on the core during experiments. The distance between the face of the inlet cap and the face of the rock core is 2.25-inch. The open volume created by the distance

between to the inlet cap face and core face was termed the core holder "headspace." The 2.25-inch so-called headspace, established by 2-inch and ¼-inch spacer rings (Figure 13G), contained bulk fluids when pumping began. The nozzle attachment (Figure 13B), is 2.16-inch long; therefore, the standoff distance, or the distance between the nozzle and the rock core face, was 0.09-inch. The standoff distance was equivalent to 4 times the 0.0225-inch diameter of the nozzle.
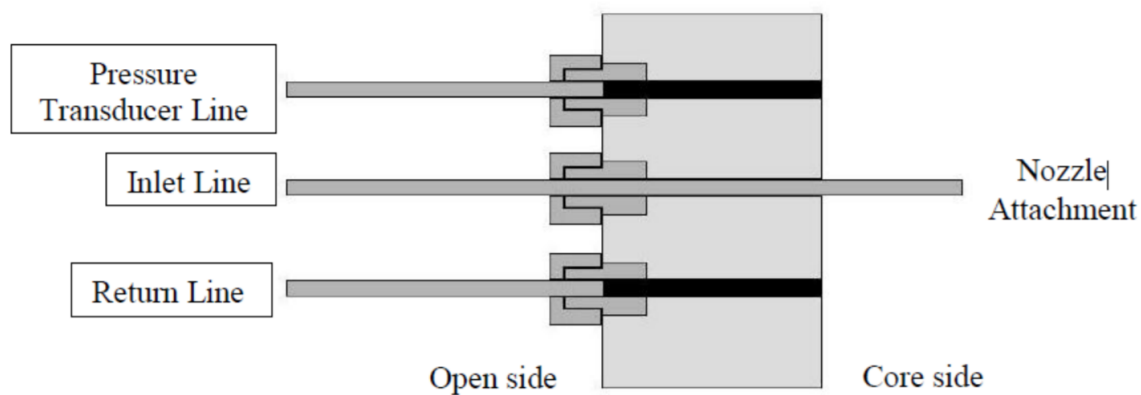
Figure 12 – Cross Section of Core Holder Inlet Cap (Reprinted from Holland (2014))

The inlet cap of the core holder has already been mentioned, but the Hastelloy core holder which securely held the cores during experiments has many parts. The inlet cap, outlet cap, cylindrical body, Viton 70-75 fluoroelastomer interior sleeve, spacer rings, and other components all contributed to proper functioning of the core holder during experiments. All core holder components are shown in Figure 13. An additional component of the core holder was the hydraulic oil that was pumped via an Enerpac P392 hand pump into the space between the cylindrical body and the interior sleeve of the core

holder. The hydraulic oil, Pro-Select AW-32, enabled confining pressure on cores to force fluid into the matrix of cores and prevent fluid "race tracking" around the sides.
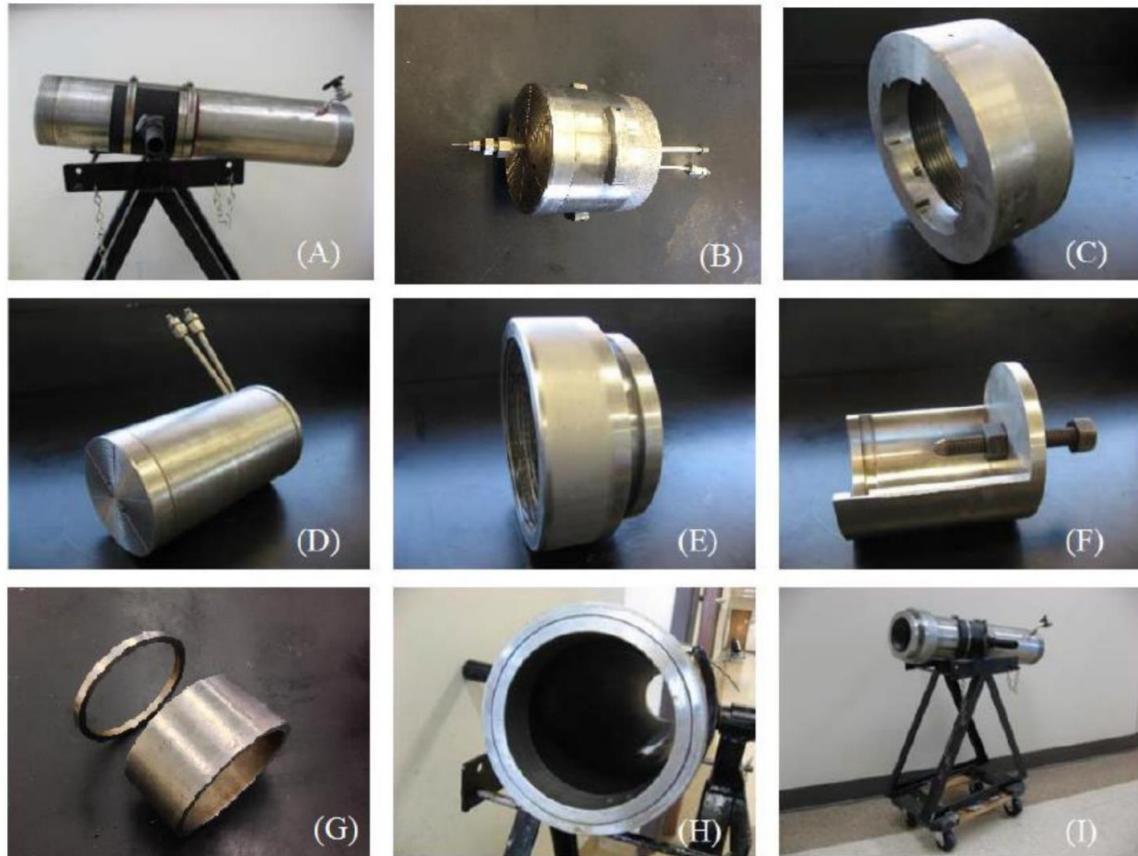
Figure 13 – Hastelloy Core Holder Components (Reprinted from Holland (2014))

There are two lines on the outlet cap of the core holder. One line connects to the differential pressure transducer, and the other line is the fluid effluent line which collects fluid that traveled through the core. The effluent line was first connected to the control valve-actuator (1/4" Badger Hastelloy-C valve-Hanbay LCL-050AB actuator) mentioned earlier, then the line was connected to the downstream pressure regulator, where finally the line was run to a flask which collects the effluent fluid. The flask sat on top of a high

precision weight scale (Ohaus Ranger 7000) which tracked the total weight of the effluent. The weight scale was connected to the lab computer to transmit weight data to LabVIEW, and the actuator was connected to the lab computer to receive valve position data from LabVIEW. The Ohaus Ranger 7000 weight scale and the Badger control valve-Hanbay LCL-050AB actuator combo are shown below (Figure 14).

Figure 14 – Weight Scale and Control Valve-Actuator Combo

2.3.2 Design and Specifications of New Equipment and Software Used in this Study

The Badger control valve-Hanbay actuator combo and the Ohaus Ranger 7000 scale represent the newly added equipment which differentiates the experimental apparatus used in this study from previous acid jetting studies. These pieces of equipment,

23

paired with the LabVIEW software, enable critical process control that maintain interstitial velocity, v_i, approximately constant during experiments. The following discussion provides context on the design and specifications of these pieces of equipment.

The Ohaus Ranger 7000 scale is used to implicitly measure effluent flow rate out of the core, Q_{flux}. The scale is an Ohaus Model R71MHD3. The 0.01 g readability (i.e. precision) of the scale is the most important detail of the scale specifications. The high level of precision allowed the scale to accurately characterize the weight change from the smallest of droplets of fluids that may drop from the effluent line into the flask sitting on the scale. The scale connects to the lab computer via a USB cable. All other specifications for the scale are detailed in Figure 15.

MODEL	R71MHD3	R71MHD6	R71MHD15	R71MHD35
Capacity	3000 g	6000 g	15000 g	35000 g
Readability d	0.01 g	0.02 g	0.1 g	0.1 g
Approved Readability e	0.1 g	0.2 g	1 g	1 g
Repeatability (std. dev.)	0.01 g	0.02 g	0.1 g	0.1 g
Linearity	± 0.02 g	± 0.04 g	± 0.2 g	± 0.2 g
Span Calibration Points	500 g, 1500 g, 2000 g, 3000 g	1000 g, 2000 g, 4000 g, 6000 g	5000 g, 10000 g, 15000 g	10000 g, 20000 g, 30000 g, 35000 g,
Weighing units	gram, kilogram, ounce, pound, pound:ounce, ton			
Applications	Weighing, Parts Counting, Percent Weighing, Check Weighing, Dynamic Weighing, Filling, Formulation, Differential Weighing, Density			
Stabilization time (typical)	Within 1 second			
Display	TFT Graphic LCD			
Display size	4.3 in			
Backlight	White LED			
Communication	RS-422, USB			
Power supply	Power Input: 100-240 V~ 0.5 A 50/60 Hz			
Platform size	240 x 240 mm 9.4 x 9.4 inch		377 x 311 mm 14.8 x 12.2 inch	
Terminal Housing dimensions (W x D x H)	267 x 118 x 72 mm 10.5 x 4.6 x 2.8 in			
Base Housing dimensions (W x D x H)	280 x 280 x 114 mm 11 x 11 x 4.5 inch		377 x 311 x 128 mm 14.9 x 12.2 x 5 inch	
Assembled dimensions (W x D x H)	280 x 420 x 114 mm 11 x 11 x 4.5 inch		377 x 467 x 128 mm 14.9 x 18.4 x 5 inch	
Net weight	7.2 kg / 16 lb		10.9 kg / 24 lb	
Shipping weight	9.2 kg / 20.3 lb		14.4 kg / 31.7 lb	

Figure 15 – Ohaus Ranger 7000 Scale (Model R71MHD3) Specifications

The Ohaus scale allowed the interstitial velocity conditions in the core to be measured and monitored via LabVIEW during experiments. The Badger control valve-Hanbay actuator combo provides the necessary action to maintain interstitial velocity, as defined in Equation 1, approximately constant during experiments. When an increase in interstitial velocity was detected by the scale and displayed real-time in LabVIEW, a user sent a signal to the actuator to close the control valve through the user interface in LabVIEW, and the actuator then received the signal from LabVIEW and closed the control valve, thereby reducing interstitial velocity to the desired value.

The design of the actuator-control valve primarily hinged upon the selection of the control valve type, size, material, and rangeability; once a control valve was selected, an actuator could be matched to accommodate the control valve. The type, size, and material portion of the control valve design was fairly simple. The control valve application used in this study accommodated smaller-scale laboratory experiments which featured highly corrosive acid. To accommodate these needs, the Badger Valve RCV 1001GCTHCSVOOP05HC was used in this study. The control valve was a standard research control valve made of Hastelloy C with ¼ inch diameter.

The design of the rangeability of the control valve was non-trivial, and involved determining the range of flow conditions the valve could accommodate and control precisely. The flow coefficient range, or C_v range, of a valve is a quantitative measure of the range of flow conditions the valve can accommodate. The flow coefficient was defined in Equation 6:

$$C_v = Q \sqrt{\frac{SG}{\Delta P}} \tag{6}$$

where Q was the volumetric flowrate across the valve in gallons per minute, SG was the specific gravity of the fluid flowing through the valve, and ΔP was the pressure differential across the valve in psi. Essentially, the C_v is the gallons per minute of water at 60^0 F that flowed across the valve with 1 psi difference across the valve. The conditions set forth to design the needed C_v range for the experiments in this study were:

- Interstitial velocities ranging from 0.1 cm/min to 2.0 cm/min

- Core permeabilities ranging from 2 mD to 10 mD

- Core porosities ranging from 10% to 15%

- Core lengths 8 in to 16 in

With this in mind, calculations were made to verify if a control valve under consideration met objectives at the extreme end of conditions possible. The flow rate and specific gravity of the fluid fluxing through the core at these conditions, as well as the pressure drop across the control valve at the beginning of the experiments, with no core dissolution, and the pressure drop across the control valve at the end of the experiment, when a wormhole broke through the core (essentially no pressure drop across the core), were calculated to determine the range of C_v conditions the control valve experienced. Ultimately, the Badger control valve used in this study was selected based on its maximum C_v of 0.0004 and its C_v maximum:minimum ratio of 15:0.1.

2.3.3 Experimental Procedure

At the outset of experiments, the selected rock core, identified by its code, was placed inside the core holder. The 2-inch and ¼-inch spacers were placed flush with the core on the inlet side of the core holder. The inlet cap is pushed flush with the spacers and then rotated to be locked into place. Three additional 2-inch spacers were placed on the outlet side of the core and pushed flush with the core. The outlet cap was placed inside the core holder and pushed flush with the spacers. The outlet cap was fastened into place with the component (Figure 13F). The core holder, which was placed on a stand that allows it to be rotated 360 degrees, was rotated such that the inlet side was pointing up and the outlet side was pointing down. All tubing connections between the pump, core holder inlet and outlet, back-pressure regulators, the pressure transducer, hydraulic oil hand pump, and effluent line were properly fastened. The hand pump was used to pump hydraulic oil into the core holder until there is 750 psi confining pressure on the core. Once the core and core holder were setup, and all flowlines were fastened, the acid was prepared.

15% by weight HCl was prepared by combining 1 part 38% by weight HCl (Macron Chemical Company) with 2.81 parts of water in the chemical tank. Variable volumes of acid were prepared based on the pump rate and estimated jetting time to reach breakthrough for each experiment. This was a deviation from the procedure in Holland (2014) where the same amount of acid was prepared for each experiment. The acid that exited the outlet line of the core holder was not routed back to the chemical tank but was instead routed to the waste bucket. Fresh acid of the same concentration was jetted onto cores throughout the entirety of the experiment.

As a safety measure, the acid was poured into the water to prevent chemical reactions. The acid should be prepared under a fume hood, and the preparer should wear a gas mask with a face shield, lab coat with long pants or coveralls, and rubber gloves as a safety precaution. 2% per volume Schlumberger A262 corrosion inhibitor is subsequently mixed into the acid (e.g. if 10 liters of 15% HCl are prepared, 50 mL of corrosion inhibitor is added) with a magnetic stirrer in the chemical tank.

Acid samples were collected from the chemical tank after corrosion inhibitor was added to the acid and before acid pumping began. After acid pumping began, acid samples were taken from the core headspace outlet line which sent fluid to the waste bucket. The samples were placed in 30 mL glass containers that were labeled with the core's identification code plus lettering that identifies when during the experiment the sample was taken. For example, A samples were taken from the tank before acid pumping begins, and B, C, D… samples were taken from the outlet line throughout the experiment. Samples from the outlet line were taken once per minute for the first five minutes of each experiment and once every five minutes after the first five minutes. Each sample was titrated after the conclusion of experiments to obtain acid concentrations throughout the experiment.

After the acid was prepared, the desired flow rate from the pulse pump was calculated. The pulse pump has a knob which allows the user to select between 0-100% of the pump's flow rate capacity. The percentage that corresponded to the desired jetting velocity at the 0.0225-inch nozzle attachment was determined with reference to the diminished pump efficiency per incremental head pressure increase. An approximation of

the needed percentage pump setting for the given head pressure conditions to achieve the desired flowrate was made. The flowrate was then tested under pressure for a 60 second interval to verify, and adjustments are made to the percentage pump setting if necessary. An example calculation below shows how the jetting velocity was determined based on the percentage selected. Again, this was a deviation from the procedure in Holland (2014), where pump inefficiency due to head pressure increases is not considered. The experiments in this study have flow rates from the pump of ~6.1 gallons per hour and jetting velocities of ~80 ft/s.

$$q_{pump} = (q_{max})(capacity\ \%)(efficiency) = \left(16.3\frac{gal}{hr}\right)(0.70)(0.53) = 6.1\frac{gal}{hr}$$

$$\left(6.1\frac{gal}{hr}\right)\left(0.133681\frac{ft^3}{gal}\right)\left(\frac{1\ hr}{3600\ s}\right) = 2.2652\ x\ 10^{-4}\frac{ft^3}{s}$$

$$A_{nozzle} = \frac{\pi}{4}D_{nozzle}^2 = \frac{\pi}{4}\left[(0.0225\ in)\left(\frac{1ft}{12\ in}\right)\right]^2 = 2.7612\ x\ 10^{-6}ft^2$$

$$v_{jet} = \frac{q_{pump}}{A_{nozzle}} = \frac{2.2652\ x\ 10^{-4}\frac{ft^3}{s}}{2.7612\ x\ 10^{-6}\ ft^2} = 82\frac{ft}{s}$$

Once the proper pump capacity was selected, the pulse pump was started which initiated the water pre-flush of the core. The next step in the procedure was to adjust the downstream back-pressure regulator pressure to 1,000 psi, then increase the upstream back-pressure regulator pressure to 1,000 psi in 250 psi increments. After each 250-psi increment increase, the differential pressure across the core was allowed to equalize and the confining pressure was increased 250 psi. Once upstream back pressure regulator was set to 1,000 psi, the confining pressure was 1,500 psi and was maintained 500 psi above

the upstream back-pressure regulator setting when it was increased to create flow across the core.

The differential pressure calculated in core preparation in Equations 4 and 5 was then used to adjust the upstream back-pressure regulator pressure to create the needed differential. Flow was initiated across the core, and water exited the effluent line into the flask. The scale displayed increasing weight as effluent collected in the flask. The testing and adjustments to pump setting and upstream back pressure were made to ensure the pump rate was consistent with 80 ft/s at the jet and interstitial velocity was correct.

At this point in the experimental procedure, the LabVIEW program became a critical tool to execute the experiment. The LabView program was opened and then started by clicking the white arrow in the upper left-hand corner of the user interface (Figure 16). After starting, LabVIEW immediately began receiving the weight data from the scale at a sampling rate of 10 Hz, which was equivalent to 10 weight measurements per second. LabVIEW took the difference between the current weight value then subtracted it from the weight value ten samples before; this weight differential was divided by the time between the samples and an assumed fluid density to calculate a volumetric flowrate. This calculation is represented in Equation 7 below:

$$Q_{flux} = \frac{m_i - m_{i-10}}{\rho_{water} * (10t_s)} \tag{7}$$

where Q_{flux} was the volumetric flowrate of fluid fluxing through the core, m_i was the current weight value being recorded from the scale, m_{i-10} was the weight value recorded ten samples before, t_s was the time interval between samples, and ρ_{water} was the density

of water. This flow rate can be transformed into an equivalent interstitial velocity via an alternative version of Equation 1:

$$v_i = \frac{Q_{flux}}{A\varphi} \tag{8}$$

where v_i was interstitial velocity, Q_{flux} was the effluent flowrate calculated in Equation 7, A was the cross-sectional area of the core, and φ was the core porosity. A moving average of the interstitial velocity using the 100 previous samples was recorded and displayed in LabVIEW (which represents a 10 second moving average of the interstitial velocity).
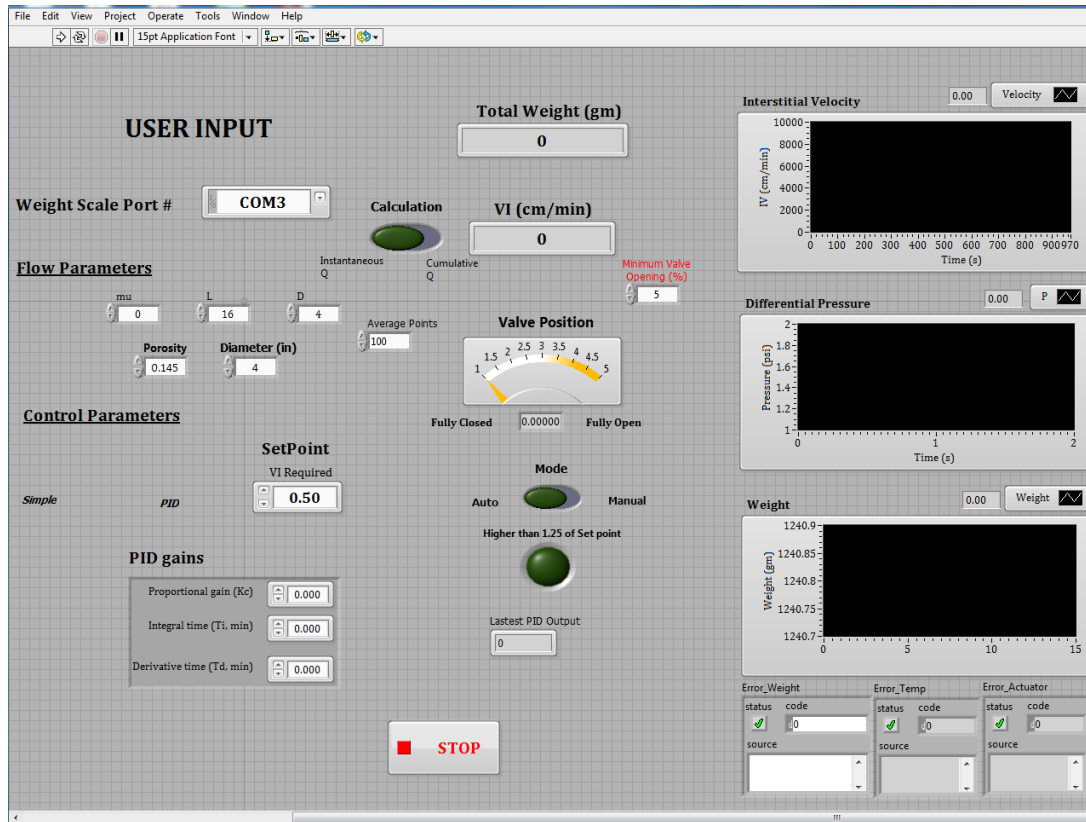
Figure 16 – Constant Interstitial Velocity Acid Jetting LabVIEW User Interface

The displayed interstitial velocity in LabVIEW allowed the user to see whether the differential pressure established across the core needed to be adjusted to achieve the desired interstitial velocity for the experiment. Once the appropriate interstitial velocity was established, the water pre-flush continued for an additional minute to ensure a stable, steady-state interstitial velocity across the core. When steady-state conditions were reached, the pump was changed "on the fly" via the ball valves mentioned earlier to receive acid from the chemical tank, initiating the constant interstitial velocity acid jetting portion of the experiment.

As water was displaced in the flowlines and acid reached the nozzle attachment, a water jet was replaced by an acid jet that struck the core. Previous experimental work shows that once acid jetting begins, a combination of cavity growth and/or wormhole propagation develops depending on the interstitial velocity (Holland 2014, Ndonhong 2014, Belostrino 2016). As wormholes propagate, the initial differential pressure needed for the desired interstitial velocity becomes greater than what is needed to maintain constant interstitial velocity. The reason for this is the reduction in effective length of the core by the length of the dissolution structure, assuming that flow through cavities and/or wormholes has negligible pressure drop relative to flow through the rock matrix. Computational fluid dynamics simulations confirm that this is a reasonable assumption (Beckham, Shuchart, and Buechler 2015).

It is necessary to reduce the differential pressure across the core as wormholes propagate into the core. The control valve-actuator combo in the experimental apparatus enabled this pressure differential reduction. More specifically, the control valve was a

32

needle valve with position settings ranging from fully open (100%) to fully closed (0%). As the valves closes from 100% to 0%, it increased the downstream pressure "felt" at the downstream face of the core, reducing the differential pressure across the core. When the valve was completely closed at 0%, the pressure equalized across the core and the differential pressure became zero allowing zero flow across the core. To avoid this condition, the valve was only allowed to close to a minimum setting of 10%.

The Hanbay actuator, which controlled the position of the needle valve, was connected to the lab computer via a Turck cable. The LabVIEW program used in the experiments was programmed to communicate the desired position of the needle valve to the actuator. The LabVIEW program has two options to communicate this desired valve position: (1) through a proportional-integral-derivative (PID) function or (2) manual input from the user. The second method using manual input from a user was used in this study due to its simplicity and consistency in controlling interstitial velocity, as shown in the experimental data plots in the Appendix.

In either method of controlling the position of the needle valve, the difference between the desired interstitial velocity, which was explicitly input into LabVIEW, and the actual interstitial velocity must be known. In the first method mentioned above where a PID function was used to control the needle valve, the difference between the desired and actual values, or error, was constantly calculated by LabVIEW. The PID parameters were established by several step-test increases in interstitial velocity. Essentially these step-tests determined how much the valve needed to be closed in order to reduce a step increase in the difference between the desired and actual interstitial velocity values. By

33

constantly receiving updated error values for the interstitial velocity, the PID function in LabVIEW constantly updated the needle valve position communicated to the actuator needed to achieve the desired interstitial velocity. To summarize, the PID function method of controlling interstitial velocity created a feedback loop where the weight data sent from the scale to the computer was interpreted by LabVIEW to communicate a needle valve position from the computer to the actuator to maintain constant interstitial velocity.

The manual input method of controlling the interstitial velocity was much simpler than the PID function option. The manual input method required a user to monitor the actual interstitial velocity value being displayed by LabVIEW. When the displayed, or actual, interstitial velocity reached a predetermined percent deviation or absolute error from the desired value, the displayed interstitial velocity became red, indicating to the user the needle valve needed to be closed to reduce the flux rate through the core. The user closed the needle valve in stepwise fashion by explicitly entering a valve position until the actual interstitial velocity was reduced to the desired value. In this study, the needle valve position was closed in 1% increments until the desired interstitial velocity was achieved. In either method of valve position/interstitial velocity control, the interstitial velocity can be maintained within +/- 0.05 cm/min of the desired value.

Using either of the methods mentioned above, constant interstitial velocity acid jetting of the core occured until wormholes brokethrough the core or a predetermined time is reached. Acid jetting was ended by switching the pump "on the fly" back to water, initiating the water post-flush of the core. The upstream back-pressure regulator pressure was reduced to zero by bleeding down the pressure in the tubing connecting the nitrogen

tanks to the upstream back-pressure regulator. Both of these steps were necessary to evacuate acid out of core and flush any remaining acid out of the core and/or flowlines. The water post-flush lasted for ten minutes. The pump was then shut down, flowlines/tubing were disconnected, the core holder inlet and outlet caps were removed, and the core was removed from the core holder. The core was then weighed to determine the mass of rock dissolved during the experiment. The last step in the experimental procedure was to bring the core to the Toshiba Aquilion TSX-101A/RG X-ray CT machine for scanning and process the CT images to enable 3D viewing of the dissolution structure.

2.4 CT Image Processing

A detailed workflow was established for processing CT images of cores that had undergone acid jetting core flood experiments (Belostrino 2016). The workflow allowed 3D image and video renderings of dissolution structures and measurement of dissolved cavity volume, cavity depth, wormhole length (cavity depth plus additional wormhole propagation length), and total dissolution volume. An in-depth, detailed discussion of the CT image processing methodology used in this study is in Belostrino (2016); for simplicity, a succinct summary of the workflow is presented here:

The raw CT image files produced by the Toshiba CT machine are classified as DICOM files, or Digital Imaging and Communications in Medicine files. Obviously, the typical purpose of processing and interpreting CT images is for medical purposes; however, this same processing power can be used to interpret rock properties, in this specific instance the dissolution structures within a rock core produced from an acid jetting

core flood. Each DICOM file represents a thin, cross-sectional slice of the rock core. Each slice image is characterized by pixels of a range of values, where positive pixel values indicate high density material (i.e. solid rock matrix material) appearing as white and negative positive pixel values indicate low density material (i.e. rock pore space or dissolution structures) appearing as black.

The CT machine produces four types of these cross-sectional slices with varying levels contrast, resolution, focus and slice thickness. The image type which produces the highest resolution and lowest contrast level is used so even the smallest diameter wormholes are detected in the processing. A MacOS based open source software, Horos, is used to process the CT images. Essentially, Horos allows a user to manipulate two ranges of pixel values, one representing bulk rock material and one representing dissolved rock volume, to be set to alternate pixel values. In this case, the dissolved rock volume range of pixel values is set to appear white, and the bulk rock material is set to appear black, thus allowing a visualization of the dissolution structure within the rock core (Figure 17). Through additional built-in functionality within Horos, cavity volume, cavity depth, wormhole length, and total dissolution volume can be determined (Figure 18).
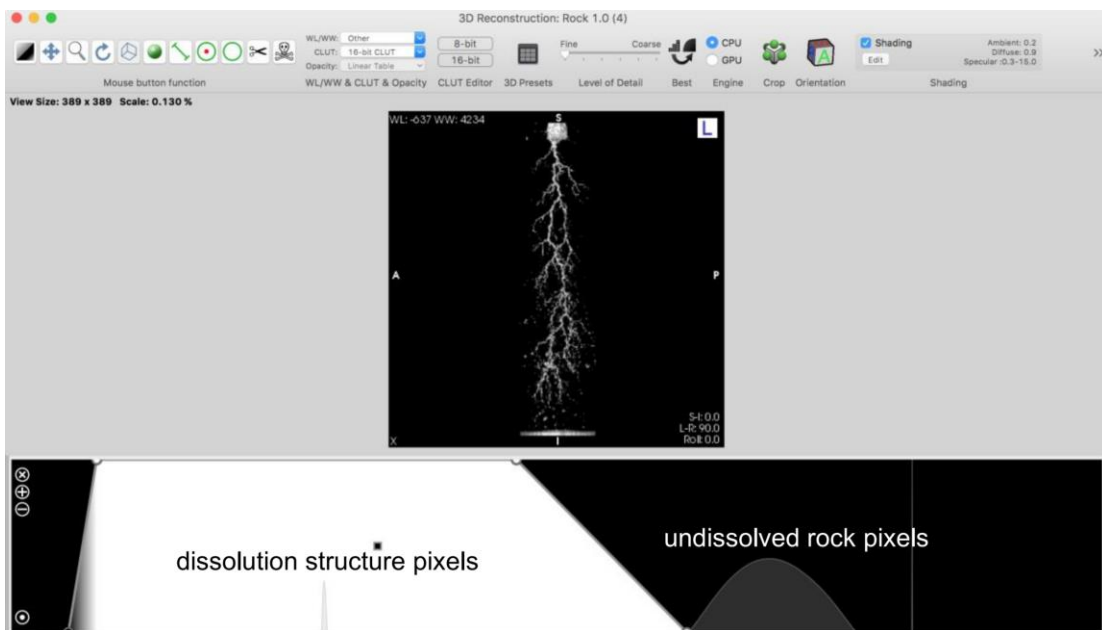
Figure 17 – 3D Volume Rendering of Rock Core Dissolution Structure (Reprinted from Belostrino (2016))
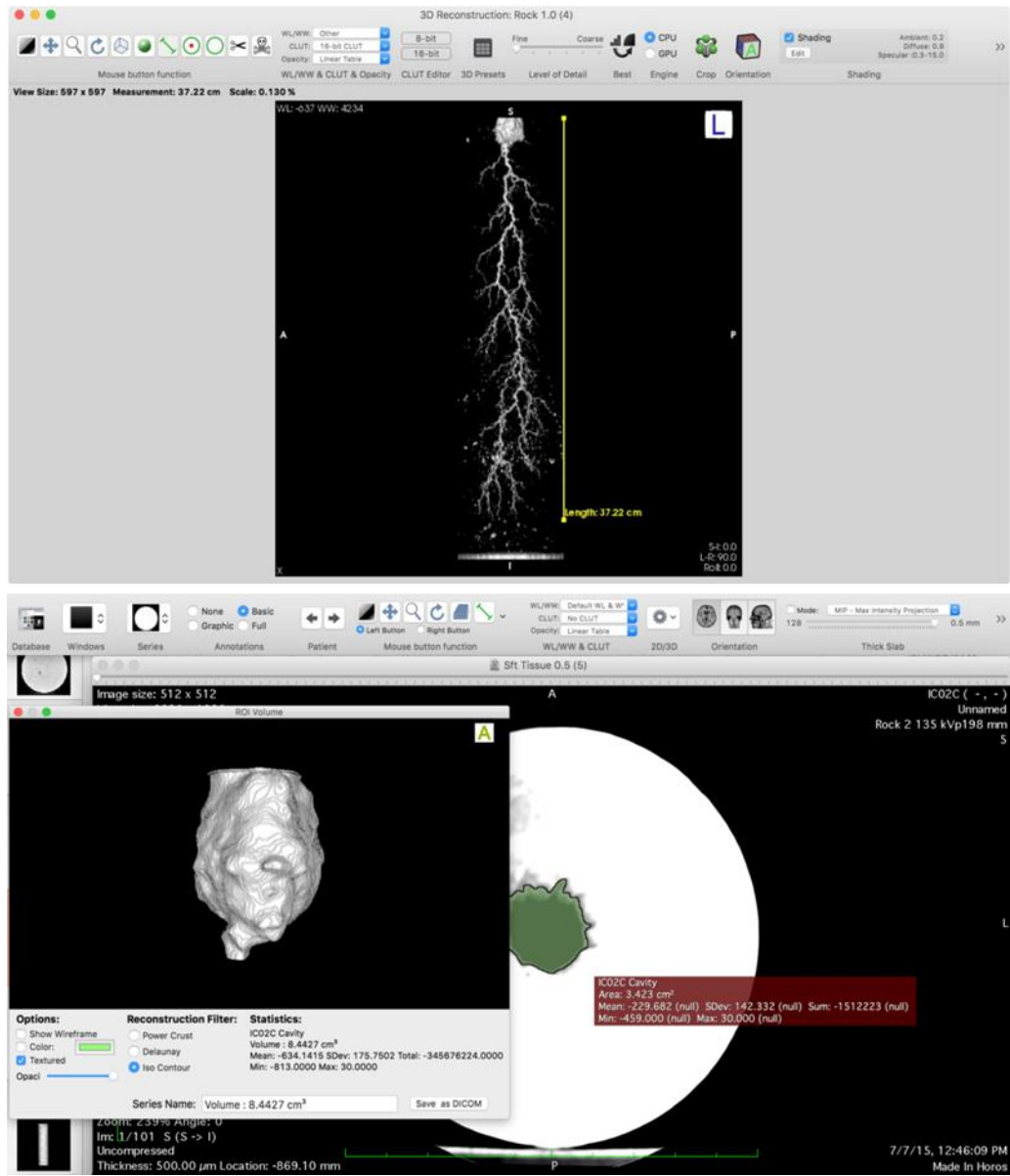
Figure 18 – Wormhole Length and Cavity Volume Calculation with Horos Software (Reprinted from Belostrino (2016))

3. RESULTS AND DISSCUSSION

3.1 Matrix Acidizing Theory and the Wormhole Efficiency Curve

In matrix acidizing laboratory experiments of carbonate cores, acid is pumped into the cores at constant rate until a wormhole breaks through the core, where the total volume of acid pumped is known. In matrix acidizing experiments, there is no headspace, or bulk fluid volume, between inlet of the core holder and the core face, and there is no outlet line for fluid to evacuate the headspace, as in the acid jetting experiments in this study. In matrix acidizing experiments, v_i, or interstitial velocity, is easily calculated by Equation 1, and, PV_{bt}, or pore volumes to break through, is a dimensionless number which represents the multiple of core pore volume of acid which is pumped to propagate a wormhole through the core. PV_{bt} can be calculated with the following simple equation:

$$PV_{bt} = \frac{V_{acid}}{V_{pore}} = \frac{V_{acid}}{\left(\frac{\pi}{4} D_{core}^2 L_{core}\right) * \varphi} \qquad \textbf{(9)}$$

Equation 9 is straightforward for matrix acidizing experiments because acid is simply pumped into the cores at constant rate needed to achieve the desired V_i, therefore the total acid volume is easily calculated or directly measured. Once again, all acid pumped is fluxed through the core. If the wormhole front does not break through the entire core, Equation 9 becomes:

$$PV_{bt} = \frac{V_{acid}}{V_{pore}} = \frac{V_{acid}}{\left(\frac{\pi}{4} D_{core}^2 L_{wh}\right) * \varphi} \qquad \textbf{(10)}$$

where wormhole length, L_{wh}, is substituted for core length, L_{core}.

In matrix acidizing of carbonate rocks, surface reaction rate between HCl and a carbonate formation is typically high. This condition creates a situation where the creation and propagation of wormholes is a transport limited, diffusion controlled process (Buijse and Glasenbergen 2005, Buijse 1997). The condition of transport limited acid spending is what creates and explains wormhole growth's intimate dependency on interstitial velocity, which serves as a proxy for injection rate in matrix acidizing. Although injection rate increases may result in higher fluid loss from wormholes into the rock matrix, an increase in injection rate will cause higher acid flux at wormhole tips resulting in higher wormhole growth rates. At low injection rates, short wormholes or no wormholes propagate in a dissolution regime termed compact dissolution; at optimum injection rates, dominant wormholes propagate due to an optimal transport condition where enough acid reaches the wormhole tip to create a more singular wormhole without significant side branching; and at high injection rates, high amounts of acid reach wormholes tips creating notable tip splitting and wormhole branching (Buijse and Glasenbergen 2005).

When a set of carbonate matrix acidizing core flood experiments with the same acid-rock-temperature system is conducted at various interstitial velocities, the various dissolution regimes discussed above can be modeled quantitatively via the PV_{bt} parameter. A log-log plot of PV_{bt} vs. v_i values from matrix acidizing core floods can be fit to the Buijse and Glasenbergen (2005) model. After fitting the wormhole efficiency curve to the experimental data, one can clearly visualize the three wormhole regimes. Significant acid efficiency is gained by increasing interstitial velocity to the optimum

interstitial velocity, and minimal acid efficiency is lost by increasing interstitial velocity above the optimum interstitial velocity.

One exception to the previous comment about minimal loss of acid efficiency occurs as the dissolution regime changes from highly branched wormholes experiencing severe tip splitting to ramified wormholes where conditions approach uniform dissolution (Figure 19) (Fredd and Fogler 1999). The injection rate and interstitial velocity associated with the ramified wormhole regime does not represent a desired condition in matrix acidizing treatments at the field scale; however, this dissolution regime may be comparable to the cavity dissolution regime observed in acid jetting core flood experiments, which is discussed below.
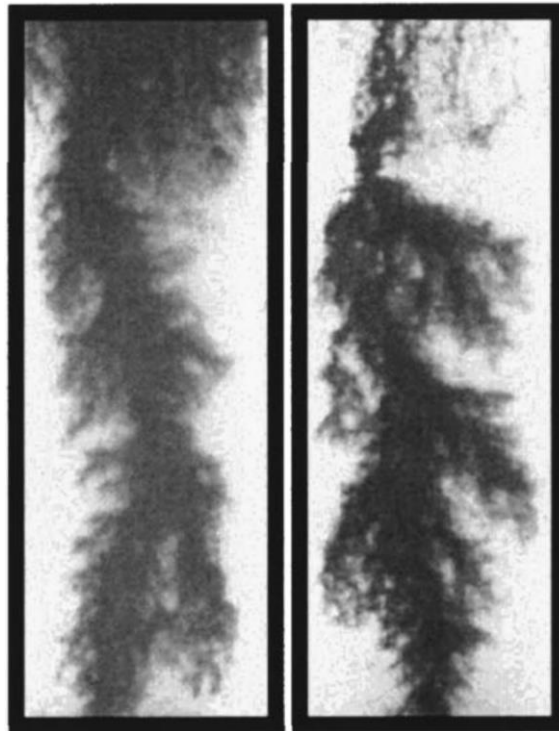
Figure 19 – Ramified Wormholes in High Interstitial Velocity Matrix Acidizing Experiments (Reprinted from Fredd and Fogler (1999))

Four matrix acidizing core flood experiments were conducted with 4-inch diameter x 8-inch length low permeability Indiana Limestone cores with 15% by weight HCl acid at room temperature (75º F) (Jin 2013). A summary of the experiments is featured in Table 1. Additionally, Jin (2013) used the Buijse and Glasenbergen (2005) wormhole growth model to fit a wormhole efficiency curve to the experimental data (Figure 20). In this study, acid jetting experiments were run with the same rock-acid-temperature system as the matrix acidizing experiments of Jin (2013). The differences between the matrix acidizing experiments and acid jetting experiments are evaluated and the differences of the experimental results are evaluated for potential implications on wellbore scale acid stimulation.

Because of the distinct differences between matrix acidizing and acid jetting experiments, a cautioned approach is used to not directly compare the experimental data from each study, but to rather use the contrast between the results to inform and understand the differences in the physical processes occurring in the two different experiments.

Table 1 – Indiana Limestone Matrix Acidizing Data (Reprinted from Jin (2013))

Core#	Perm(mD)	Porosity	Acid injection rate(ml/min)	Interstitial Velocity(cm/min)	PVbt
1	2.5	14.53	6.3	0.53	0.34
2	0.55	14.46	10.5	0.90	0.22
3	0.86	14.74	35.1	2.94	0.28
4	0.86	14.3	3.5	0.30	1.47
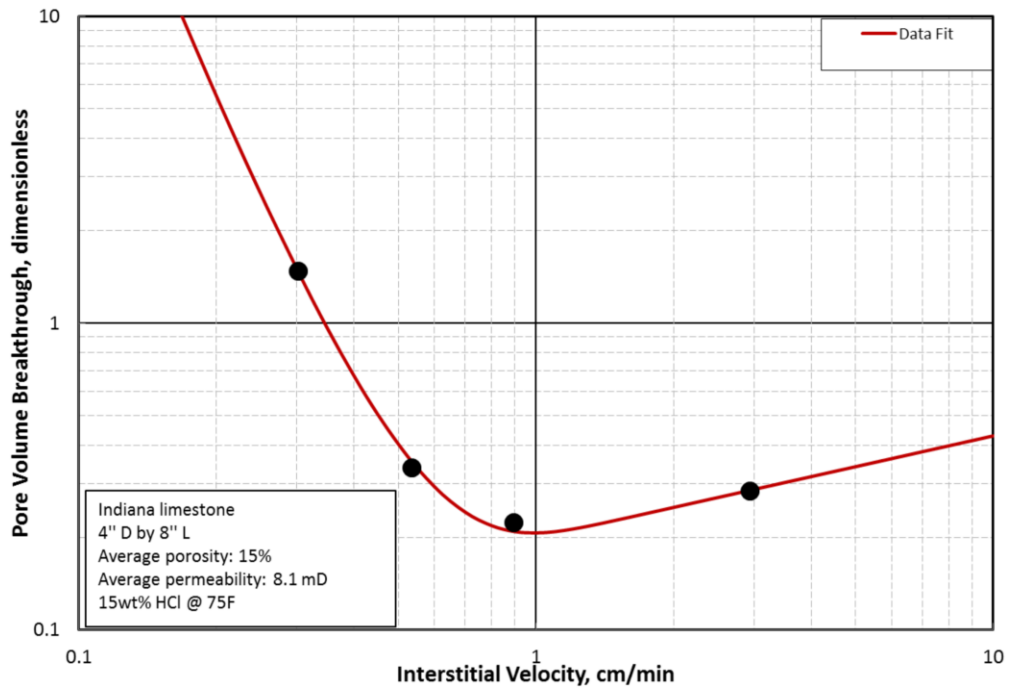
Figure 20 – Indiana Limestone Matrix Acidizing Wormhole Efficiency Curve (Reprinted from Jin (2013))

3.2 Acid Jetting Experimental Data Set

The conditions of lower permeability, 4-inch diameter by 8-inch length Indiana Limestone cores, 15% HCl, and room temperature system used in this acid jetting core flood study is very similar to Jin's work, as mentioned above. Table 2 provides a more detailed characterization of the cores used in this study and the conditions of the experiment associated with each core. Each experiment was conducted using the methodology explained above.

Table 2 - Core Characterization & Experimental Conditions

	inch	inch	%	mD	cm/min	ft/s
Core ID	**L**	**D**	**ϕ**	**k**	**Vi**	**Vjet**
1	7.75	4	14.91%	4.02	0.4	80
2	7.75	4	14.16%	2.53	0.2	80
3	7.875	4	13.81%	2	0.12	80
4	7.75	4	15.92%	5.72	0.71	80
5	7.875	4	15.91%	9.91	2	80
6	7.875	4	15.42%	8.89	1.11	80

Each experiment had a wormhole that broke entirely through the core except for Core 3, which was conducted at the lowest interstitial velocity (0.12 cm/min). The experiment was ended prior to break through because a confining pressure increase was observed on the hydraulic oil line, an indicator in previous experiments that the cavity is approaching the side of the core. When the cavity grows all the way to the side of the core contacting the sleeve, it causes a sleeve failure and a potentially faulty experiment result. For Core XX03, the wormhole length was determined using the CT image processing.

Each core had a cavity after the experiments. The cavity volume and depth were determined for each experiment with CT image processing. The total dissolution volume, including the cavity and the wormholes, was also determined for each experiment. Table 3 provides these details.

Table 3 - Experimental Results

	cm/min	ft/s	min	inch	cm		cc	cc	
ID	v_i	v_{jet}	t_{jet}	L_{wh}	D_{cavity}	D_{cavity}/L_{wh}	V_{cavity}	$V_{cavity + wh}$	%Vcav
1	0.40	80	14.00	7.75	4.41	22%	36.41	40.80	89%
2	0.20	80	22.53	7.75	5.63	29%	58.36	61.85	94%
3	0.12	80	32.28	6.264	8.30	52%	142.15	143.54	99%
4	0.71	80	8.38	7.75	3.34	17%	15.21	20.51	74%
5	2.00	80	3.52	7.875	4.50	22%	24.55	32.00	77%
6	1.11	80	6.17	7.875	3.18	16%	13.99	20.66	68%

The data provided in Tables 2 and 3 allows the calculation of other parameters, including PV_{bt}, v_i/v_{wh} ratio, and v_{wh}, all of which allow deeper evaluation and analysis of the acid jetting results. An explanation of these parameters, how they are calculated, and the implication of their graphical representation when plotted versus v_i is given in the next section.

3.3 Methods of Evaluation for Acid Jetting

With the proper background on matrix acidizing, the methods of evaluating experimental acid jetting results with reference to experimental matrix acidizing results can be examined. Essentially, two curves are used to evaluate acid jetting: (1) the wormhole efficiency curve typically used to characterize matrix acidizing experiments; and (2) a new curve, the "normalized wormhole growth rate" curve. Additionally, acid jetting and matrix acidizing can be evaluated with a third plot where wormhole velocity, v_{wh}, is plotted against v_i. v_{wh} is simply the wormhole length, L_{wh}, which includes the depth of the cavity, divided by the experiment jetting time, t_{jet}. v_i is defined in Equation

1, and the methodology to calculate Q_{flux} needed to calculate v_i is discussed in the Methodology section.

The first method of evaluation, the wormhole efficiency curve, plots the PV_{bt} parameter, which captures wormhole propagation length per a normalized volume of acid used, plotted versus v_i. When using PV_{bt} as an evaluation mechanism, acid volume minimization per productivity increase (i.e. wormhole length) is the objective.

The second method of evaluation, the normalized wormhole growth rate curve, utilizes the v_i/v_{wh} ratio of acid jetting experiments and the v_i/v_{wh} of matrix acidizing experiments plotted versus v_i. In matrix acidizing experiments, the v_i/v_{wh} ratio is simply equivalent to the PV_{bt} value; therefore, the normalized wormhole growth rate curve is the same as the wormhole efficiency curve. In acid jetting the PV_{bt} value is not equal to the v_i/v_{wh} value. It is suggested that using the v_i/v_{wh} ratio is meaningless and that v_{wh} should simply be compared; however, the v_i/v_{wh} ratio provides a plot with a similar shape to the wormhole efficiency curve, which is familiar to more people. Also, the optimum v_i/v_{wh} ratio and optimum v_i observed from the normalized wormhole growth rate plot are necessary to fit the Buijse and Glasenbergen (2005) wormhole growth model to the acid jetting experimental data. When using the v_i/v_{wh} ratio as an evaluation mechanism, the objective is to maximize productivity increase (i.e. wormhole length) without regards to the volume of acid used. It is critically important to distinguish a normalized wormhole growth rate curve, which uses v_i/v_{wh} ratio, from a wormhole efficiency curve, which uses PV_{bt}, because they represent two different objective functions.

The third method of evaluation is essentially a simpler version of the second method and utilizes plotting v_{wh} versus v_i. In all methods put forth, the goal is to provide an evaluation of parameters over a range of v_i conditions.

3.2.1 PV_{bt}

Just like with matrix acidizing experiments, PV_{bt} can be calculated for acid jetting experiments albeit not with direct measurement but with calculations. A method was developed to calculate PV_{bt} in Indiana Limestone acid jetting experiments utilizing the volumetric dissolving power, x, which is a dimensionless parameter that represents a volume of mineral dissolved per volume of acid solution (Holland 2014). The unique mineralogy of Indiana Limestone (almost entirely $CaCO_3$) allows one to appropriately assume the reaction kinetics are strictly defined between HCl and $CaCO_3$. The reaction of HCl and $CaCO_3$ is defined in the stoichiometry in Equation 11.

$$2HCl + CaCO_3 \rightarrow CaCl_2 + CO_2 + H_2O \qquad \textbf{(11)}$$
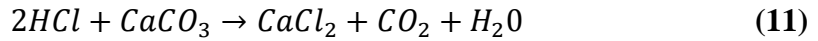
The dissolving power is determined with the following equations:

$$x = \beta \left(\frac{\rho_{acid\ solution}}{\rho_{mineral}} \right) \qquad \textbf{(12)}$$

$$\beta = \frac{v_{mineral} * MW_{mineral}}{v_{acid} * MW_{acid}} \qquad \textbf{(13)}$$

where x is volumetric dissolving power, β is the mass dissolving power, $\rho_{acid\ solution}$ is the density of the diluted acid solution, $\rho_{mineral}$ is the density of the mineral being reacted, $v_{mineral}$ and v_{acid} are the stoichiometric constants in Equation 11, and $MW_{mineral}$ and

MW_{acid} are the molecular weights of the mineral and acid. For 15% by weight HCl and

Indiana Limestone the volumetric dissolving is calculated to be the following:

$$\beta_{100} = \frac{(1)*(100.1)}{(2)*(36.6)} = 1.37 \; \frac{g \; CaCO_3}{g \; HCl}$$

$$\beta_{15} = 0.15 * \beta_{100} = 0.21 \; \frac{g \; CaCO_3}{g \; HCl}$$

$$x_{15} = \beta_{15} \left(\frac{\rho_{acid \; solution}}{\rho_{mineral}} \right) = 1.37 \; \frac{g \; CaCO_3}{g \; HCl} * \left(\frac{1.07 \frac{g}{cm^3}}{2.71 \frac{g}{cm^3}} \right)$$

$$x_{15} = 0.0829 \; \frac{cm^3 \; CaCO_3}{cm^3 \; HCl}$$

With the volumetric dissolving coefficient determined for the Indiana Limestone-

15% HCl system, the volume of rock dissolved in an acid jetting experiment can be used

to calculate the volume of acid used in the dissolution. Holland (2014) back calculated the

volume of $CaCO_3$ dissolved in acid jetting by using the change in core mass before and

after acid jetting; however, in this study we used the CT image processing methodology

described to explicitly measure the volume of rock dissolved during the acid jetting

experiment. It is critically important to correct the bulk volume of rock dissolved measured

in the CT image processing by adjusting it to account for pore volume within the total bulk

rock volume dissolved as demonstrated in Equation 14:

$$V_{CaCO_3,dissolved} = V_{bulk,dissolved} * (1 - \varphi) \tag{14}$$

where $V_{CaCO_3,dissolved}$ is the net volume of calcium carbonate dissolved during acid

jetting, $V_{bulk,dissolved}$ is the bulk volume of rock dissolved during acid jetting determined

by CT image processing, and φ is core porosity. After correction for porosity, the

calculated net volume of CaCO₃ dissolved in acid jetting can be transformed into the volume of HCl used:

$$V_{HCl\ 15\%} = \frac{V_{CaCO_3, dissolved}}{x_{15}} \qquad (15)$$

PV_{bt} is then calculated:

$$PV_{bt} = \frac{V_{HCl\ 15\%}}{V_{pore}} \qquad (16)$$

where V_{pore} is core pore volume calculated via Equation 8 or 9. The $V_{HCl\ 15\%}$ parameter in Equation 16 includes the volume of acid used to dissolve the cavity as well as any wormholes in the experiment.

Figure 21 shows that PV_{bt} values for acid jetting experiments are approximately equal to matrix acidizing experiments at low interstitial velocity in the compact dissolution regime and much higher than the PV_{bt} values of the matrix acidizing experiments at optimum and high interstitial velocities. The PV_{bt} values of acid jetting are highly dependent on the cavity volume generated during the experiment. The cavity volume growth rate has an approximately linear relationship with the total volume of acid jetted on a log-log plot indicating a power law relationship; the total volume of acid jetted is directly proportional to the jetting velocity and jetting time. This result is consistent with the conclusion of Holland (2014) and reinforces that acid jetting is inherently acid intensive and consumes more acid per length of wormhole generated than matrix acidizing, especially at interstitial velocities approaching or above the optimum.

An interesting result to note from Figure 21, below, is that acid jetting's optimum apparent v_i when using the PV_{bt} parameter is 1 cm/min, similar to the optimum for matrix acidizing experiments. The optimum point for acid jetting is the point which balances quicker wormhole growth (less time to break through therefore smaller cavity) with inefficiency creating the wormhole at higher v_i conditions.
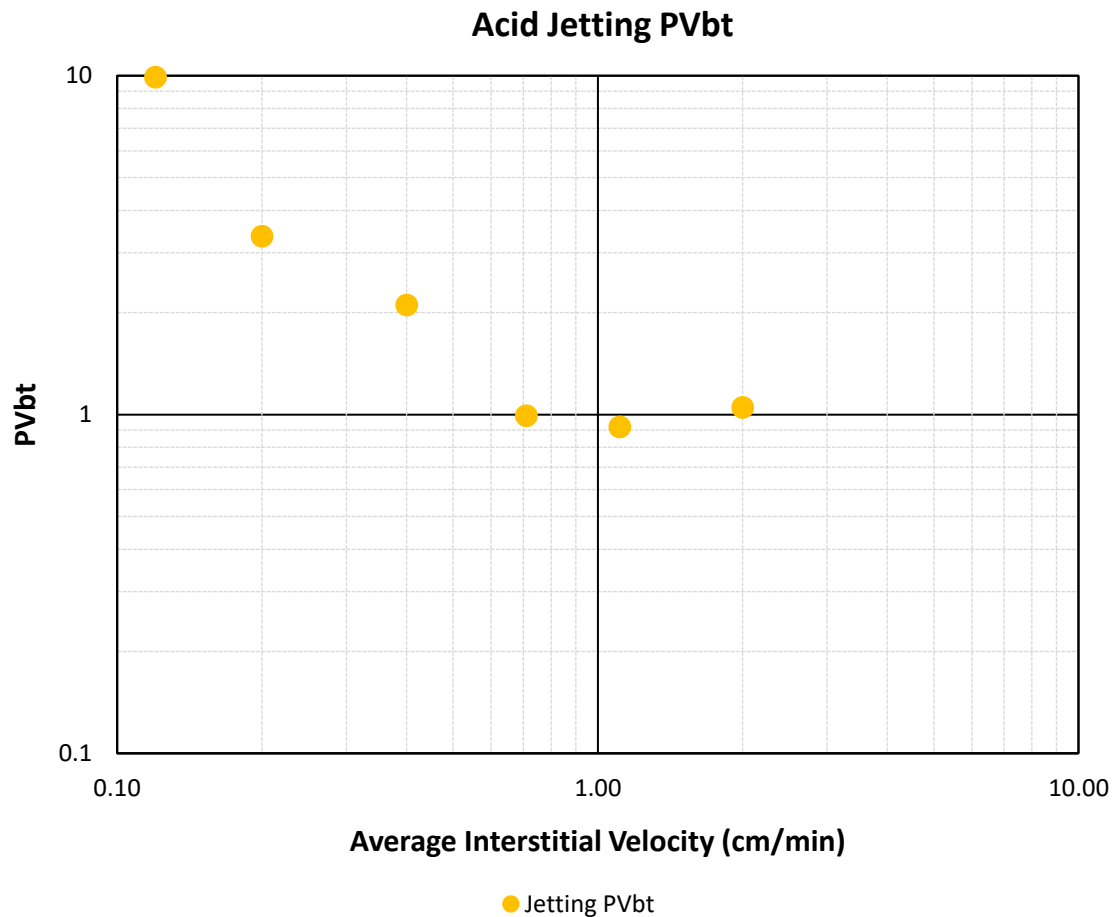
Acid Jetting PVbt

Figure 21 – Acid Jetting PVbt Plot Showing Increasing Volumetric Acid Efficiency with Increasing Interstitial Velocity Until ~2 cm/min Interstitial Velocity

3.2.2 v_i/v_{wh} Ratio

In matrix acidizing experiments, pore volumes to break through, PV_{bt}, interstitial velocity, v_i, and wormhole velocity (or growth rate), v_{wh}, are related by the following equation (Buijse and Glasenbergen 2005):

$$PV_{bt} = \frac{v_i}{v_{wh}} \tag{17}$$

This relationship is based on the assumption that v_{wh} is not the growth rate of a single wormhole but the average growth rate of a wormhole front. When PV_{bt} is calculated as discussed above, and v_{wh} is calculated (Equation 18) as the length of the farthest extending wormhole tip from the inlet face of the core, L_{wh}, divided by the acid jetting time, t_{jet}, the relationship in Equation 17 does not exist for acid jetting experiments.

$$v_{wh} = \frac{L_{wh}}{t_{jet}} \tag{18}$$

The break down in the $\frac{v_i}{v_{wh}}$ relationship is shown in Figure 22. PV_{bt} values of acid jetting experiments are higher than the values of v_i/v_{wh}. The highly localized acid leak-off and turbulence where the acid jet strikes the core face is a likely partial explanation of why the relationship in Equation 17 does not exist for acid jetting. In carbonate matrix acidizing, wormhole initiation and propagation are dependent on the localized leak-off of acid in the most porous and permeable portions of rock among other factors. This localized leak-off is completely determined by the rock heterogeneity and rock properties of the core used. Basically, acid has equal access to the entire cross-sectional area of the core in matrix acidizing, and wormholes will travel roughly as a uniform front.

Cavities, a clear consequence of the localized acid leak-off and turbulence generated by the jet, are not a feature in matrix acidizing and demonstrate a deviation from plug flow conditions where wormholes travel as an approximately uniform front. In acid jetting, the localized leak-off which initiates and propagates cavities and wormholes is artificially created by the jet's velocity and pressure impingement on a finite area of the core's inlet face. Cavities form at the acid jet impingement location, wormholes initiate from the base of the cavity, then wormholes propagate via a continuous supply of fresh HCl jetted into the cavity. The singular, localized source of acid in acid jetting may cause the local interstitial velocity "felt" by the wormholes to be greater than the apparent interstitial velocity calculated using Equation 8, which uses the entire cross-sectional area of the core as an input to calculate interstitial velocity. This localized source of acid also limits the possible locations, or cross-sectional area of the core, available for wormhole initiation.
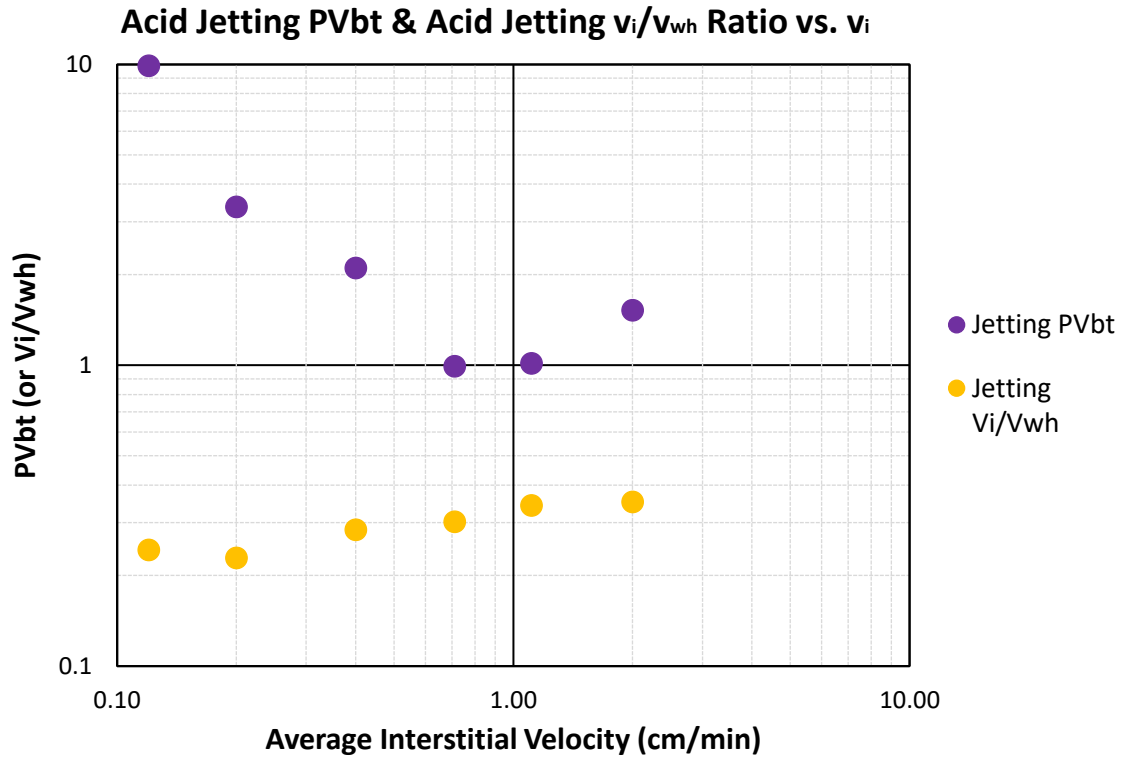
Figure 22 – Contrast of PVbt & v_i/v_{wh} Ratio in Acid Jetting Experiments

The potential discrepancy between local v_i and average v_i in acid jetting experiments must be considered. A field-scale modeler of acid jetting wormhole growth may not have time or be interested in the complex numerical simulations needed to calculate the localized v_i experienced by wormholes propagating from an acid jet. In fact, it may be more convenient for a field-scale modeler of acid jetting to have an acid jetting v_{wh} approximation as a function of the v_i of adjacent formation where matrix acidizing is occurring. The experimental apparatus and procedure used in this study allows the measurement of the v_i/v_{wh} ratio and v_{wh} behavior as a function of what would be a representative v_i in formation adjacent to an acid jet undergoing matrix acidizing.

53

As previously stated, PV_{bt} is equivalent to v_i/v_{wh} in matrix acidizing experiments. The v_i/v_{wh} ratio for acid jetting experiments is not equivalent to PV_{bt} so it can be plotted to obtain a comparison to the shape of a matrix acidizing wormhole efficiency curve (Figure 23). Figure 23 shows that acid jetting has no apparent optimum interstitial velocity and optimum v_i/v ratio. The optimum interstitial velocity for matrix acidizing is 1.0 cm/min and the optimum v_i/v_{wh} ratio is 0.2. Interestingly, the v_i/v_{wh} values for acid jetting are lower than the PV_{bt} values of matrix acidizing below $v_i \sim 0.75$ cm/min. Above $v_i \sim 0.75$ cm/min the v_i/v_{wh} values for matrix acidizing are slightly higher. The curve generated by plotting v_i/v_{wh} vs. v_i for acid jetting could be interpreted to be an equivalent form of the matrix acidizing wormhole efficiency curve just shifted to the left where the optimum interstitial velocity is approaching 0 cm/min. This shift to the left would corroborate the postulation that wormholes in acid jetting experiments have a higher interstitial velocity than the apparent interstitial velocity calculated by Equation 8.
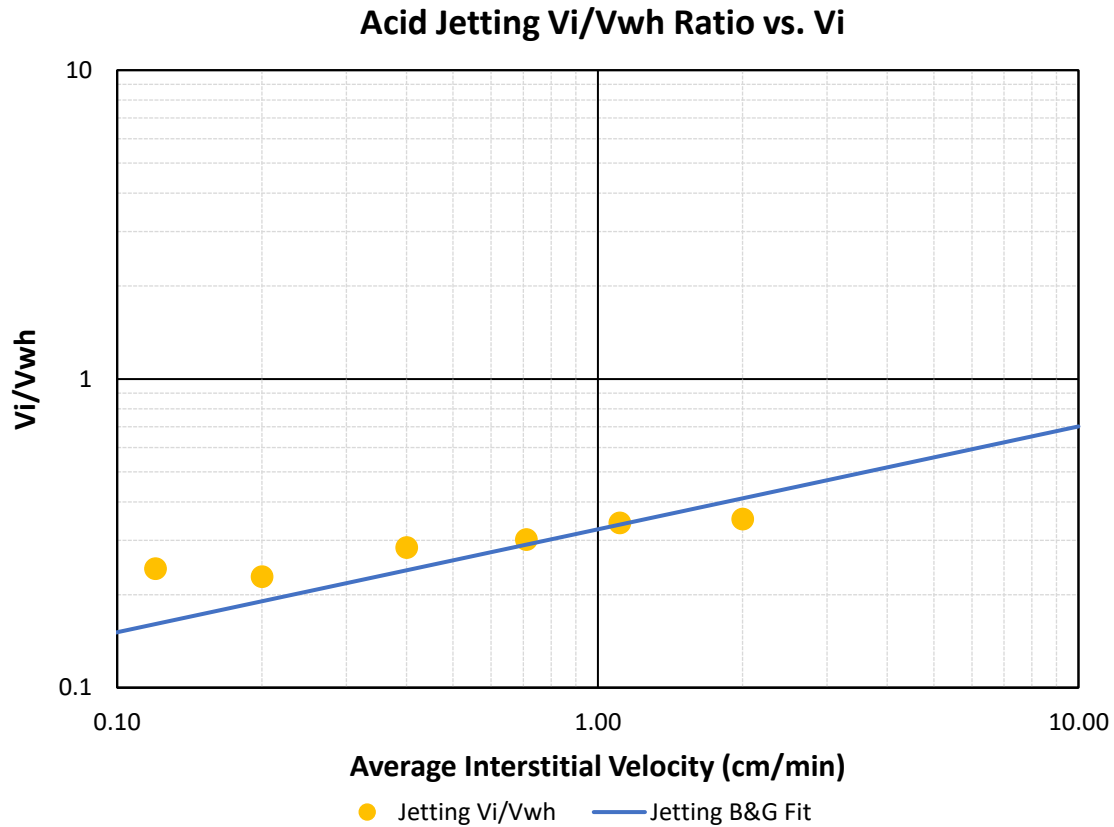
Figure 23 – Normalized Wormhole Growth Rate Plot for Acid Jetting Demonstrating Fluid-Loss Limited Wormhole Growth Behavior

A visual qualitative observation of the difference between the wormhole density of matrix acidizing experiments and acid jetting experiments could provide additional explanation for the behavior described above. At high interstitial velocities wormhole densities of both experiments are similar. At lower interstitial velocities, the matrix acidizing experiments feature a high density of thick wormholes, whereas the acid jetting experiments feature one or two highly branched wormholes initiated from the cavity (Figures 24 and 25). Figure 24 shows smaller cavity sizes from lower interstitial velocity to higher interstitial velocity (left to right); Figure 24 also shows increasing wormhole

complexity and branching from lower interstitial velocity to higher interstitial velocity (left to right). Figure 25 features CT images of three "non-jetting" experiments conducted utilizing an acid dispersing attachment which replaced the jetting nozzle in the acid jetting apparatus. The acid dispersing attachment was used to effectively conduct matrix acidizing experiments with the acid jetting experimental apparatus.
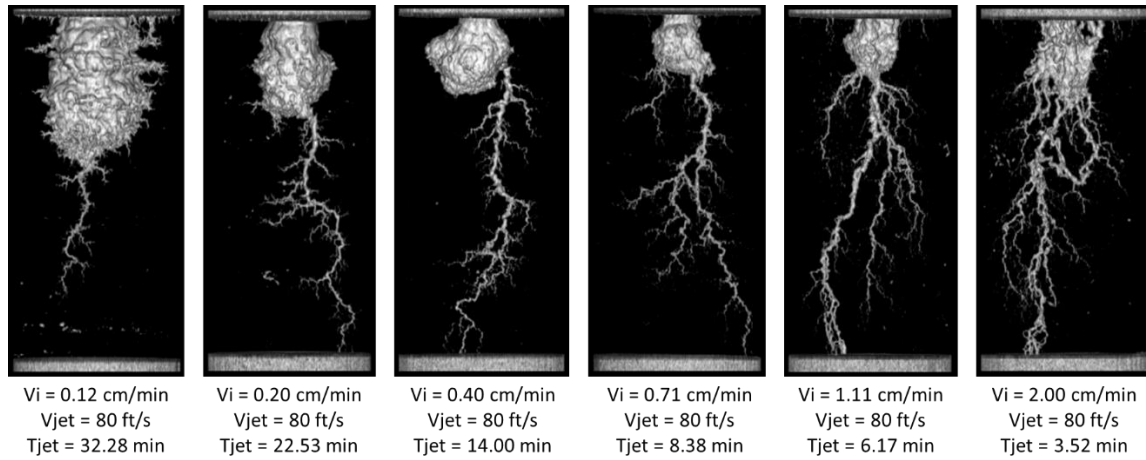

Vi = 0.12 cm/min
Vjet = 80 ft/s
Tjet = 32.28 min

Vi = 0.20 cm/min
Vjet = 80 ft/s
Tjet = 22.53 min

Vi = 0.40 cm/min
Vjet = 80 ft/s
Tjet = 14.00 min

Vi = 0.71 cm/min
Vjet = 80 ft/s
Tjet = 8.38 min

Vi = 1.11 cm/min
Vjet = 80 ft/s
Tjet = 6.17 min

Vi = 2.00 cm/min
Vjet = 80 ft/s
Tjet = 3.52 min

Figure 24 – CT Images of Acid Jetting Experiments (Interstitial Velocity and Wormhole Growth Rate Increasing from Left to Right)

The normalized wormhole growth rate curve corroborates previous discussion about higher localized interstitial velocity experienced by wormholes produced by acid jetting. The acid jetting v_i/v_{wh} points suggest an "optimum" interstitial velocity lower than the matrix acidizing data; optimum is put into quotes because v_i/v_{wh} is an arbitrary parameter that one would not seek to optimize. Essentially, Equation 8 becomes invalid because acid is not allowed to evenly flux through the entire cross-sectional area of the core. Instead, acid is forced to artificially leak off into the formation at the impingement point of the jet creating a cavity and shortly after a wormhole. Because the wormholes in

acid jetting are initiated and receive acid for growth from a smaller, localized jet impingement area, the wormholes have a higher interstitial velocity than what is calculated in Equation 8. The cross-sectional area for flow, A, in the denominator of Equation 8 is smaller than the total core cross-sectional area; therefore, v_i is larger than what is calculated using the total core cross-sectional area.
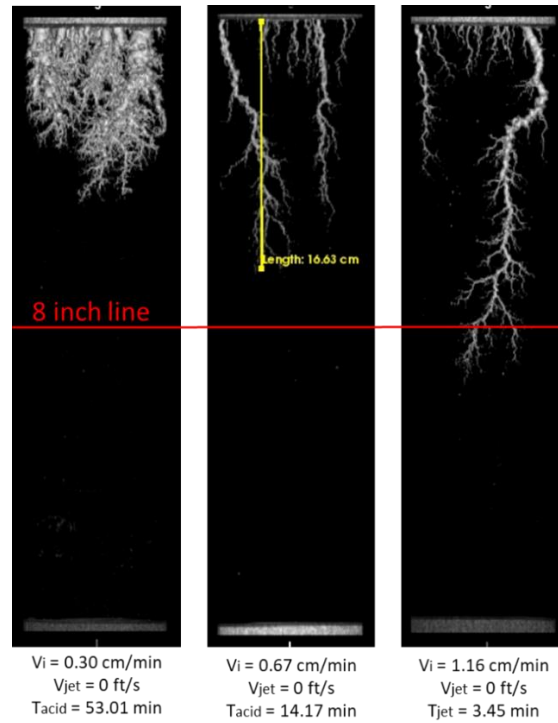

Figure 25 – Non-Jetting (Matrix Acidizing using Acid Jetting Apparatus) Experiments

3.2.3 v_{wh} Comparison

The third method of evaluation for acid jetting is obtained by simply plotting the wormhole velocity, v_{wh}, versus v_i for the set of experiments (Figure 26). An approximation of the optimum v_i/v_{wh} ratio and optimum v_i from the normalized wormhole growth rate curve are needed to generate the curve fit of the v_{wh} data.
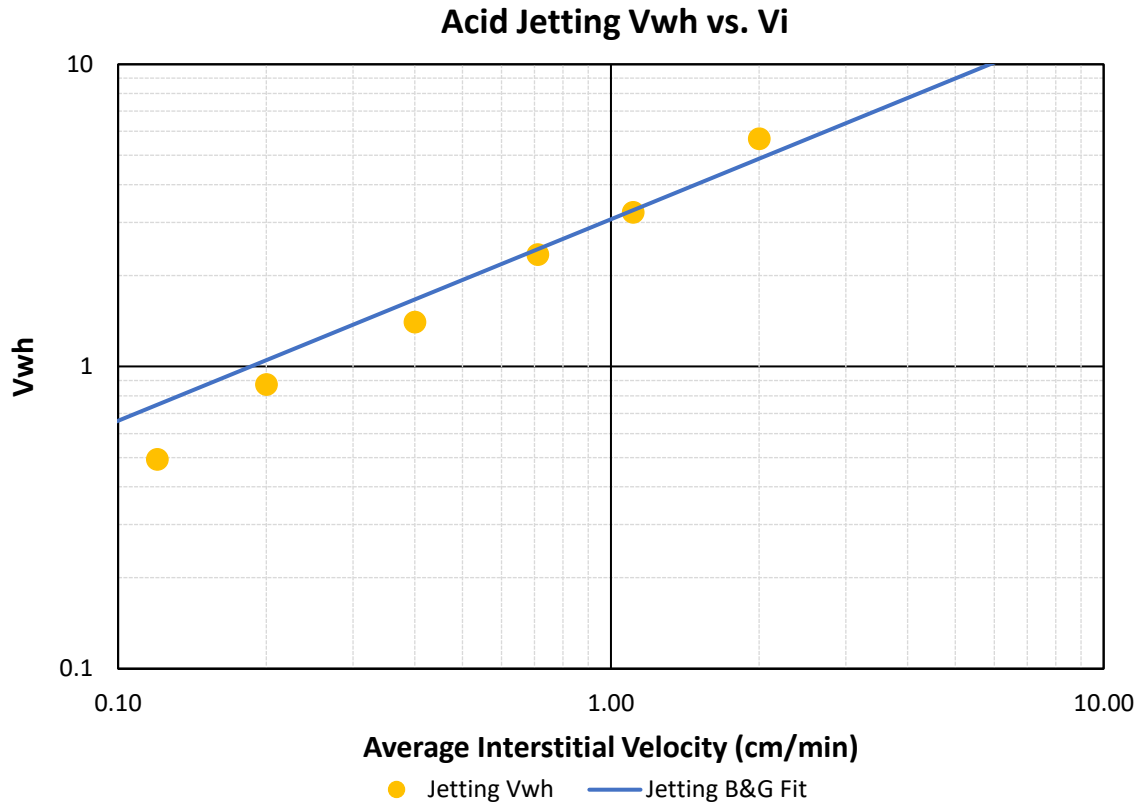
Figure 26 – Wormhole Growth Rate Plot for Acid Jetting Showing Linear Trend that Deviates from Typical Behavior of Matrix Acidizing Wormhole Growth Rate Plots

Figures 26 and 27 demonstrates that v_{wh} behavior for acid jetting and matrix acidizing is very comparable at $v_i > 0.75$ cm/min, although acid jetting v_{wh} is slightly lower. It shows much different v_{wh} for acid jetting versus matrix acidizing at $v_i < 0.75$ cm/min. All the acid jetting experiments seem to follow the approximate relationship of v_{wh} vs. v_i of matrix acidizing experiments above the optimum v_i condition. The $v_{wh} \sim v_i^{2/3}$ relationship established in the Buijse and Glasenbergen (2005) model above the optimum v_i condition is explained to be where fluid loss limited wormhole growth

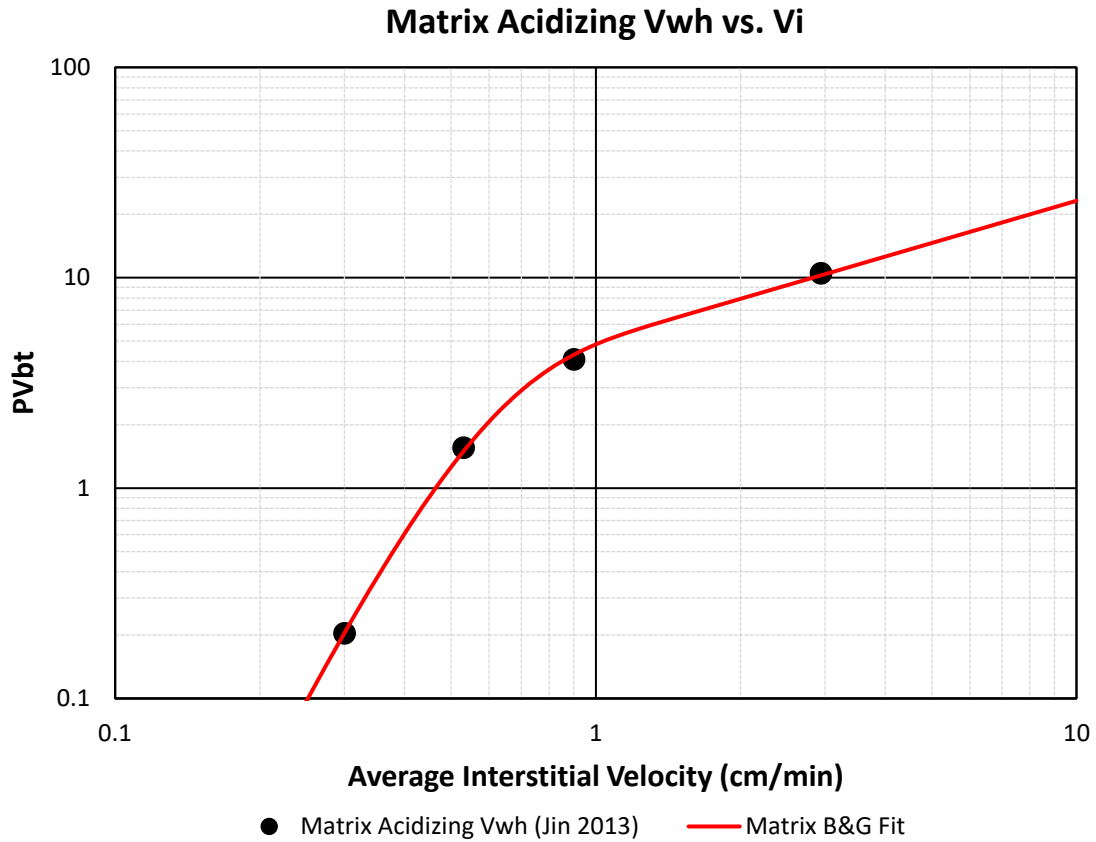dominates. The wormhole growth rate plot for the matrix acidizing experiments in Jin (2013) is shown in Figure 27.

Figure 27 - Wormhole Growth Rate Plot for Matrix Acidizing Experiments

3.2.4 Evaluation Limitations

The three graphical comparison methods outlined are limited by some assumptions. Also, these methods cannot be directly used for decision making in completion and stimulation design because a methodology to upscale the results to radial geometry has not been created. The assumptions in the evaluation methods are addressed here as well as the additional methodology needed for completion and stimulation design.

All the evaluation methods are limited by the assumption that the CT image processing methodology determines the bulk volume of rock dissolved and wormhole length due to acid jetting accurately. Although the bulk volumes and wormhole lengths determined in this study are believed to highly accurate, there is inevitable human interpretation involved in the CT image processing so there could be error introduced in the process, therefore it is acknowledged here.

Additionally, all the evaluation methods are limited by the inability to characterize the localized interstitial velocity in the wormhole during acid jetting. It is previously discussed how the wormholes in acid jetting potentially experience higher localized interstitial velocity than what is calculated using the entire cross-sectional area of the core. Nevertheless, this is an assumption in the evaluation methods and must be disclosed.

Computational fluid dynamics (CFD) simulations confirm the pressure spike from an impinging jet will be transmitted down long wormholes (Beckham, Shuchart, and Buechler 2015). It is assumed that the pressure drop along the length of the wormhole is negligible and that the pressure spike directly enhances wormhole growth rate. It is additionally noted that as cavity depth increases, the impingement pressure of the jet decreases; furthermore, Figure 24 demonstrates that the cavity depths in each experiment are not the same. This means each experiment experiences a different average jet impingement pressure. The time dependence of cavity depth growth, and therefore wormhole growth rate, at various interstitial velocity conditions must be incorporated into these evaluation methods. The incorporation of time dependence would allow a more

robust, universal evaluation of the differences in acid efficiency and wormhole growth rates between acid jetting and matrix acidizing experiments.

The normalized wormhole growth rate curve comparison method is limited by various factors. First, the assumption is made in calculating acid jetting time, t_{jet}, that the start time is indicated by when acid first reaches the nozzle and strikes the core face. Titration analysis of HCl concentration from the outlet line of the core holder during acid jetting experiments indicates that the bulk volume of fluid in the headspace of the core holder is not the full 15% HCl until a time period after acid first reaches the nozzle. It is assumed this has a negligible impact on experimental results since the nozzle continuously supplies fresh acid to the impingement point on the inlet core face.

3.4 The Case for Longer Wormholes Near an Acid Jet at the Field Scale: Near Wellbore and Far Field Behavior in Low Velocity, Diffusion-Limited Environments

The experimental data in this study provides evidence that an acid jet induces fluid loss limited wormhole growth across a range of apparent interstitial velocity conditions, even interstitial velocity conditions that appear to in the diffusion-limited wormhole growth regime for matrix acidizing experiments with similar conditions. Field acid treatment designs for limited entry liner completions can have injection rates that are expected to be in the diffusion-limited wormhole growth regime below the optimum, or critical, interstitial velocity condition (Jackson et al. 2012, Sau et al. 2014). An example of an acid treatment design for a limited entry liner where the injection flux is below the "critical injection flux" for the duration of the job (Figure 28). Additionally, the design and predicted stimulation results for an approximately 40+ gallon/ft job with a limited

entry liner are shown (Figure 29). Wormhole lengths below 1 ft potentially suggest diffusion-limited wormhole growth.
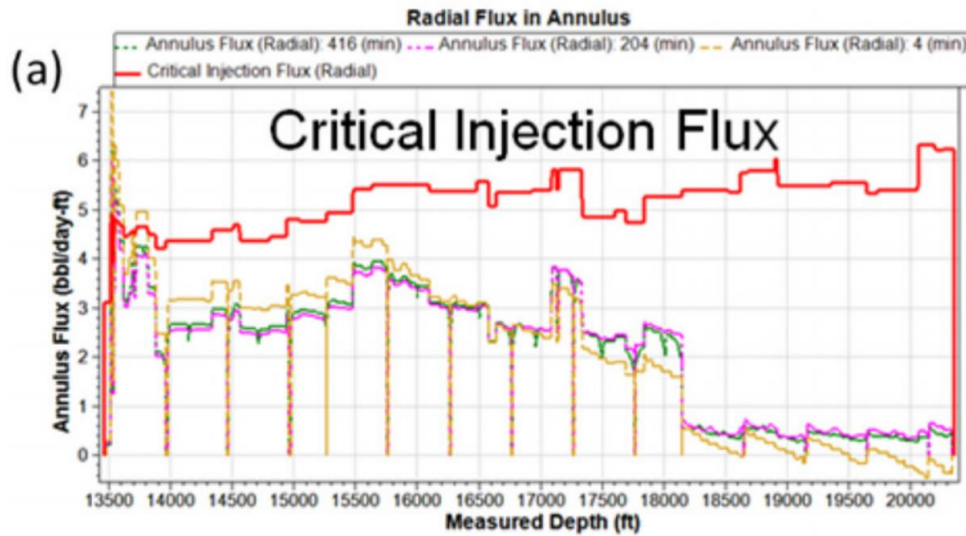

Figure 28 - Limited Entry Liner Acid Treatment Design Showing Injection Rates Below the Optimum Rate for a Majority of the Treatment (Reprinted from Sau et al. (2014))
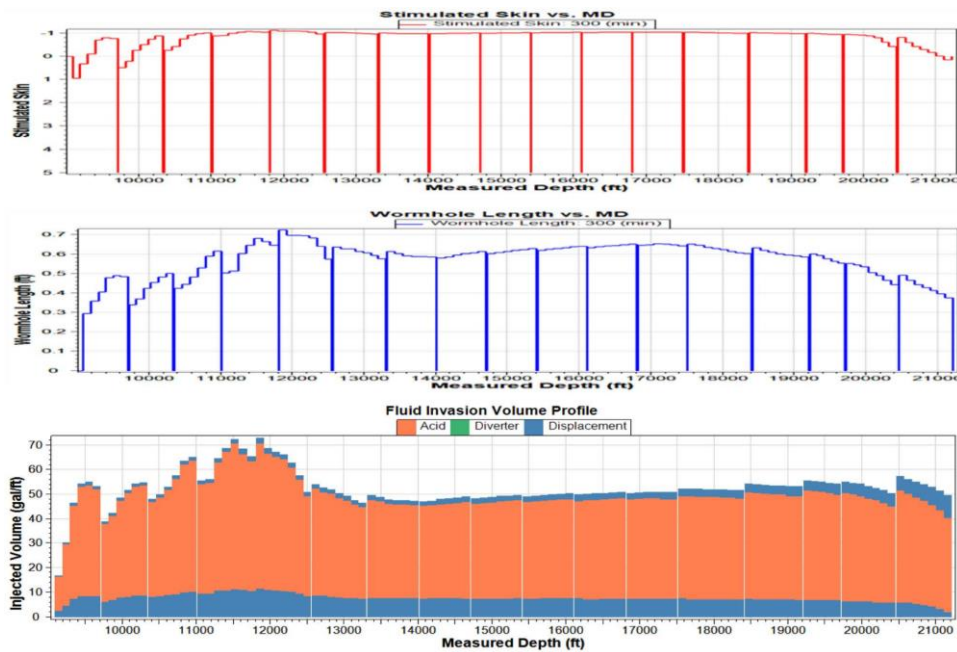

Figure 29 - Limited Entry Liner Acid Treatment Design with Predicted Wormholes Lengths Less than 1 ft (Reprinted from Jackson et al. (2012))

The cores used in this study are only 8-inch long; therefore, it is certainly possible that the fluid loss limited wormhole growth phenomena occurring in these experiments may only be a "near jet" phenomena. As discussed earlier, the fluid loss-limited wormhole growth may be in part caused by the impingement pressure of the jet. As cavity depth increases with increasing jetting time, the impingement pressure of the jet decreases, which could decrease the jets ability to produce wormhole growth in the fluid loss limited regime (Beckham, Shuchart, and Buechler 2015). This diminishing jet impingement pressure with cavity growth provides evidence for the argument that "enhanced" wormhole growth only occurs as a near wellbore effect in field scale acid treatments.

On the contrary, from an acid placement point of view, the simulation results presented in Furui et al. (2010) may provide theoretical evidence that wormhole growth proceeding from an acid jet can be sustained in the fluid loss-limited regime far from the wellbore. The model, shown in Figure 30, is a 3D FEM model with an open-hole well in a homogenous and isotropic permeability formation with radially growing, symmetrical wormholes. Wormholes are spaced at 60^0 in the angular direction, and there are wormholes of 0.5 ft, 1 ft, 2 ft, 4 ft, and 8 ft placed along the axial direction. Wormholes are considered to have 0.2 ft effective diameter. Figure 30 details further the conditions used to run the simulation.

Wellbore radius = 0.354 ft
Injection rate = 60 bpm per 1000 ft length
Injection pressure = 7000 psia at formation face
Formation permeability = 2 md
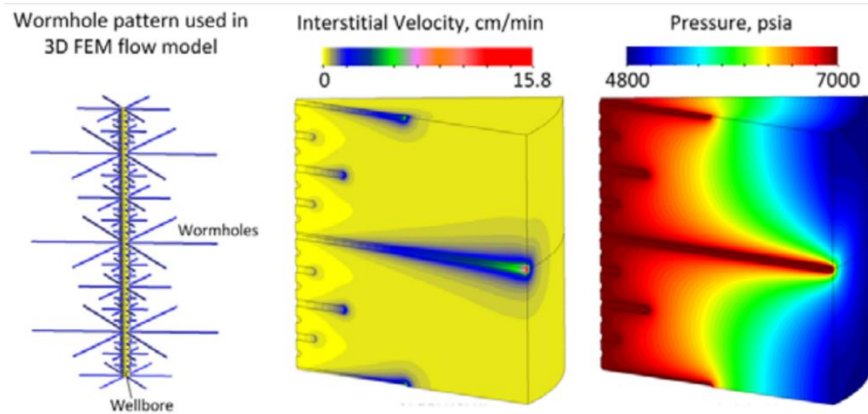Formation porosity = 35%
Fluid viscosity = 0.5 cp

Figure 30 - FEM Modeling of Fluid Loss and Competition for Injection Fluid in Radial Geometry Showing Longer Wormholes Have Increased Ability to Compete for Injection Fluid (Reprinted from Furui et al. (2010))

The simulation's interstitial velocity plot clearly shows the highest flow at the tips of the longest wormholes. The interstitial velocity is much lower in the short wormholes near the wellbore. This phenomenon is shown in more detail in Figure 31. The model calculates steady-state pressure and flux distributions based on an assumed distribution of wormholes and does not incorporate an acid-carbonate chemical reaction. If the assumption is valid that the wormholes at an acid jet are longer than the adjacent formation due to the near wellbore and early time impingement pressure of the jet, it is also a valid assumption, based on the observations presented in Furui et al. (2010), that the wormholes at an acid jet will be able to maintain higher flux conditions in the fluid loss-limited wormhole growth regime based on their ability to compete for injected fluid. Effectively,

if wormholes propagating from an acid jet are able to propagate faster near the wellbore at early times in the acid treatment and become longer than wormholes in the adjacent formation undergoing matrix acidizing, they will increase their ability to compete for injected fluid. With increased interstitial velocities from better ability to accept injected fluid, wormholes at an acid jet will be able to grow faster and longer than just from the near wellbore, early time effect of the jet impingement pressure.
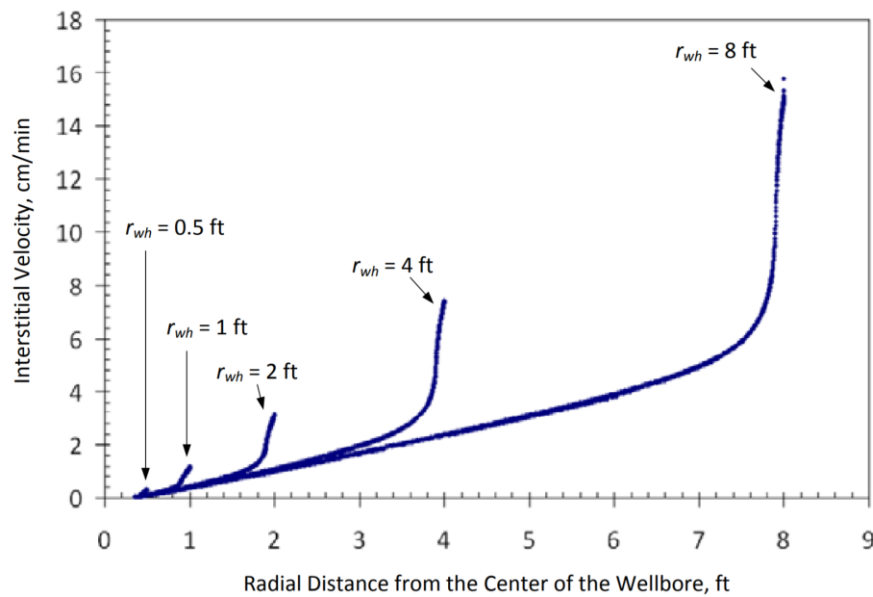

Figure 31 - Interstitial Velocity Profiles Plot Showing Longer Wormholes with Higher Interstitial Velocity Concentrated at the Wormhole Tip (Reprinted from Furui et al. (2010))

3.5 Field-Scale Acid Jetting Stimulation Outcome - A Theoretical Framework

Upscaling acid jetting laboratory experiment data for use in wellbore scale modeling of the acid jetting process in a limited entry liner is admittingly a difficult task. For one, the flow geometry changes from linear in a core flood experiment to radial in the open-hole annulus-reservoir interaction. The orientation of the jet in a horizontal well will

influence the jetting stimulation outcome due to directional velocity at the jet impingement point and directional permeability contrast in the vertical and horizontal directions. Large-scale, radial acid jetting experiments are likely necessary completely understand the acid jetting stimulation outcome in the wellbore scale; however, the laboratory experiments in this study clearly demonstrate that jetting can locally increase wormhole growth rate in matrix acidizing treatments at a range of low interstitial velocities. This "enhanced" wormhole growth rate comes at a cost: lost volumetric acid efficiency due to large cavity generation at the jet's point of impingement.

With the aforementioned in mind, matrix acidizing treatment design with a limited entry liner completion requires balancing the effect of enhanced wormhole growth rate near a jet with the effect of inefficient acid use at a cavity on the overall productivity of the well. The goal of this portion of the study is not to quantify wormhole length/geometry or cavity volume at the wellbore scale using the laboratory experimental results. That challenge will be left to those who pursue numerical modeling of acid jetting or those who pursue large-scale, radial acid jetting experiments. The goal of this portion of the study is to provide a theoretical framework for evaluating overall well productivity when assuming various acid jetting stimulation outcomes at the wellbore scale.

In an effort to simplify the visualization and quantification of the stimulation outcome in a limited entry liner completion featuring acid jetting, a theoretical stimulation geometry is proposed (Figure 32). Figure 32 depicts a horizontal wellbore with an open-hole limited entry liner completion where there is a matrix stimulation region, jetting "enhanced" stimulation region, orifices termed $perf_i$, spaced axially at a distance x_{perf},

66

horizontal formation permeability, k_H, and vertical formation permeability, k_V. The orifices will have a diameter, d_{perf}, and flowrate, q_{perf}, which determines the velocity and pressure impingement associated with the orifices. All these parameters affect wormhole growth and cavity growth near the orifices. The matrix stimulation region is characterized by a wormhole radius, r_{wh}; the jetting stimulation region is characterized by a wormhole radius, $r_{wh,jet}$, and a cavity volume, V_{cavity}. It is emphasized that Figure 32 does not mean to represent the difference in wormhole radii in the jetting and matrix regions to scale. The contrast in the figure is used to show the theoretical framework postulates longer wormholes in the region of the jet. Also, the parameter $r_{wh,jet}$, wormhole radius in the jetting region, implicitly suggests radial wormhole growth in the jetting region. This is not meant to be suggested; however, the assumption is that the stimulation outcome near a jet can be approximated using a skin model that assumes a radial or elliptical distribution of wormholes.
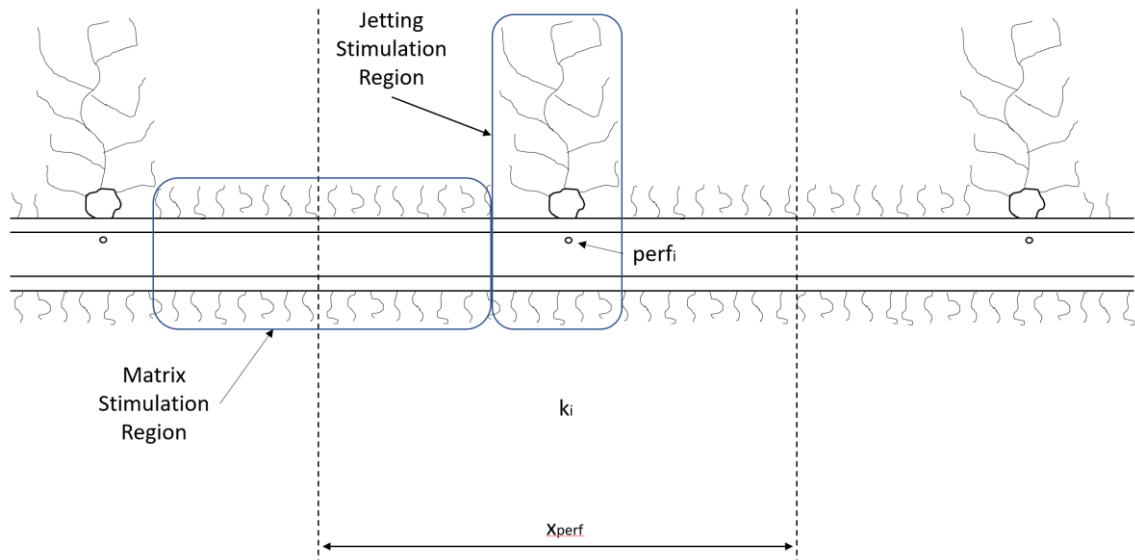

Figure 32 – Theoretical Stimulation Outcome for Limited Entry Liner Completion

67

The Furui, Zhu, and Hill (2003) formation damage skin factor and reservoir inflow model for horizontal wells provide a methodology to quantify the impact of non-uniform, ellipse-shaped formation damage along a horizontal well. The model first provides a method to calculate a local skin factor along each axial position in the well:

$$s(x) = \left[\frac{k}{k_D(x)} - 1\right] \ln\left[\frac{1}{I_{ani} + 1}\left(\frac{r_{dH}(x)}{r_w} + \sqrt{\left(\frac{r_{dH}(x)}{r_w}\right)^2 + I_{ani}^2 + 1}\right)\right] \quad (19)$$

where k is the undamaged permeability, k_D is permeability in the damaged zone, r_{dH} is the half-length of the horizontal axis of the damage ellipse, r_w is the wellbore radius, and I_{ani} is the anisotropic ratio of permeability, which equals $\sqrt{k_H/k_V}$. To reiterate, the damage zone is considered to be elliptical shape. The cumulative effect of the distribution of localized skin, $s(x)$, along the wellbore is provided in the model via the equation for the overall "equivalent" skin factor, s_{eq}:

$$s_{eq} = \frac{L}{\int_0^L \left\{ln\left[\frac{I_{ani}h}{r_w(I_{ani} + 1)}\right] + s(x)\right\}^{-1} dx} - \ln\left[\frac{I_{ani}h}{r_w(I_{ani} + 1)}\right] \quad (20)$$

where L is the length of the wellbore and h is the reservoir thickness. If the wellbore is discretized into equal size sections, Δx, with associated local skin factors, $s(x)$, the integral in Equation 20 can be transformed into a simpler summation which provides an estimate of s_{eq}:

$$s_{eq}$$

$$= \frac{L}{\Delta x \left[\left\{ ln \left[\frac{I_{ani}h}{r_w(I_{ani}+1)} \right] + s(x_1) \right\}^{-1} + \left\{ ln \left[\frac{I_{ani}h}{r_w(I_{ani}+1)} \right] + s(x_2) \right\}^{-1} \cdots \right]} - ln \left[\frac{I_{ani}h}{r_w(I_{ani}+1)} \right] \quad \textbf{(21)}$$

The original purpose of the model was to consider non-uniform, ellipse-shaped formation damage along the axial direction of the well; however, the model can be used to evaluate non-uniform, ellipse-shaped (and radial-shaped) stimulation results in a horizontal wellbore as well (Schwalbert, Zhu, and Hill 2018). First, a local wormhole radius, $r_{wh,eq}$, is predicted using a global wormhole model such as Buijse and Glasenbergen (2005) or Furui et al. (2010). If wormholes are believed to have a radial geometry around the wellbore (most likely in isotropic formations), the local skin factor is predicted with Hawkins (1956) model:

$$s(x) = -ln \left(\frac{r_{wh,eq}}{r_w} \right) \quad \textbf{(22)}$$

where s is skin factor, $r_{wh,eq}$ is wormhole radius predicted by a global wormhole model, and r_w is wellbore radius. However, if the wormholes are thought to have an elliptical geometry, the local skin factor is predicted by first calculating the horizontal wormhole length, r_{whH}, with Equation 23:

$$r_{whH} = r_{wh,eq} \sqrt{I_{ani,wh}} \quad \textbf{(23)}$$

where $I_{ani,wh}$ is the wormhole anisotropy ratio, or r_{whH}/r_{whV}, which is not to be confused with the permeability anisotropy ratio, I_{ani}. Schwalbert, Zhu, and Hill (2018) suggest, based on simulation results, that a reasonable estimate of $I_{ani,wh}$ is I_{ani}. Therefore, in this

study $I_{ani,wh}$ is considered equivalent to I_{ani}. Finally, the local skin of an elliptical-shaped wormhole region can be estimated via Equation 24, which is alternate take on Equation 19 developed by Furui, Zhu, and Hill (2003).

$$s(x) = -\ln\left[\frac{1}{I_{ani}+1}\left(\frac{r_{whH}}{r_w} + \sqrt{\left(\frac{r_{whH}}{r_w}\right)^2 + I_{ani}^2 - 1}\right)\right] \qquad (24)$$

To evaluate the overall net effect on well productivity of stimulation near orifices in a limited entry liner completion, the previously developed equations by Furui, Zhu, and Hill (2003) and Schwalbert, Zhu, and Hill (2018) can be used in the context of the conceptual framework provided in Figure 32 with the following workflow:

1) Assume a $r_{wh,eq}$ for the jetting stimulation region and matrix stimulation region

2) Calculate r_{whH} for the jetting stimulation region and matrix stimulation region using Equation 23

3) Calculate the local skin factor for the jetting stimulation region, s_{jet}, and the matrix stimulation region, s_{matrix}, using Equation 24

4) Assume a wellbore length, L, wellbore radius, r_w, number of orifices, N_{perf}, and the wellbore length associated with each jetting stimulation region, Δx_{jet}, to calculate s_{eq} with Equation 25 (a more specific version of Equation 21 for the stimulation outcome depicted in Figure 32)

$$s_{eq} = \frac{L}{N_{perf}\Delta x_{jet}\left[\ln\left[\frac{I_{ani}h}{r_w(I_{ani}+1)}\right]+s_{jet}\right]^{-1} + \left(L-N_{perf}\Delta x_{jet}\right)\left[\ln\left[\frac{I_{ani}h}{r_w(I_{ani}+1)}\right]+s_{matrix}\right]^{-1}} - \ln\left[\frac{I_{ani}h}{r_w(I_{ani}+1)}\right] \qquad (25)$$

5) Assume a reservoir thickness, h, and the drainage length perpendicular to the well, y_b, and calculate the dimensionless productivity index using Equations 26, 27, and 28 (Furui, Zhu, and Hill 2003)

$$\frac{J_s}{J_0} = \frac{\beta_r + \beta_l - 1.224 + s_o}{\beta_r + \beta_l - 1.224 + s_{eq}} \tag{26}$$

$$\beta_r = \ln\left[\frac{hI_{ani}}{r_w(I_{ani} + 1)}\right] \tag{27}$$

$$\beta_l = \frac{\pi y_b}{hI_{ani}} \tag{28}$$

The s_{eq} in Equation 26 is calculated by Equation 25. The methodology proposed above provides the opportunity to evaluate the performance of many different potential stimulation geometries in a well completed with a limited entry liner completion. Before continuing into case studies with the proposed methodology, some assumptions involved in deriving the equations used must be understood.

First, it must be understood a stimulation geometry is simply being imposed or assumed. The workflow is providing the methodology to evaluate well performance based on the geometry imposed, not the methodology to predict the geometry itself. Many uncertainties remain about the wormhole lengths and the geometry of jetting stimulation in the wellbore scale. Additionally, orifice spacing is the same length across the entire length of the wellbore, and the stimulation associated with each orifice is consider equivalent. The results in this study provide evidence that acid jetting produces longer wormholes in certain environments, therefore, this methodology postulates an enhanced

wormhole region near acid jetting in the wellbore scale but not the specific scale or geometry.

Second, the assumptions going into the skin factor equations must be understood. A critical underlying assumption in the skin factor in Equation 24 is that $I_{ani,wh}$ is equivalent to I_{ani}; this is based on evidence from simulations (Schwalbert, Zhu, and Hill 2018). Another assumption is that the wormhole radius/length outside the wellbore can be approximated by infinite permeability. An assumption in the model, which is inherent to Equations 19 and 24, is that the cross-section of wellbore damage or stimulation perpendicular to the wellbore can be represented by the isobars in the Peaceman (1983) solution for fluid flow through an anisotropic permeability field to a cylindric wellbore (Furui, Zhu, and Hill 2003). Additionally, the overall skin factor, s_{eq}, in Equation 20 is derived assuming a fully penetrating wellbore, therefore any partial penetration skin is neglected in the skin factor.

Third, the assumptions associated with the Furui, Zhu, and Hill (2003) reservoir inflow model for a horizontal well must be documented. As mentioned with the overall skin factor above, the inflow model assumes a fully penetrating horizontal well in a rectangular reservoir. The model additionally assumes steady-state flow of an incompressible fluid into the horizontal wellbore. The model assumes the total pressure drop in the formation is the sum of the linear pressure drop regime far from the wellbore and the radial/elliptical pressure drop regime near the wellbore.

3.6 Field-Scale Acid Jetting Stimulation Outcome – Case Study

The equations and methodology in the previous section are used to perform a case study. The case study tests various acid jetting stimulation geometries (x_{perf}, Δx_{jet}, N_{perf}), reservoir properties (y_b, h, I_{ani}), and initial formation damage conditions (s_d) to plot s_{eq} and J_s/J_0 (or J_s/J_d) versus the acid jetting isotropic wormhole length, $r_{wh,eq}$, to provide a reference for how these stimulation characteristics affect overall well productivity. A 10,000 ft wellbore is considered; an 8½-inch diameter wellbore is considered. The matrix stimulation region is considered to have $s_{matrix} = 0$ post-stimulation, except in Case 6, where $s_{matrix} = 10$.

In order to more clearly demonstrate the calculations going in the plots in the plots below, a sample calculation is performed below:

1. Assume $r_{wh,jet} = 10\ ft$ and $r_{wh,matrix} = r_w$ ($S_{matrix} = 0$)

2. Calculate $r_{whH,jet}$ assuming $I_{ani} = I_{ani.wh} = 10$

$$r_{whH,jet} = 10ft * \sqrt{10} = 31.62\ ft$$

3. Calculate s_{jet} assuming $r_w = 0.35\ ft$

$$s_{jet} = -\ln\left[\left(\frac{1}{10+1}\right)\left(\frac{31.62}{0.35} + \sqrt{\left(\frac{31.62}{0.35}\right)^2 + 10 - 1}\right)\right] = -2.80$$

4. Calculate s_{eq} assuming $L = 10,000\ ft$, $N_{perf} = 249$, $\Delta x_{jet} = 5\ ft$, and $h = 100ft$

$$s_{eq} = \frac{10000ft}{(249*5ft)\left[ln\left[\frac{10*100}{0.35(10+1)}\right] - 2.80\right]^{-1} + (10000 - (249*5ft))\left[ln\left[\frac{10*100}{0.35(10+1)}\right] - 0\right]^{-1}} - \ln\left[\frac{10*100}{0.35(10+1)}\right]$$

$$s_{eq} = -0.62$$

73

5. Calculate the J_s/J_0 assuming $y_b = 500\ ft$ and $S_0 = 0$

$$\beta_r = \ln\left[\frac{100ft * 10}{0.35ft * (10 + 1)}\right] = 5.56$$

$$\beta_l = \frac{\pi * 500ft}{100ft * 10} = 1.57$$

$$\frac{J_s}{J_0} = \frac{5.56 + 1.57 - 1.224 + 0}{5.56 + 1.57 - 1.224 - 0.62} = \frac{5.91}{5.29} = 1.12$$

This calculation can be verified against the graph in Case 4. In the $I_{ani} = 10$ lines, which

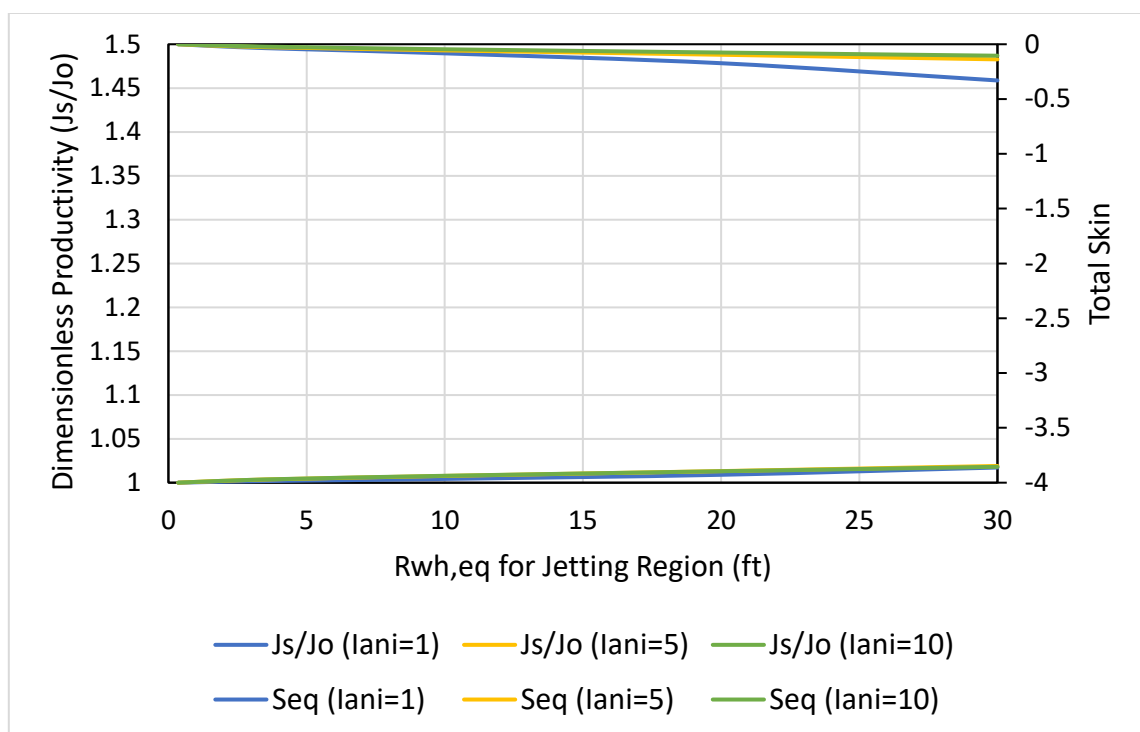are green on the graph, at $r_{wh,eq} = 10\ ft$, $S_{eq} = -0.62$ and $J_s/J_0 = 1.12$.

Figure 33 – Case 1 (h=100 ft, x_perf=120 ft, Δx_jet=1 ft, N_perf=82, So=0)
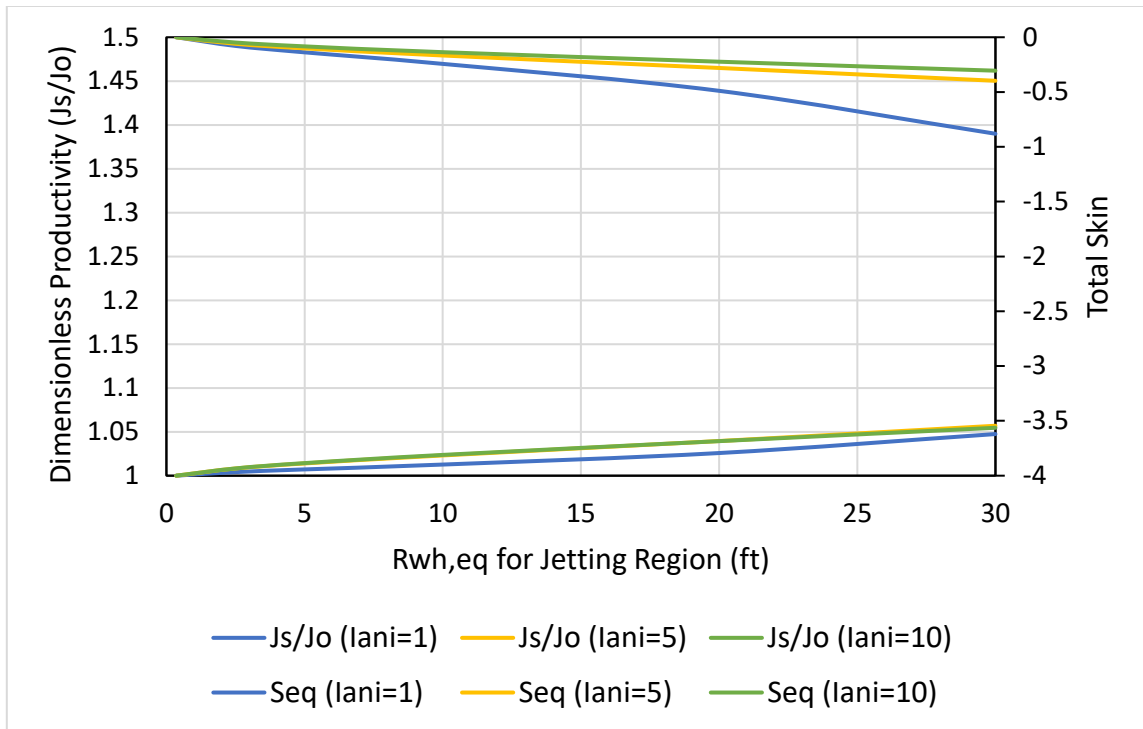
Figure 34 – Case 2 (h=100 ft, x_perf=40 ft, Δx_jet=1 ft, N_perf=249, So=0)
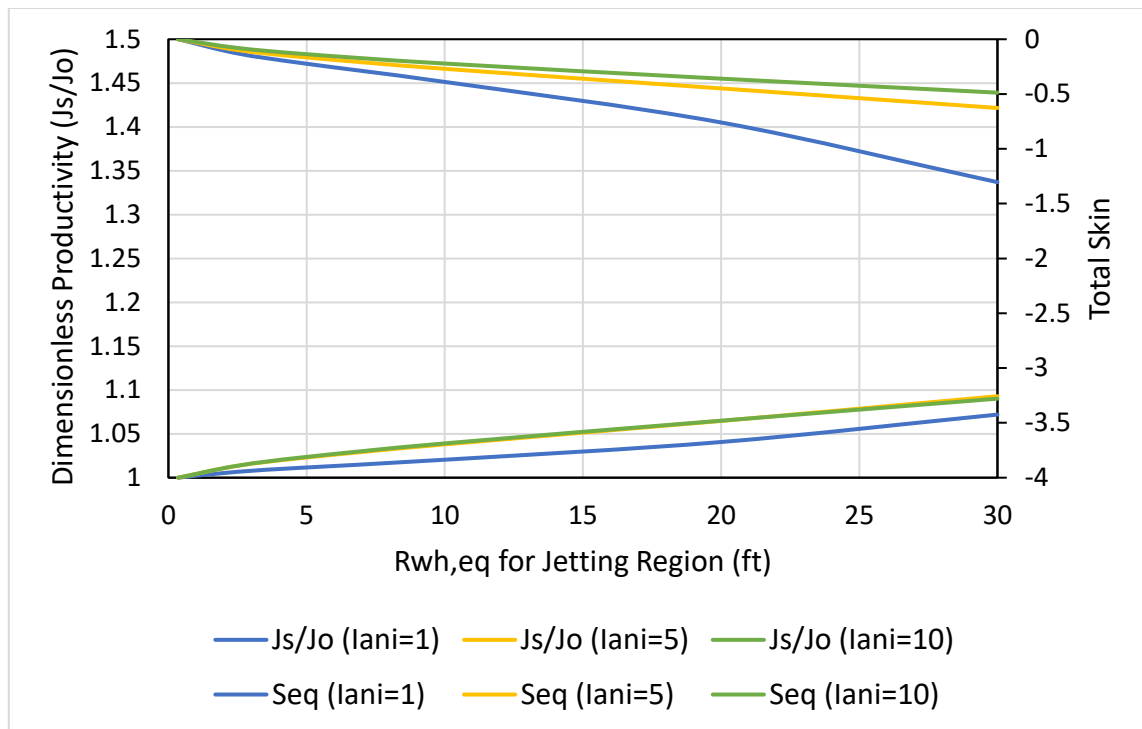
Figure 35 – Case 3 (h=100 ft, x_perf=120 ft, Δx_jet=5 ft, N_perf=82, So=0)
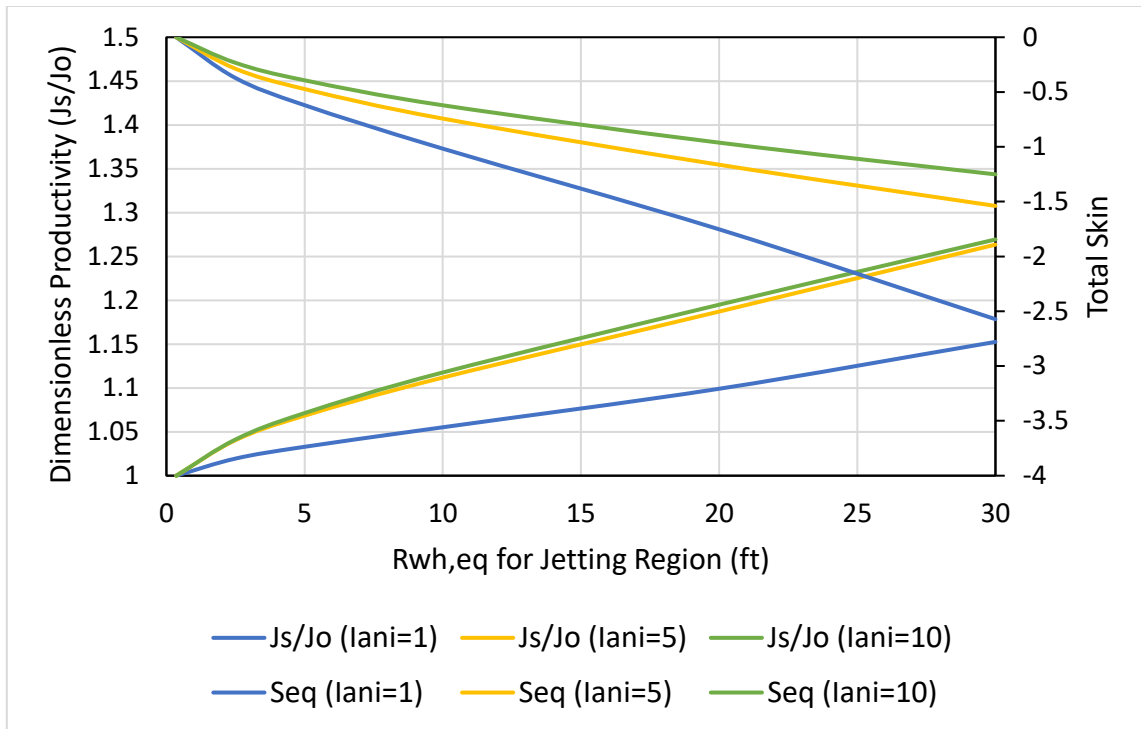
Figure 36 – Case 4 (h=100 ft, x_perf=40 ft, Δx_jet=5 ft, N_perf=249, So=0)
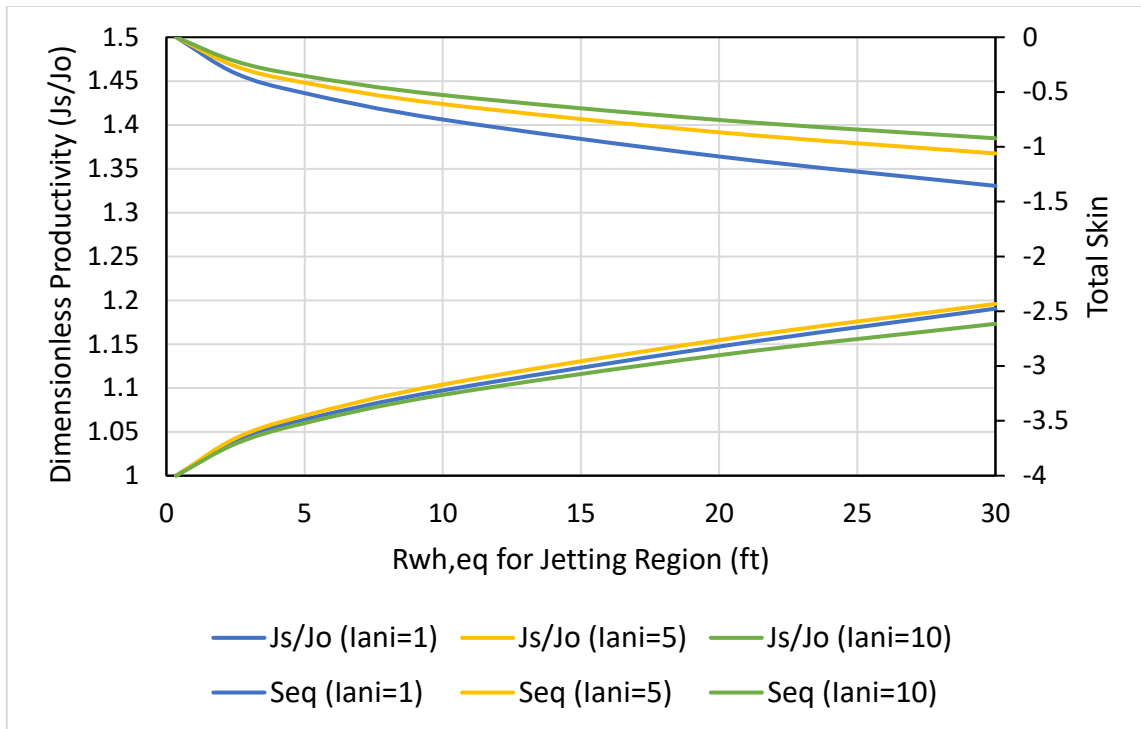
Figure 37 – Case 5 (h=500 ft, x_perf=40 ft, Δx_jet=5 ft, N_perf=249, So=0)
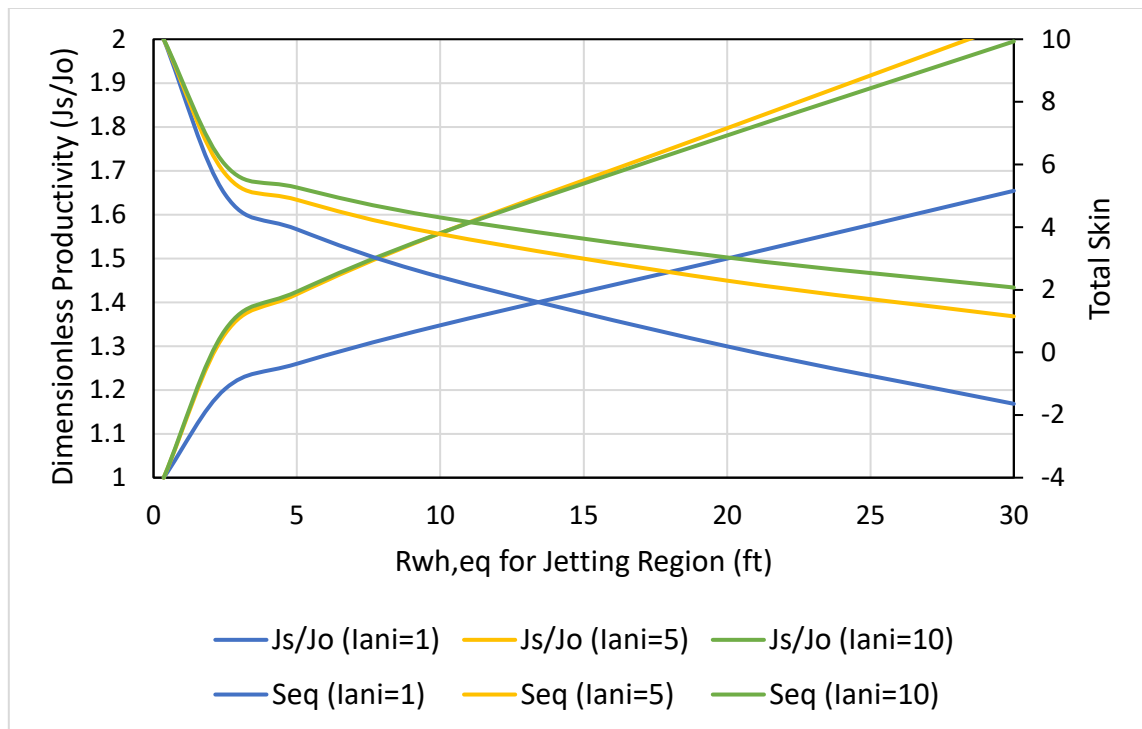
Figure 38 - Case 6 (h=100 ft, x_perf=40 ft, Δx_jet=5 ft, N_perf=249, So=10, Smatrix=10)
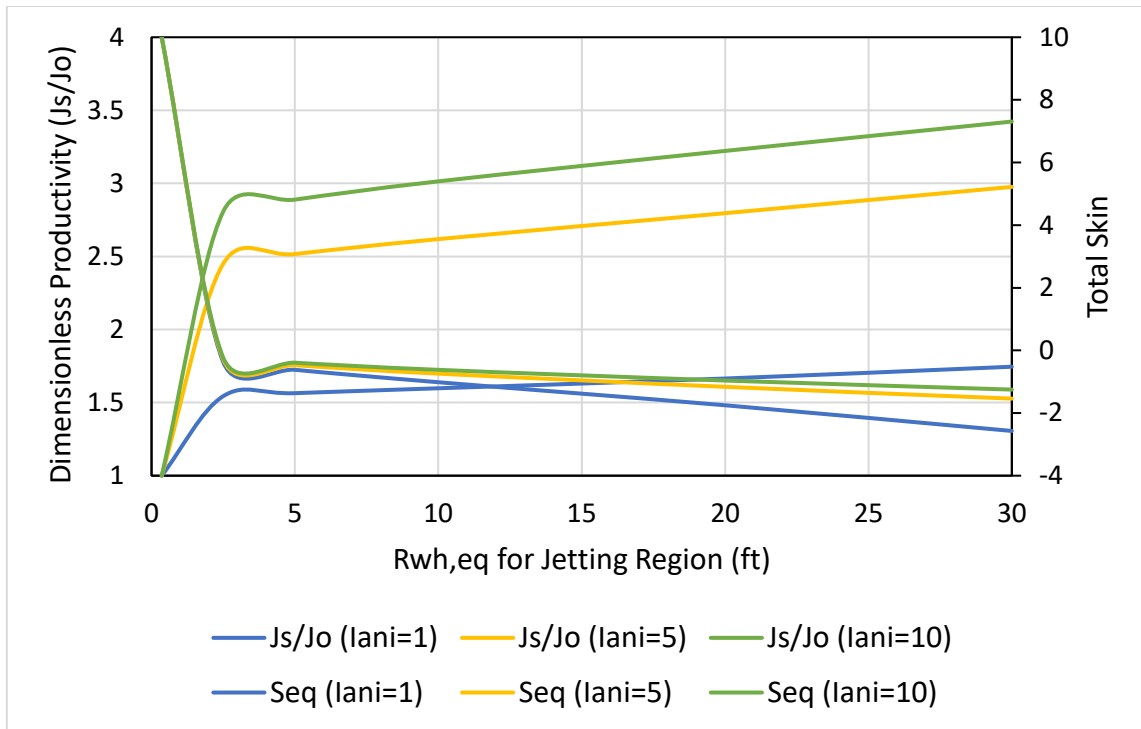
Figure 39 - Case 7 (h=100 ft, x_perf=40 ft, Δx_jet=5 ft, N_perf=249, So=10, Smatrix=0)

The case study provides valuable insights into the stimulation outcome for a limited entry liner, and it provides some obvious conclusions. A simple conclusion of this case study is that while a carbonate matrix acidizing treatment with a limited entry liner may substantially improve well productivity, impact the jetting stimulation alone depends on $r_{wh,eq}$, h, I_{ani}, and previous formation damage. The improvement in well productivity is also dependent on the number of orifices, N_{perf}, and the length of the wellbore allocated to each jetting stimulation region, L_{perf}. For the cases where $h = 100$ ft, reservoirs with higher permeability anisotropy show less skin reduction but higher productivity increases due jetting stimulation. The dependence of skin factor reduction and well productivity increase on $r_{wh,eq}$, N_{perf}, and L_{perf} in this model demonstrate the need to run larger-scale, radial-geometry acid jetting experiments which calibrate the smaller-scale linear core floods presented in this study.

The thicker reservoir used in Case 5 demonstrates alternative behavior with changing permeability anisotropy due to increased radial/elliptical flow influence in the inflow model, where $I_{ani} = 5$ saw the highest productivity increase. Case 6 demonstrated that in a previously damaged well, where $S_0 = 10$ and $S_{matrix} = 10$ after stimulation, the high probability stimulation near a jet provides a risk management tool to an engineer designing a limited entry liner completion/stimulation to ensure increased productivity. However, Case 7 clearly shows the importance of the matrix stimulation. In this case, $S_0 = 10$ but $S_{matrix} = 0$. Depending on the permeability anisotropy, the reduction in skin throughout the entire wellbore in this case can increase productivity three times ($I_{ani} =$

10), where longer wormholes in the jetting stimulation region have a lesser impact. This reinforces the importance of the cavity in the acid jetting process.

When acid is used in generating a cavity when an acid jet strikes the borehole wall, it contributes to the enhanced wormhole growth near the jet; however, it reduces the acid concentration available to the adjacent wellbore undergoing matrix acidizing. With this in mind, it is critically important to weigh the enhanced productivity from longer wormholes near a jet with the "opportunity cost" of potentially lost matrix acidizing stimulation in the adjacent wellbore. A potential methodology to consider this opportunity cost is to construct a cavity volume growth rate model (cavity volume growth rate versus time), calculate the acid concentration lost in a finite time step based on the cavity growth rate model, calculate wormhole growth rate based on the lower acid concentration available to the adjacent formation undergoing matrix acidizing, and repeat the calculations for the total job time. The well productivity can be considered with and without the lost acid concentration from cavity generation. The cumulative sum of the quantitative increase in dimensionless productivity from enhance wormhole growth near a jet and the quantitative negative drop in dimensionless productivity from reduced stimulation in the adjacent matrix acidizing ultimately provides the net effect of acid jetting on the overall treatment performance.

Clearly, the axial length of wellbore associated with the jetting stimulation region, which is equivalent to $N_{perf}\Delta x_{jet}$, is extremely important to well productivity increases in these cases, as colored by the discussion above. An engineer designing a limited entry liner is primarily concerned with achieving the desired acid allocation along the wellbore,

therefore he or she may not increase orifice density to create more acid jetting if it compromises acid placement and allocation. Smaller diameter orifices in a limited entry liner allow for a higher density of orifices without compromising acid placement. Smaller orifices would result in less prolific jets, which most likely reduces the wormhole growth enhancement of the jet, but also reduces cavity growth produced by the jet. Based on the results from the inflow model used in this case study, it seems a higher density of moderate wormhole lengths increases well productivity more than a lower density of prolific wormholes lengths along the wellbore. As a matter of practicality, smaller diameter orifices may cause other issues to arise in the completion and production operations of a well. A high level of caution should be used if considering this approach.

4. CONCLUSIONS & RECOMMENDATIONS FOR FUTURE WORK

To facilitate the most efficient means of delivering the conclusions from this study and the recommendations for future work, numbered lists are provided.

4.1 Conclusions

1. An experimental apparatus and procedure were created that allowed approximately constant interstitial velocity acid jetting core flood experiments to be conducted.

2. The experimental apparatus and procedure integrated effluent flow measurement via a high precision scale, effluent flow control via a control valve-actuator, and a LabVIEW code which had a convenient user interface to monitor interstitial velocity real-time and make adjustments to the control valve with the actuator to enable interstitial velocity control in the acid jetting experiments.

3. Acid jetting is inherently inefficient on an acid volume basis; matrix acidizing experiments break through cores using less or equal volumes of acid at all interstitial velocity conditions using lower permeability Indiana limestone cores.

4. The literature shows that wells drilled with long laterals (10,000 ft or longer) in carbonate reservoirs completed and stimulated utilizing a limited entry liner are designed with flux rates below the optimum interstitial velocity conditions during field treatments (potentially practical operational constraints in the field).

5. Acid jetting experiments demonstrate wormhole growth rate behavior in the fluid loss-limited regime at lower interstitial velocities below the optimum, whereas

matrix acidizing experiments demonstrate wormhole growth rate in the diffusion-limited regime at interstitial velocities below the optimum.

6. The potential for enhanced wormhole growth rate from jetting at the orifices of a limited entry liner should be evaluated with reference to the lost acid concentration by generating a cavity at the acid jet impingement on the wellbore.

7. Utilizing and slightly modifying previous work on skin factor and reservoir inflow modeling for horizontal wells, a methodology was created to evaluate the overall skin factor reduction and dimensionless productivity increase of an assumed jetting stimulation size and geometry.

8. Given the assumptions inherent to the skin factor and reservoir inflow model and the acid jetting stimulation sizes and geometries considered in the case study, it seems the overall impact of acid jetting stimulation alone is highly dependent on reservoir properties and completion design.

9. Overall stimulation success using limited entry liners requires proper stimulation along the entire lateral; matrix acidizing occurring adjacent to and in between acid jetting contributes significantly to overall skin reduction and productivity increase.

10. Cavity growth and its negative affect on acid efficiency should be approached quantitatively to determine how much cavity growth reduces potential wormhole growth in matrix acidizing regions.

4.2 Recommendations for Future Work

1. Conduct large-scale, radial-geometry acid jetting experiments with a wellbore scale jet diameter.

2. Calibrate the smaller scale laboratory acid jetting experiment to the large-scale, radial-geometry acid jetting experiments.

3. Quantify the difference between near field (close to the wellbore) and far field (farther from the wellbore) effects on acid jetting stimulation.

4. Construct a wormhole growth model based on interstitial velocity, jet diameter, jet velocity, jet stand-off distance, rock permeability, rock porosity, and rock mineralogy.

5. Construct a cavity growth model and an acid concentration reduction model based on the same parameters mentioned in Recommendation 4.

6. Utilizing all the information in Recommendations 1-5, quantify the overall impact on well productivity of acid jetting, using the skin modeling methodology provided in this work.

REFERENCES

Beckham, R. E., C. E. Shuchart, S. R. Buechler. 2015. Impact of Acid Jetting on Carbonate Stimulation. Proc., International Petroleum Technology Conference, Doha, Qatar.

Belostrino, Emmanuel. 2016. Experimental Study of Multi-Stage Acid Jetting in Carbonate Rocks. Master of Science, Texas A&M University (December).

Buijse, M., G. Glasenbergen. 2005. A Semiempirical Model to Calculate Wormhole Growth in Carbonate Acidizing. Proc., SPE Annual Technical Conference and Exhibition, Dallas, Texas.

Buijse, Marten A. 1997. Understanding Wormholing Mechanisms Can Improve Acid Treatments in Carbonate Formations. Proc., SPE European Formation Damage Conference, The Hague, The Netherlands.

Economides, Michael J., A. Daniel Hill, Christine Ehlig-Economides et al. 2013. *Petroleum Production Systems*, Second edition, 499-534, Pearson Education, Inc. (Reprint).

Fredd, C. N., H. S. Fogler. 1999. Optimum Conditions for Wormhole Formation in Carbonate Porous Media: Influence of Transport and Reaction. *SPE Journal* Volume 4 (No. 3): 196-205.

Furui, K., R. C. Burton, D. W. Burkhead et al. 2010. A Comprehensive Model of High-Rate Matrix Acid Stimulation for Long Horizontal Wells in Carbonate Reservoirs. Proc., SPE Annual Technical Conference and Exhibition, Florence, Italy.

Furui, Kenji, D. Zhu, A. D. Hill. 2003. A Rigorous Formation Damage Skin Factor and Reservoir Inflow Model for a Horizontal Well. *SPE Production and Facilities*: 151-157.

Grabski, Elizabeth Rachel. 2012. Matrix Acidizing Core Flooding Apparatus: Equipment and Procedure Description. Master of Science, Texas A&M University, College Station, TX (December).

Hansen, J. H., N. Nederveen. 2002. Controlled Acid Jet (CAJ) Technique for Effective Single Operation Stimulation of 14,000+ ft Long Reservoir Sections. Proc., SPE 13th European Petroleum Conference, Aberdeen, Scotland.

Hawkins, Murray F. 1956. A Note on the Skin Effect. *Journal of Petroleum Technology*: 65-66.

Hill, John R. 2018. Indiana Limestone. Indiana Geological & Water Survey, https://igws.indiana.edu/MineralResources/Limestone.cfm (downloaded February 26 2018).

Holland, Christopher. 2014. Experimental High Velocity Acid Jetting in Limestone Carbonates. Master of Science, Texas A&M University (May).

Hosani, Fahad Al, Alaa Amin, Yasser Ali et al. 2016. Robust Completion and Stimulation Design Methodology to Maximize Well Performance for Long Horizontal Laterals in a Giant Off-Shore Field Development. Proc., Abu Dhabi International Petroleum Exhibition & Conference, Abu Dhabi, UAE.

Issa, Faiz, Jonathan Abbott, Aulia Akbari. 2014. Production Optimization of Maximum Reservoir Contact Well by Utilizing Acid Stimulation with Limited Entry Technique. Proc., Abu Dhabi International Petroleum Exhibition and Conference, Abu Dhabi, UAE.

Jackson, Alfred, Badr Musabbeh Al Azizi, Curtis Kofoed et al. 2012. Completion and Stimulation Methodology for Long Horizontal Wells in Lower Permeability Carbonate Reservoirs. Proc., Abu Dhabi International Petroleum Exhibition & Conference, Abu Dhabi, UAE.

Jin, Xiao. 2013. Experimental Investigation for the Effects of the Core Geometry on the Optimum Acid Flux in Carbonate Acidizing. Master of Science, Texas A&M University (December).

Mason, David, Owen Hey, Henk Kramer. 1997. Extended Reach Well Completion and Operational Considerations. Proc., Offshore Technology Conference, Houston, Texas.

Mayer, Christian S. J., Rajes Sau, Chris E. Shuchart. 2014. Open-Hole Fluid Displacement for Carbonate Stimulation in Liner Completions. Proc., Petroleum Technology Conference, Doha, Qatar.

McDuff, Darren R., Chris E. Shuchart, Shalawn K. Jackson et al. 2010. Understanding Wormholes in Carbonates: Unprecedented Experimental Scale and 3-D Visualization. Proc., SPE Annual Technical Conference and Exhibition, Florence, Italy.

Ndonhong, Vanessa. 2014. Observations from Experimental Acid Jetting on Limestone Carbonates. Master of Science, Texas A&M University (December).

Peaceman, Donald W. 1983. Interpretation of Well Block Pressures in Numerical Reservoir Simulation with Non-Square Gridblocks and Anisotropic Permeability. *Society of Petroleum Engineers Journal*: 531-543.

Sau, Rajes, Anthony Goodrow, Marcus Rockwell et al. 2014. An Integrated Software Technology Based on Research and Field Application for Completion, Stimulation and Fluid Placement Design in Complex Wells. Proc., International Petroleum Technology Conference, Kuala Lampur, Malaysia.

Schwalbert, Mateus Palharini, Ding Zhu, A. Daniel Hill. 2018. Skin Factor Equations for Anisotropic Wormhole Networks and Limited Entry Completions. Proc., SPE International Conference and Exhibition on Formation Damage Control, Lafayette, Louisiana.
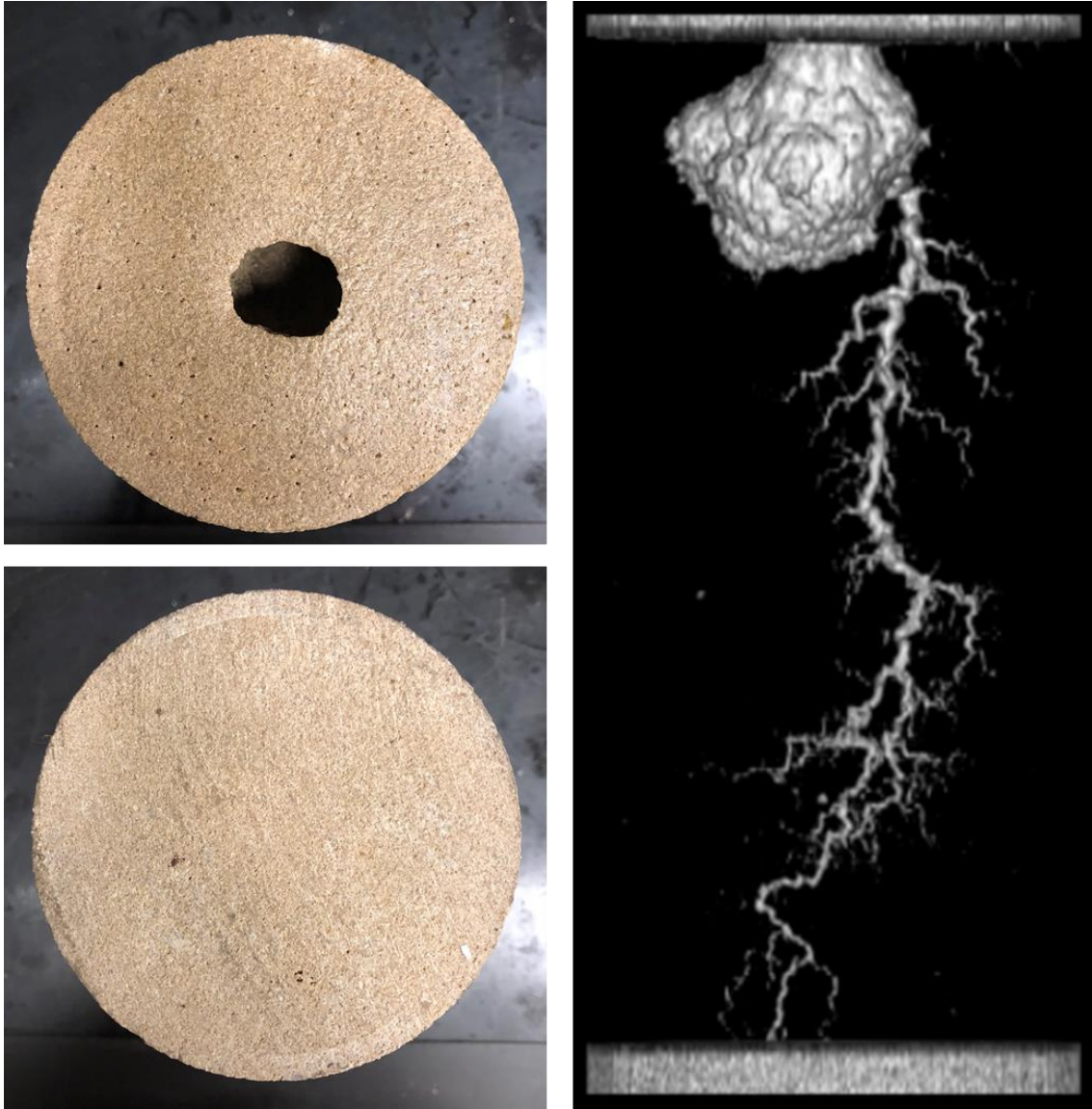
Figure 40 – Core XX01 Visualization
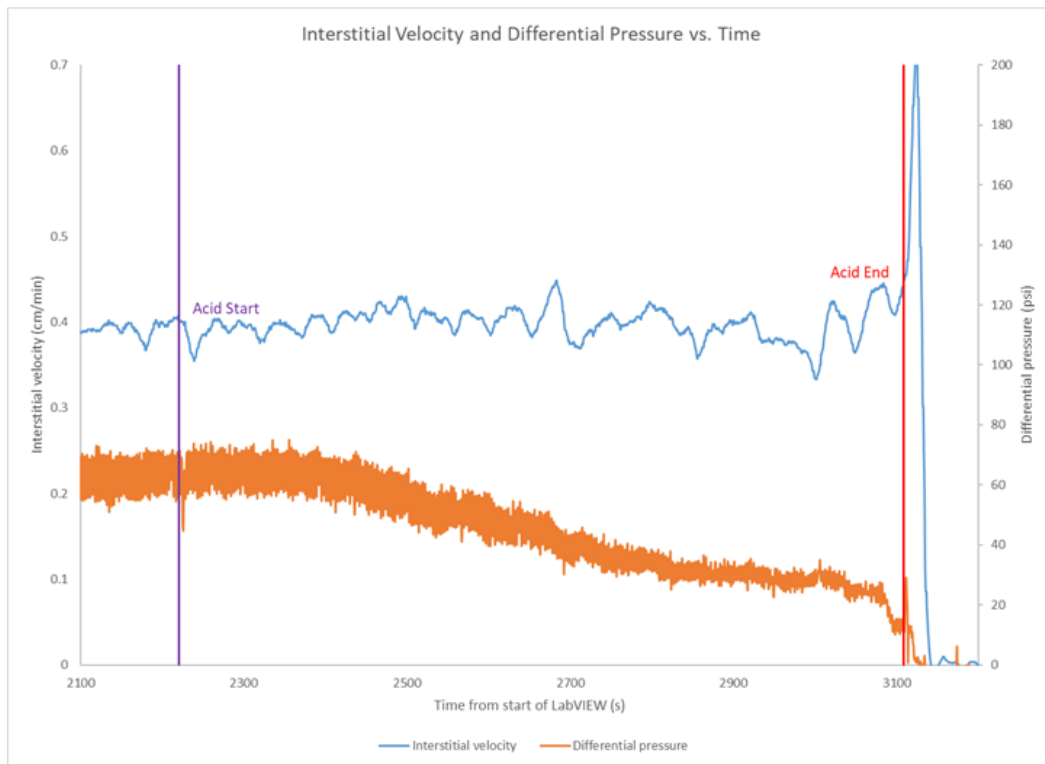
Figure 41 – Core XX01 Experimental Data
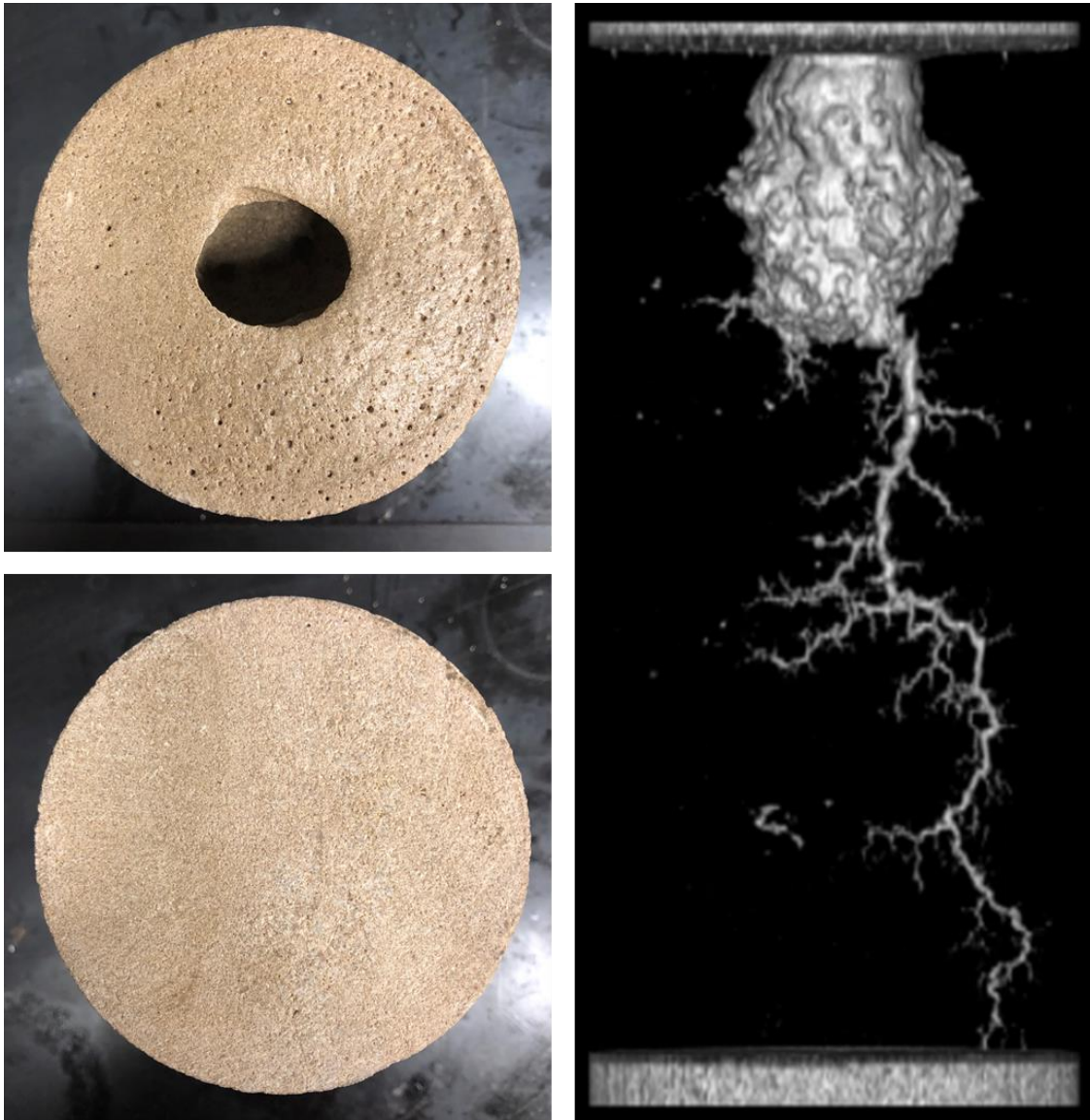
Figure 42 - Core XX02 Visualization
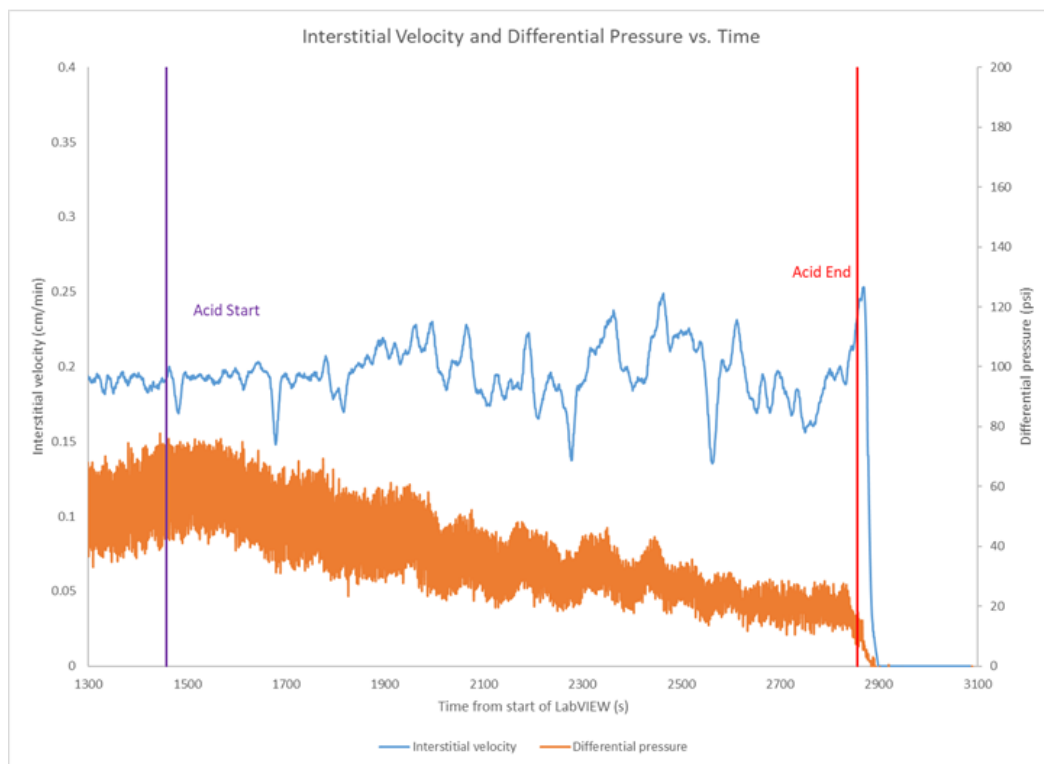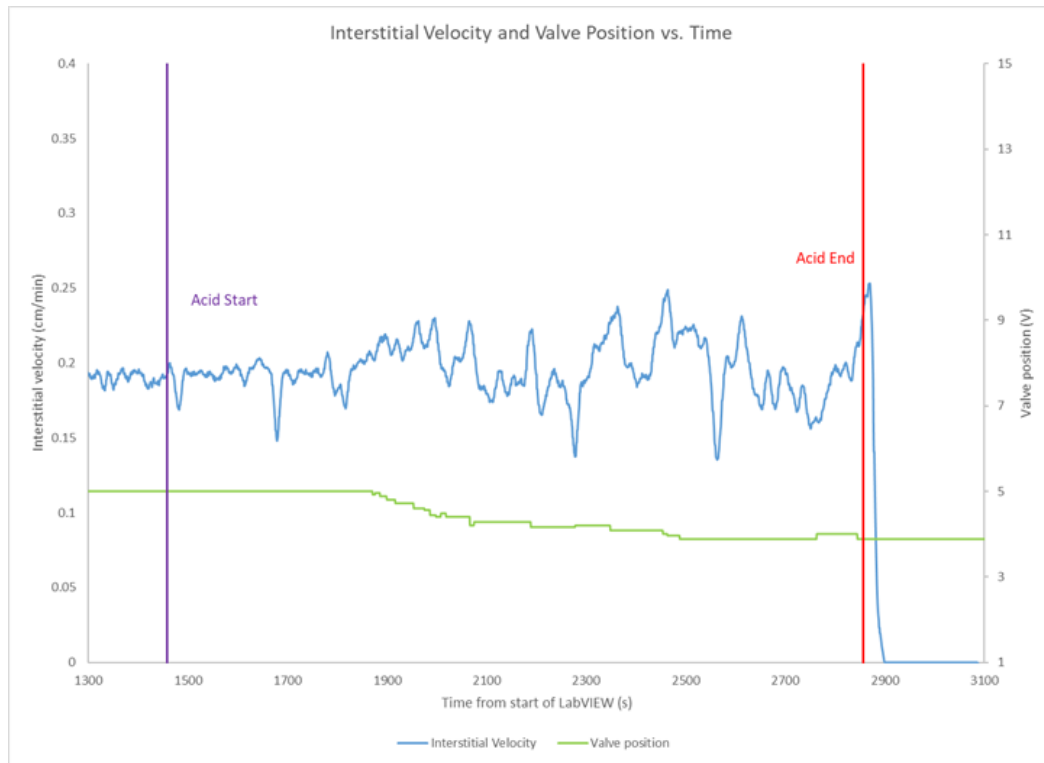
Figure 43 - Core XX02 Experimental Data

94
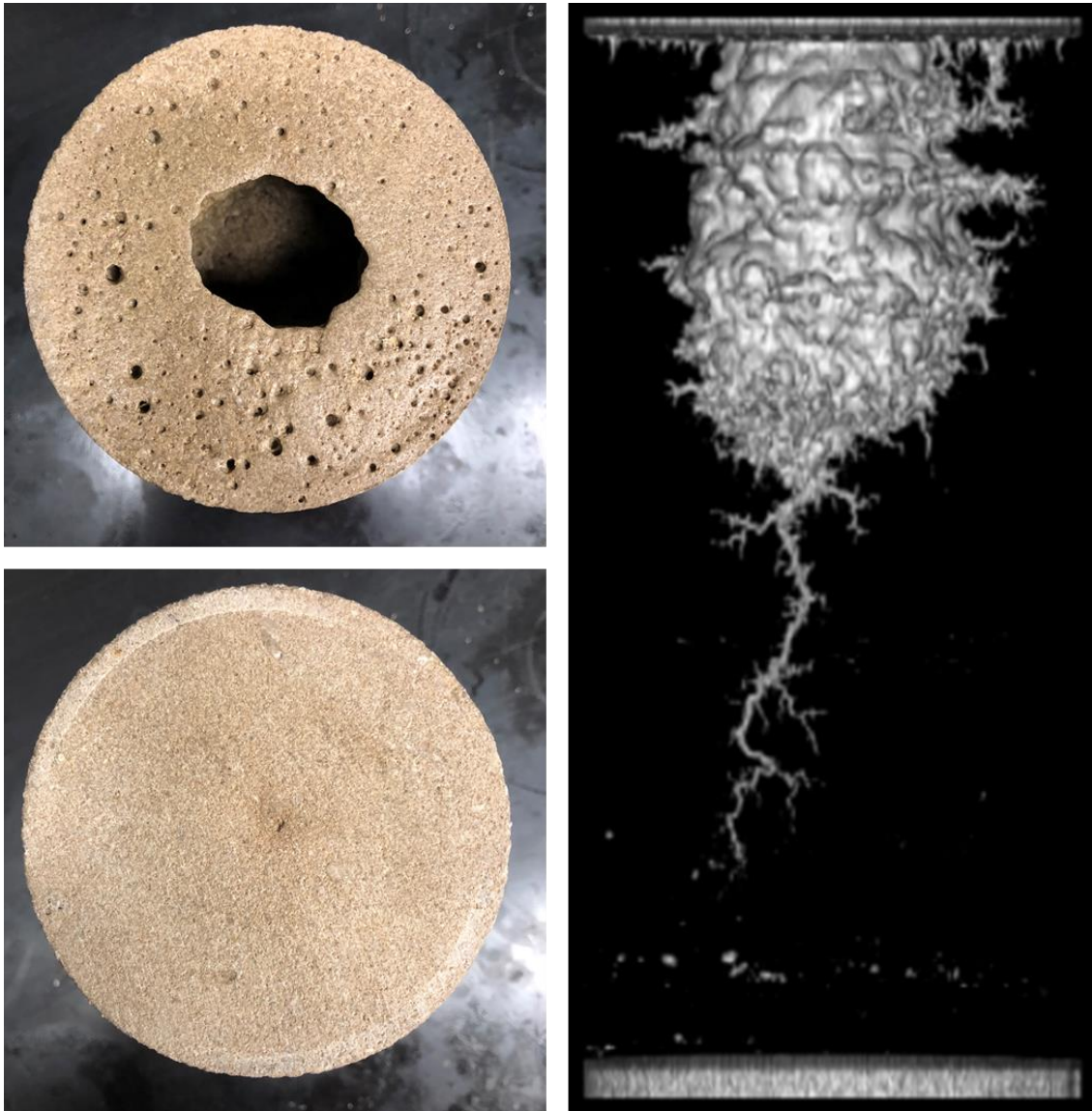
Figure 44 - Core XX03 Visualization
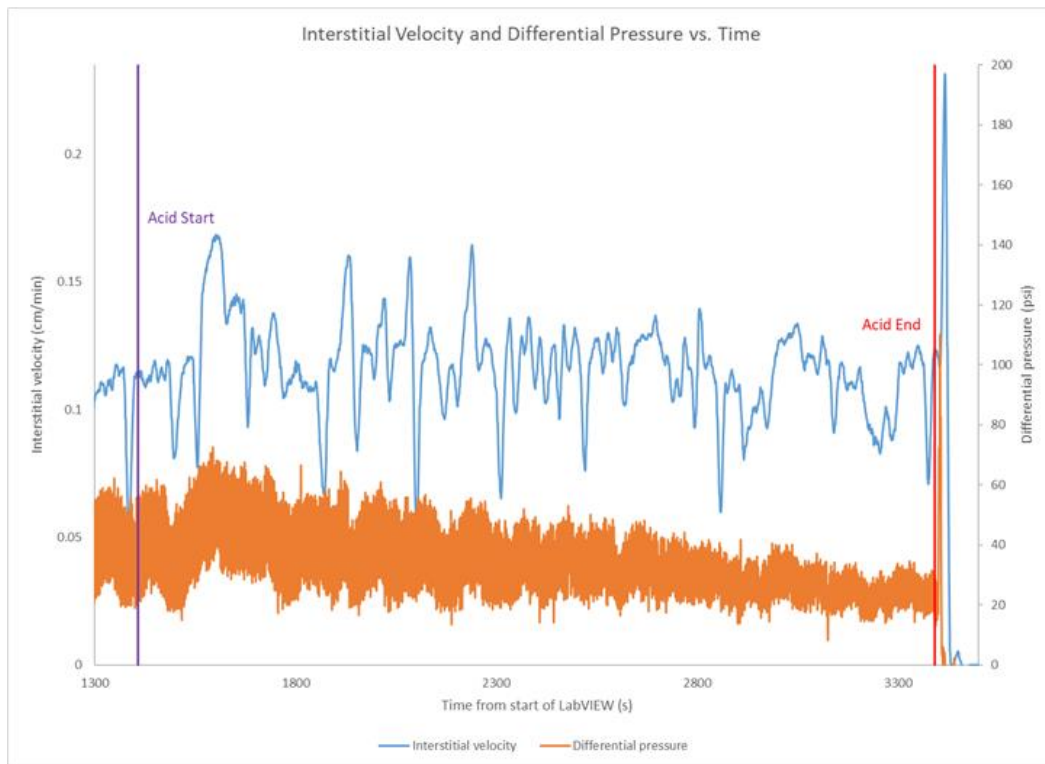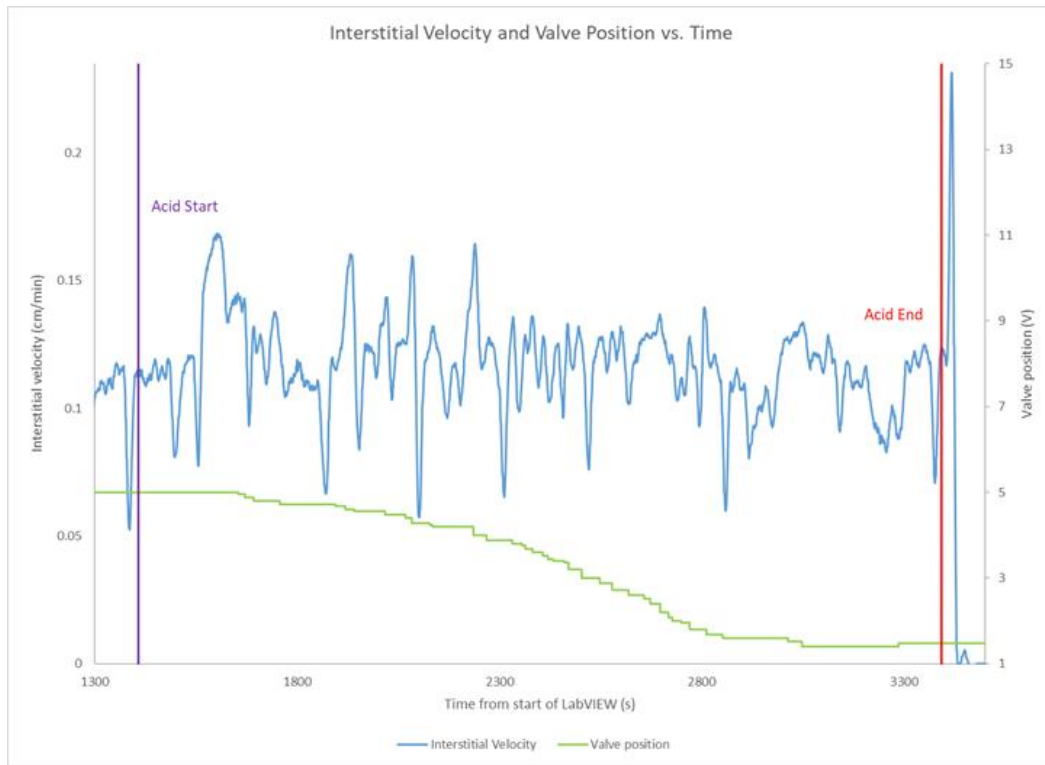
Figure 45 - Core XX03 Experimental Data
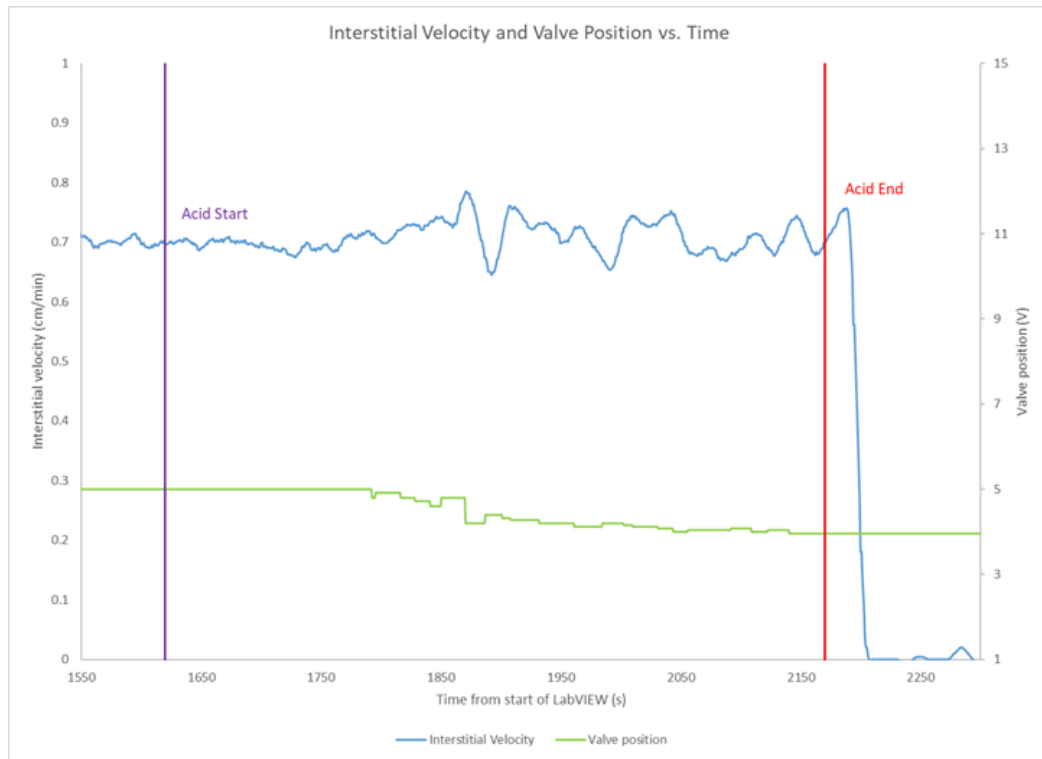
96
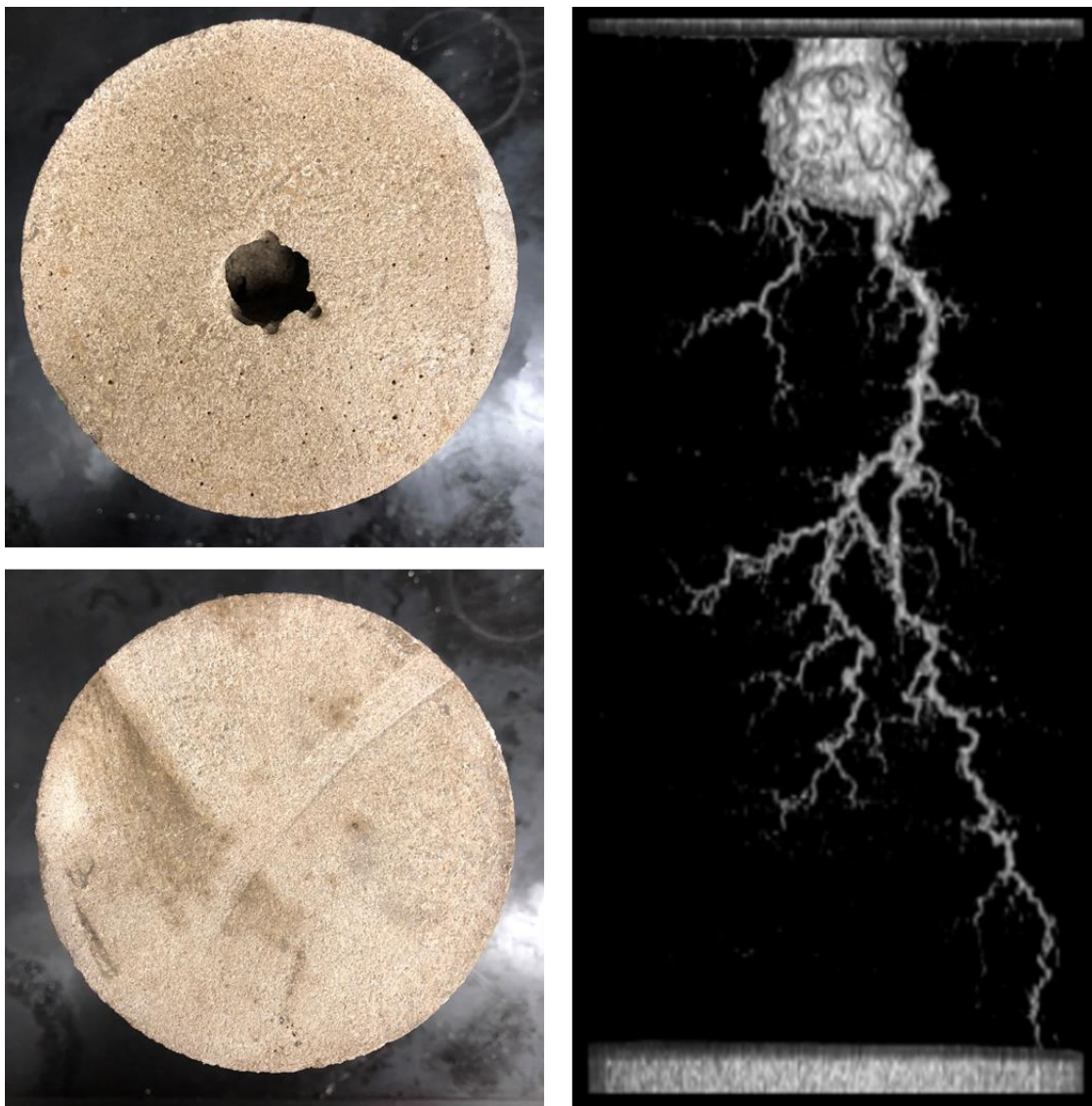
Figure 46 - Core XX04 Visualization
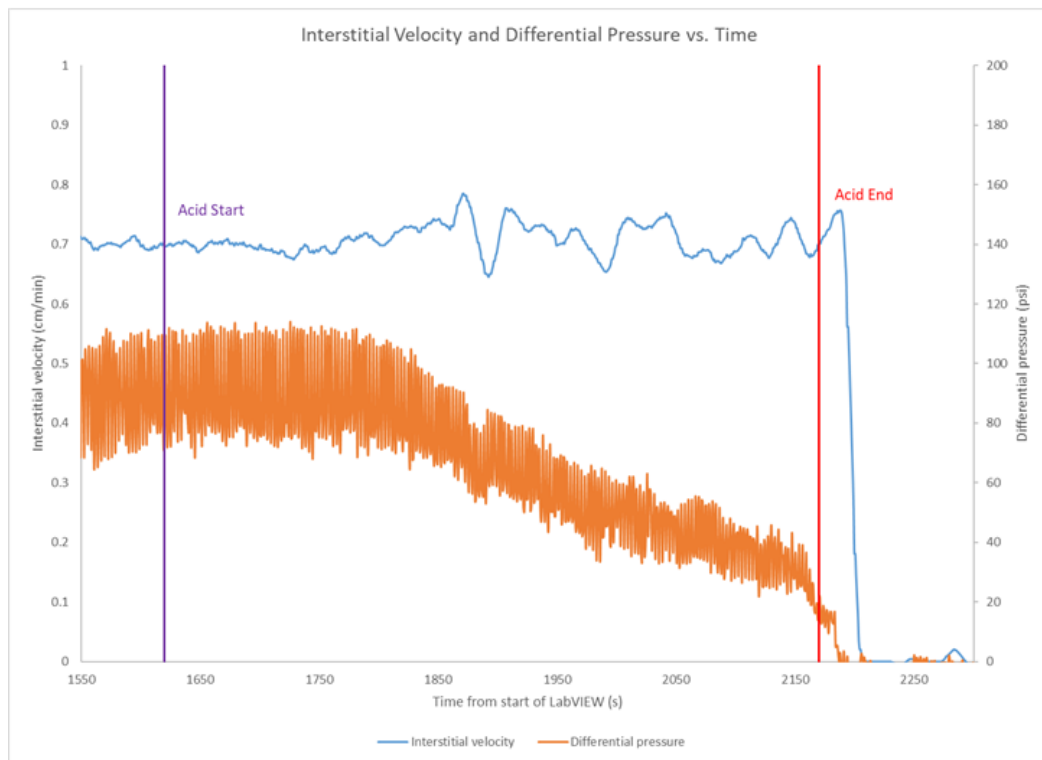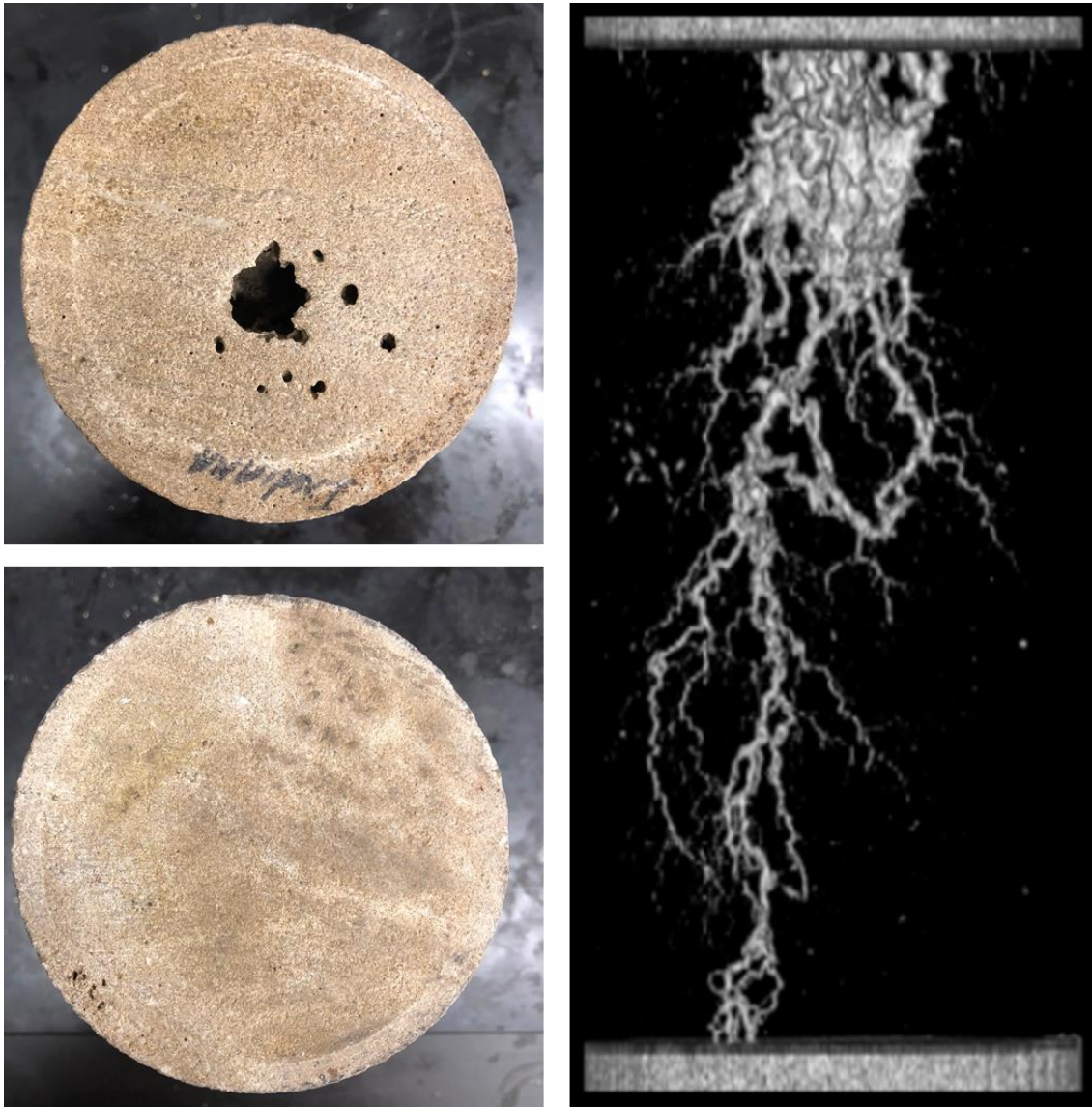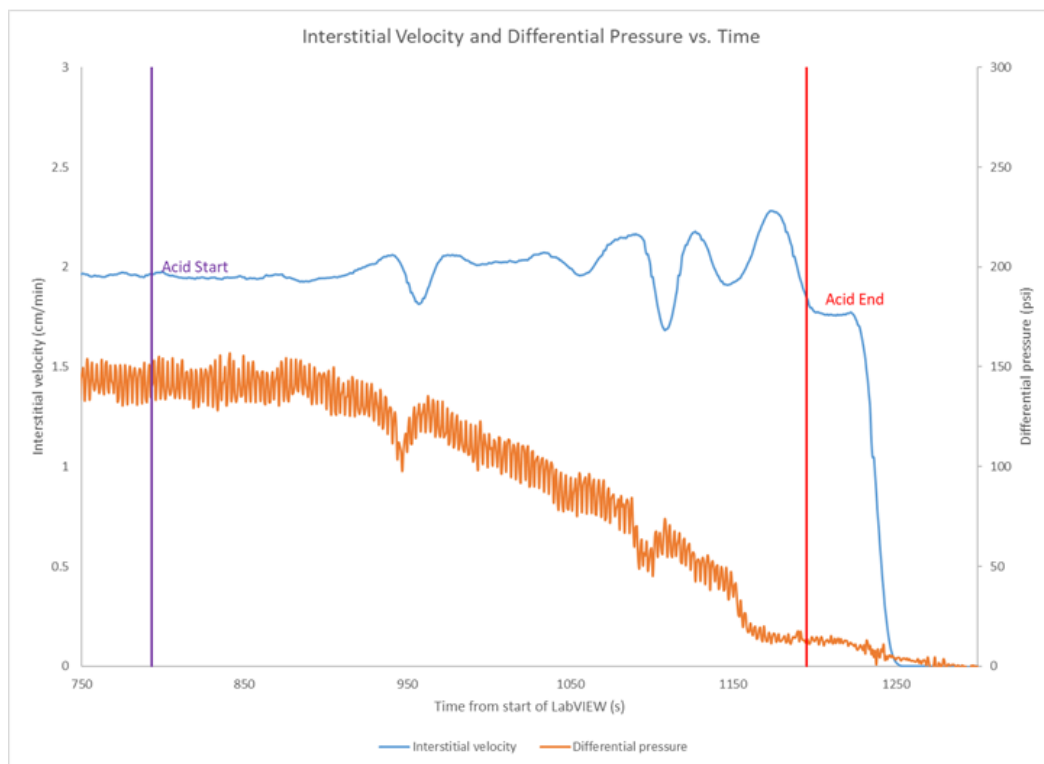
Figure 47 - Core XX04 Experimental Data
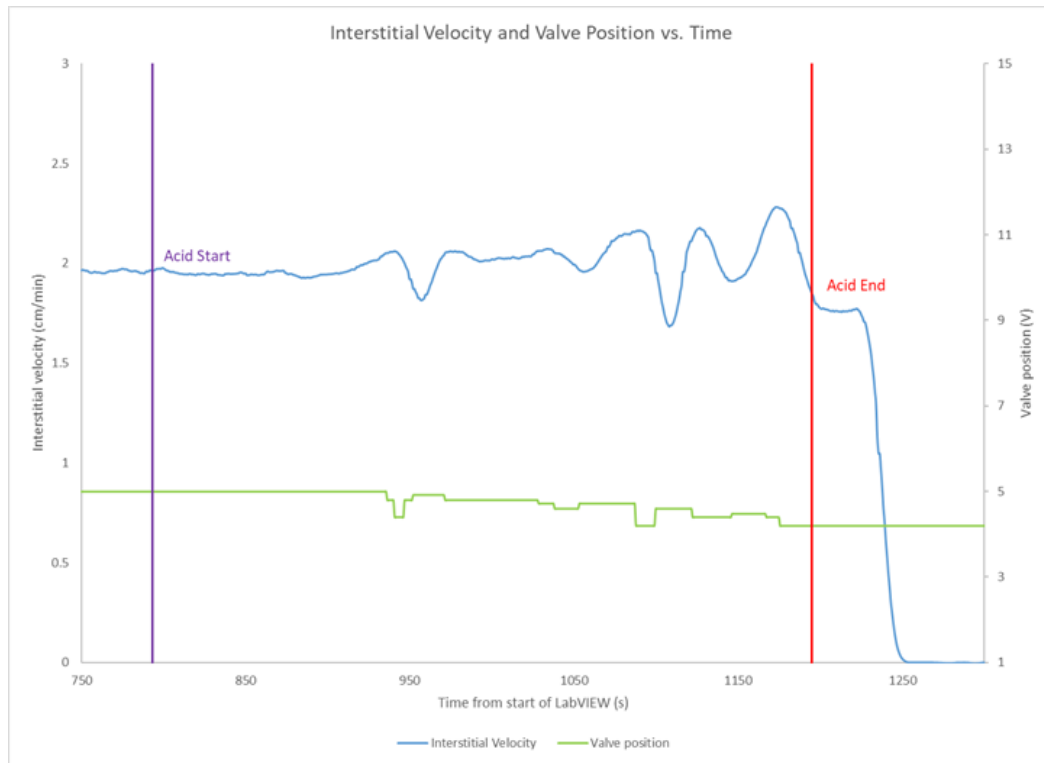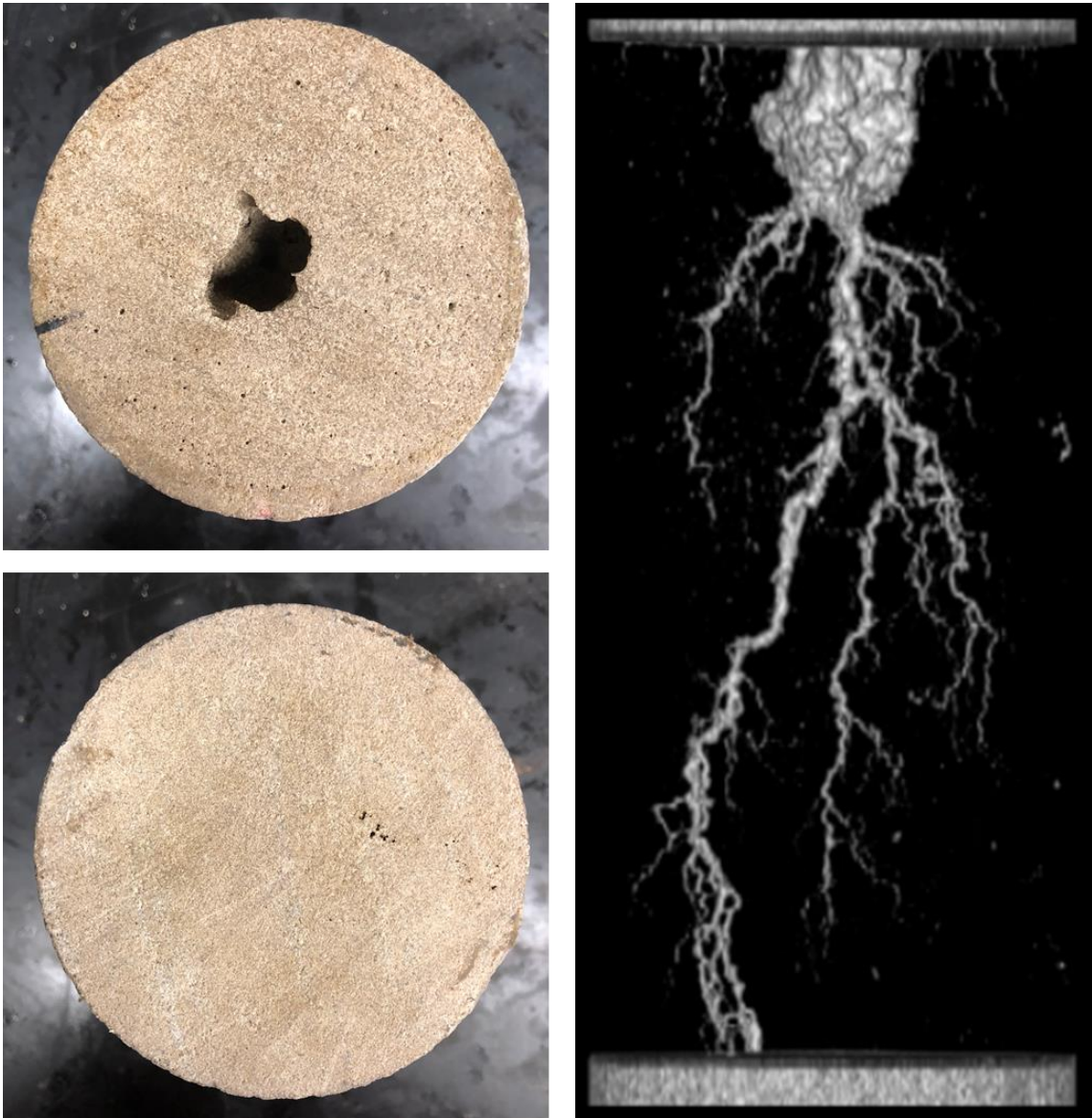
98

Figure 48 - Core XX05 Visualization

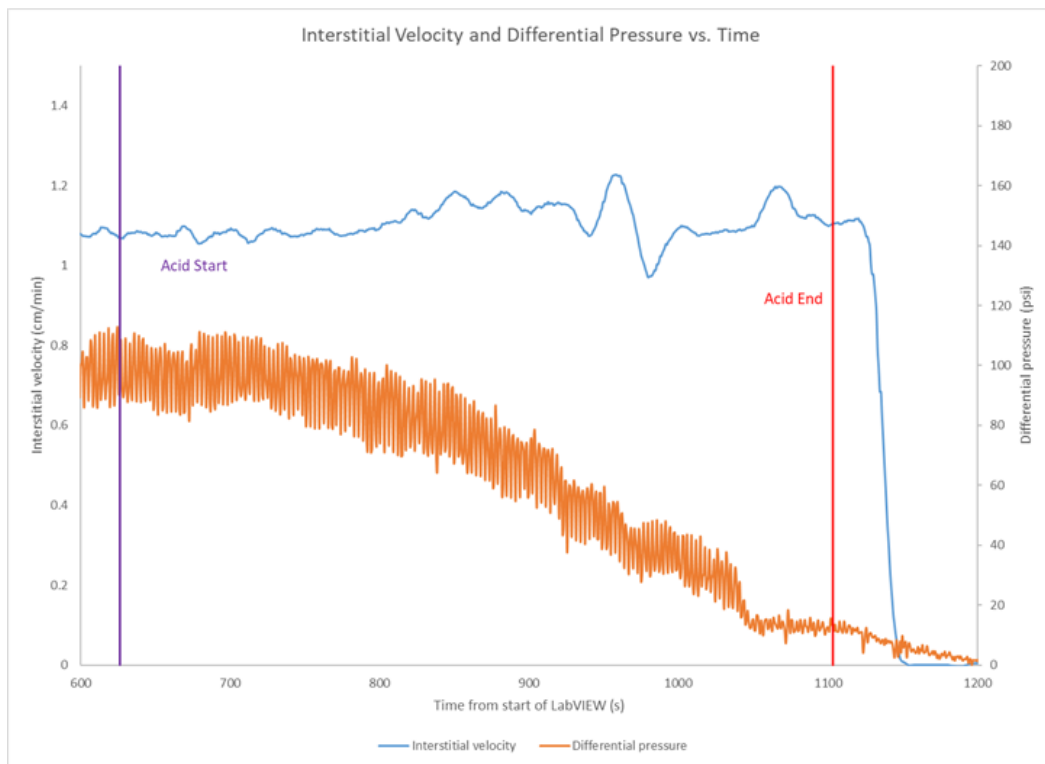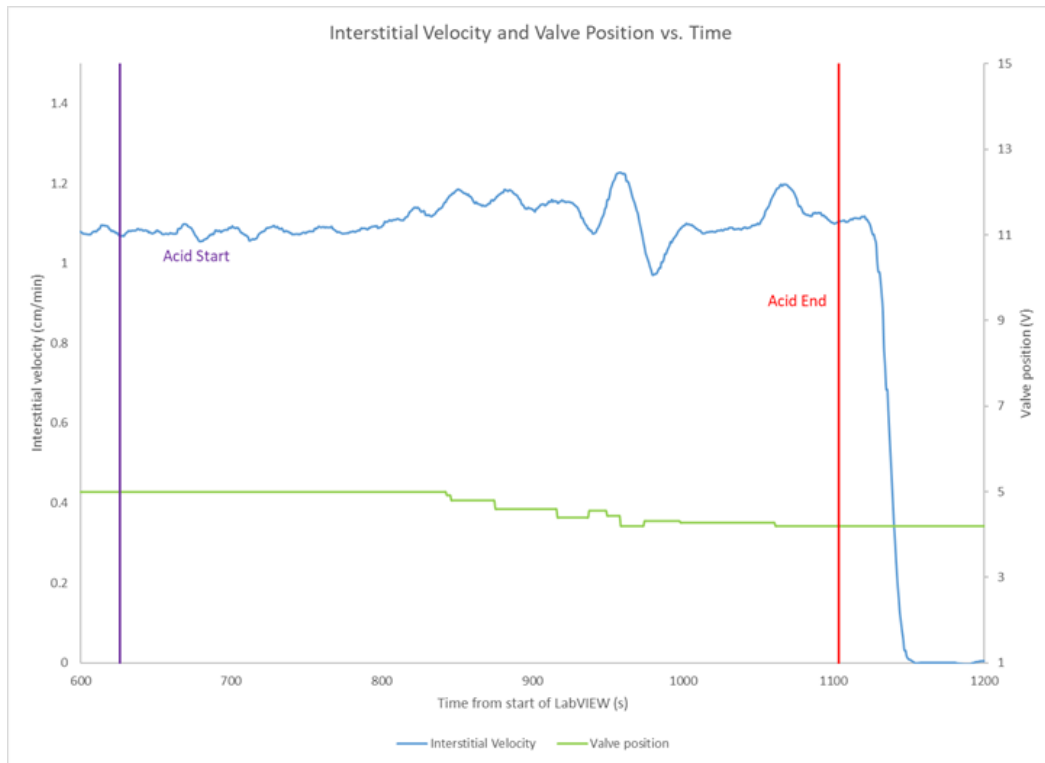**Figure 49 - Core XX05 Experimental Data**

Figure 50 - Core XX06 Visualization

Figure 51 - Core XX06 Experimental Data